IPP-Report

Max-Planck-Institut
für Plasmaphysik

Karsten Schlüter

Dependence of Oxidation on the Grain Orientation of Tungsten

IPP 2017-01
März, 2017

Universität Ulm

Max-Planck-Institut für Plasmaphysik

Bereich Plasmarand und Wand

Abschlussarbeit zur Erlangung des akademischen Grades
Master of Science im Studiengang Physik

Dependence of Oxidation on the Grain Orientation of Tungsten

Karsten Schlüter
Matrikelnummer: 732111
E-Mail: karsten.schlueter@uni-ulm.de

Betreuer: Dr. Martin Balden
Projektleitung: Prof. Dr. Rudolf Neu
Bereichsleitung: Prof. Dr. Ulrich Stroth

Erstprüfer: Prof. Dr. Emanuele Poli
Zweitprüfer: Prof. Dr. Rudolf Neu

Fassung: 20.10.2016

Abstract

Tungsten is planned to be the main material for the first wall armor of future fusion reactors. Therefore, the investigation of tungsten oxidation addresses one safety aspect in an accident case, in which the cooling system fails and the temperature rises to about 1300 K at the wall of the fusion reactor vessel for several days. In such a situation, the ingress of air into the reactor vessel would lead to the formation of tungsten oxides, i.e. WO_3. WO_3 as well as activated WO_3 evaporate into the gas phase which should be avoided. The grain orientations have an influence of the oxidation and are studied in this thesis in more detail.

The grain orientations of tungsten (W) were analyzed using electron backscatter diffraction (EBSD) and were followed by oxidations in a range between 720 K and 870 K. The grain dependent oxidation rates were determined by measuring the thickness of the oxide layer. The data of the thickness measurement were transformed into oxidation rates in $\frac{\mathrm{mg}^2}{\mathrm{cm}^4 \cdot \mathrm{s}}$ to compare them with results obtained by gravimetric measurements.

Tungsten grains with $\{100\}$ orientation have the highest oxidation rate in a range of 720 K to 870 K, which is a factor of two higher than the oxidation rate of W grains with $\{111\}$ orientation. The $\{110\}$ orientation exhibits an oxidation rate in between the $\{100\}$ and $\{111\}$ orientation.

Contents

1 Introduction

The quality of life depends on many different things. One of them is the energy availability, especially of electrical power. Nowadays, the ambition to produce CO_2 free energy is greater than ever due to the expected rapid climate change[1]. On the other hand, the production of energy with fossil fuel is cheap and available 24 h a day. Nuclear fission power plants do not release CO_2 and are available 24 h a day too, but produce radioactive waste. Also, some safety aspects are questioned.

Fusion power plants would have projectable, operational availability, good safety conditions and they are CO_2 neutral[2]. In addition, the fuel is available all over the world and there is sufficient for thousands of years[3] [4]. These are good reasons to perform research on fusion energy.

Fusion energy means that light elements like deuterium and tritium react to helium[5]. To build a power plant based on this reaction is an ambitious international project. The goal is not only to produce energy and therefore electrical power but also energy which is safe, sustainable and economic[6].

The reaction to produce fusion energy is a nuclear reaction which leads to neutron release and therefore, activation of the surrounding materials. For the use in power plants, tungsten (W) is discussed as a first wall material facing to the plasma[7] [8] [9]. Tungsten has a high melting point which is required for a first wall material and has a minimized reaction with the fuel tritium[10]. But tungsten will be activated by fast neutrons from the fusion reaction.

In an accident case, in which the cooling system fails in a fusion power plant, the temperature could rise to approximately 1370 K for several days[11]. In such a situation the ingress of air into the reactor vessel would lead to the formation of tungsten oxide (WO_3). WO_3 starts to evaporate at a temperature around 1020 K, carrying activated tungsten[12] [13].

One way to avoid this is the use of self-passivating tungsten alloys[14] [15]. The oxidation resistance of newly developed alloys is tested and the results will be shown in the appendix of this master thesis.

The main goal of this master thesis is to develop a method for measuring the oxidation rate in relation to the crystal orientation of tungsten. Such an investigation of the oxidation of tungsten can lead to a better understanding and increases the data base which is helpful to reduce tungsten oxidation.

It is possible to investigate grain dependent oxidation with single crystals, but the idea in this thesis is to measure grain dependent oxidation on recrystallized polycrystalline tungsten samples. A recrystallized tungsten sample has grains with different orientations and the grain orientations are analyzed by electron backscatter diffraction. Different grain orientations can be evaluated in one oxidation experiment. If the oxidation rate varies with the grain orientation, the thickness of the oxide layer on the individual grains will vary too. Thickness measurements of oxide layers are used to create a large and meaningful data set. Afterwards, the data of the determination of the grain orientation and of the thickness measurements are merged together.

The first goal was to develop a method for determination of grain dependent oxidation. The thickness of the oxide layer was measured in relation to the grain orientation. The second goal was to verify the thickness measurements and therefore, the thickness measurements are transformed into oxidation rates in $\frac{\mathrm{mg}^2}{\mathrm{cm}^4 \cdot \mathrm{s}}$ to compare them with results obtained by gravimetric measurements. Third, the method was applied to investigate grain orientated oxidation at four different temperatures.

The master thesis is structured in six chapters, wherein the first chapter gives an introduction. Chapter 2 contains some basic background information about fusion, tungsten, tungsten oxide and analysis techniques. In chapter 3, the method development is described. This includes the instruments for preparation, measurement and oxidation of the sample as well as information on the use of the equipment. Also, experimental parameters are investigated which influence the oxidation or the evaluation. Chapter 4 gives an overview of the developed method. A description of the experimental procedure is given and the evaluation of the data is given. Chapter 5 contains the results of grain dependent oxidation, the comparison of thickness measurements of the oxide layer to gravimetric analysis systems and the results of grain orientated oxidation at four different temperatures for the low indexed orientations $\{100\}$, $\{110\}$ and $\{111\}$. In chapter 6, the errors of the measurement techniques, oxidation effects, grain dependent oxidation and the influence of the temperature on grain dependent oxidation are discussed. Each chapter starts with a short introduction to provide more details to its content.

2 Background

This chapter gives some basic information about the principle of fusion, an accidental scenario in a fusion power plant as well as the chemical behavior and the crystal structure of tungsten. In addition, some information are shown about tungsten oxides and techniques to analyze tungsten and tungsten oxide.

2.1 Fusion Plasma and Activation of Tungsten

There are two ways to get energy using nuclear reactions. Both ways release the energy according to the equation $\mathrm{E} = \mathrm{mc}^2$. First, by nuclear fission a heavy atomic nucleus like uranium is split into two nuclei which in sum have a lower mass (m). The resulting mass defect is released as energy. The second way is nuclear fusion. By nuclear fusion two light nuclei fuse into one nucleus which has a lower mass than the two nuclei. The mass loss is also released as energy.

As iron is the element with the highest binding energy per nucleon, heavier elements release energy by nuclear fission and lighter elements release energy by nuclear fusion.

The energy gain per deuterium tritium (D-T)-reaction is in the order of MeV ($1\mathrm{MeV} = 1.6\times10^{-13}$ J) whereas the oxidation of fossil fuels is in the order of eV ($1\mathrm{eV} = 1.6\times10^{-19}\mathrm{J}$). Therefore, the D-T-reaction is attractive to energy gain. In addition, deuterium and tritium quantities are sufficient for thousands of years and they are distributed equally all over the world.

In a nuclear fusion power plant, the preferred fuel is D-T. The D-T reaction has the highest cross section at the lowest energy which makes this reaction most attractive. Different nuclei combinations are shown in figure 1.

The D-T reaction generates two products: one helium (He) nucleus and one neutron. The energy released by this reaction is 17.6 MeV. With respect to the momentums, this energy is distributed to He with 3.5 MeV and to the neutron with 14.1 MeV[16]. The reaction is shown in the following equation:

$$\mathrm{D} + \mathrm{T} \rightarrow {}^{4}\mathrm{He} + n + 17.6\ \mathrm{MeV} \tag{2.1}$$

Helium is a non-toxic, non-radioactive element. It stays in the plasma because it is charged and delivers its energy to the plasma. The neutron is not electrically charged and absorbed in the first wall. As a consequence, elements like tungsten are transformed into unstable isotopes. The wall materials can be chosen to form mostly stable elements by neutron irradiation.

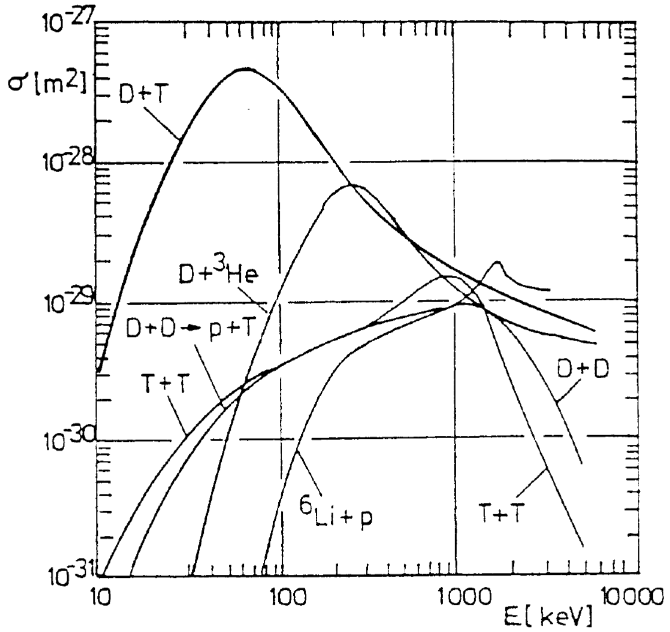

Figure 1: Cross section of fusion reaction for different nucleus combinations[16]. D-T-reaction has the highest cross section.

Tungsten is a candidate for a fusion power plant because after 75 years, "all of the tungsten material has a contact gamma dose-rate that has fallen below the 20 mSv/h level, allowing it to be categorised as complex recycling material"[17]. The high melting point, the minimized reaction with tritium or the low sputter rate are also aspects why tungsten is chosen as a first wall material[12] [10] [7] [8] [9].

2.2 Accident Scenario

In 2004, the European Power Plant Conceptual Study (PPCS) presented aspects on an investigation of a fusion nuclear power plant accident in which safety aspects and environmental aspects were investigated.

In the study four different types of nuclear power plants were described and are named Model A, B, C and D. The main differences between these models are in the cooling system and in the used materials.

- Model A based on a liquid lithium-lead blanket with a water cooled system.
- Model B is a helium cooled system. The material described by Model B based on a blanket made by alternate layers of lithium ortho-silicate and pebbles of beryllium.

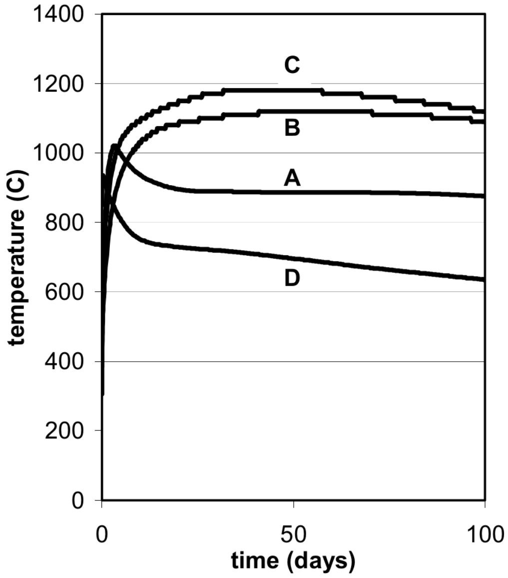

Figure 2: "Conservatively calculated temperature histories, for hypothetical bounding accidents in the outboard first wall of the four PPCS Models"[11].

- Model C has a lithium-lead blanket, in which heat is removed by circulation of the lithium-lead itself and has a helium coolant passing through channels in the structure.
- Model D uses a lithium-lead blanket, in which the lithium-lead itself is circulated as the primary coolant.

More information can be found in the PPCS report[11].

Some calculations were done in the PPCS for accident scenarios. "For Models A and B, this was assumed to be a total loss of cooling from all loops in the plant, with no active cooling, no active safety system operating, and no intervention whatever for a prolonged period. For Models C and D, the lithium-lead was retained in the model, but not circulated, so as to retain the decay heat generation by the lithium-lead itself"[11].

Figure 2 shows the calculated temperature evolution over several months. In all models the temperature rises above the evaporation temperature of tungsten oxide.

The calculated biological hazard of tungsten oxide through inhalation is 1.78 Sv/mg after one day[17].

Radioactive tungsten oxide should be avoided in the gas phase. Therefore, studying the oxidation behavior of tungsten is necessary. One solution to avoid evaporation of tungsten oxide would be the self-passivating tungsten alloys which could have drastically reduced oxidation rates of tungsten. Such alloys are described and tested in the appendix in chapter A.1.

2.3 Properties of Tungsten

Tungsten (W) is a transition metal which is in the sixth group of the periodic table. There are over 45 isotopes of W and five of them are naturally occurring[12].

The W isotope with the highest occurrence has 110 neutrons and 74 protons. In addition, the standard atomic weight is 183.95 u for ^{184}W[12]. This is the major W isotope on earth. W has a high density of 1.7 times of that of lead. The density of tungsten is equal to that of gold[12]. Properties of tungsten are given in table 1.

Table 1: Properties of tungsten[12].

Density*/ $\frac{\mathrm{g}}{\mathrm{cm}^3}$	19.24	Atomic radius/ pm	137
Thermal conductivity*/ $\frac{\mathrm{W}}{\mathrm{m \cdot K}}$	173	Covalent radius/ pm	125
Heat capacity/ $\frac{\mathrm{J}}{\mathrm{mol \cdot K}}$	21	Lattice parameter/ Å	3.16
Melting point/ K	3695	Shear modulus*/ Gpa	163
Boiling point/ K	6203	Bulk modulus*/ Gpa	310

*at room temperature

The stable form of tungsten has a body-centered cubic (bcc) lattice configuration[18]. Generally, lattice imperfections can be divided into four groups:

- Point defects (vacancies, self interstitial atoms, impurity atoms)
- Line defects (dislocations)
- Plane defects (stacking faults, grain boundaries, twins, microcracks)
- Volume defects (clusters, voids and bubbles, segregations, microcracks, second phases and domains, etc.)

In nature, tungsten is not available in pure metallic form but only in form of chemical compounds like tungsten(VI)-oxide (WO_3).

The production of pure tungsten starts with a tungsten ore like wolframite. With an ammoniac solution the wolframite is processed to ammonium paratungstate. This substance is precipitated and WO_3 is formed at a temperature over 870 K. Under a hydrogen atmosphere at 1070 K, the tungsten(VI)-oxide is reduced to tungsten powder.

$$WO_3 + 3H_2 \rightarrow W + 3H_2O \tag{2.2}$$

With the powder metallurgy, most of the tungsten is pressed into parts and then sintered. Because of the high melting temperature, sintering of tungsten is an effective way for the production. Subsequently, tungsten can be formed by rolling (rod and sheet production) or forging at elevated temperature.

2.4 Oxidation and Properties of Tungsten Oxides

In the natural environment, tungsten appears always in form of oxides. Several tungsten oxides exist, but four of them are important. The major ones are WO_3, $W_{20}O_{58}$ ($WO_{2.9}$), $W_{18}O_{49}$ ($WO_{2.72}$) and WO_2.

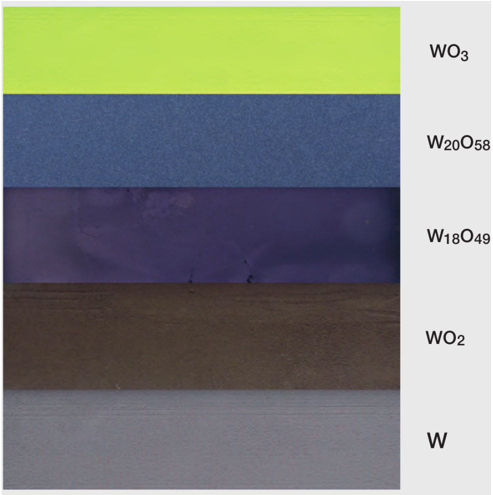

Figure 3: Colors of the tungsten oxides at room temperature and dry atmosphere[19].

The color of the different oxides is shown in figure 3. The color is changing with the formation of different oxides, variation of temperature or humidity.

At room temperature, small amounts of tungsten oxide are formed on the surface due to the contact with air. The temperature has a big impact on the formation of tungsten oxide. The oxidation rate increases slowly with increasing temperature up to 470 K. Above 470 K, the oxidation rate increases rapidly. From 327 K to 670 K, $WO_{2.72}$ is formed. It is a blue and thin oxide film which acts as a protective layer. Above 770 K, this oxide layer cracks. An example of an oxide layer with cracks is shown in figure 4. The sample is oxidized at 870 K for 30 min. Above 770 K, WO_3 is formed. The sublimation of tungsten trioxide starts at 1020 K. To investigate the grain dependent oxidation, sublimation should be avoided. Above 1570 K, the WO_3 sublimation rate corresponds to the oxidation rate.[12]

The oxidation is a complex process. The kinetics of the whole reaction can be separated in sub-steps.

- Adsorption of oxygen on the surface
- Convective and diffusive transport of oxygen to the metal interface

- Insertion of oxygen into the oxide lattice
- Transport of metal atoms to the metal-/oxide-interface

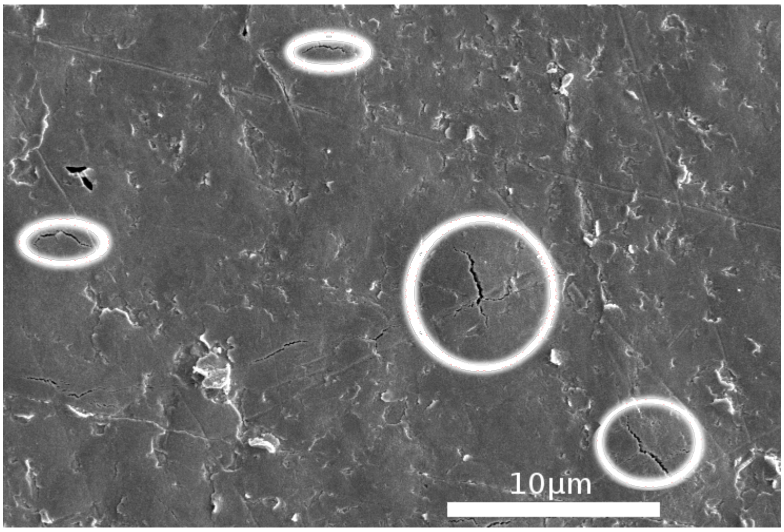

Figure 4: A sample oxidized at 870 K for 30 min. The cracks are formed during the oxidation and marked by white cycles.

At lower temperatures ($< 270\,\mathrm{K}$), oxygen in molecular form is adsorbed on a clean tungsten surface. At room temperature, this adsorption is a precursor state to the atomic adsorption. Normally, an oxidation through the surface is strongly dependent on the activity of oxygen. It is usually proportional to the partial pressure (P) according to $\sqrt{P_{O_2}}$. At first, the oxidation starts through adsorption of oxygen at the surface.

Then oxygen diffuses from the surface into the crystal lattice forming a bcc solid solution. The solubility is very low. The calculated diffusion coefficient is between $D = 7 \times 10^{-8} \frac{\mathrm{cm}^2}{\mathrm{s}}$ and $D = 10^{-7} \frac{\mathrm{cm}^2}{\mathrm{s}}$ at 1970 K[12].

If incorporation of oxygen into the oxide lattice is rate-determining, the oxidation rate will linearly depend on time (t).

If diffusive transport processes are rate-determining through the oxide, the oxidation rate will parabolically depend on time according to $t \propto \sqrt{m}$.

2.5 Crystal Orientations and Grains

Crystals are solid matter and the atoms, molecules or ions are arranged in high order in which they form a crystal lattice. A crystal is physically uniform.

Many properties, like stiffness, depend on the crystal orientation and the crystallite size. The periodicity in a crystal is different for each material. Three different types of solids are shown figure 5.

The left hand side shows a crystal with a high periodicity. Examples are snow flaks or diamonds. Most inorganic solids, for example tungsten, are polycrystalline. They are composed of many crystallites, also called grains, which have different crystal orientations. This is shown in the middle of figure 5. The amorphous non-crystalline solid is shown on the right hand side. The elements of the solid are randomly arranged and there is no periodicity of the elements. An example for this is glass.

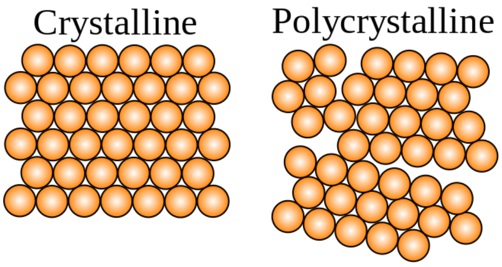

Figure 5: The crystal on the left hand side has a high periodicity. The polycrystalline solid in the middle is composed of many crystallites. The amorphous solid on the right hand side is random and has no periodicity [20].

A metal lattice structure can be simplified. Metal atoms contribute valence electrons to the electron cloud. The binding forces are undirected and in all directions equal. [18]

One concept of a crystal is a structure with stiff balls. Goldschmidt and Laves [18] say that there are three building principles of this structure.

- Principle of dense packing:
  The atoms in the crystal structure strive for an order which fills the space closestly.
- Symmetry principle:
  The atoms in the crystal structure strive for an order which has the highest possible symmetry.
- Interaction principle:
  The atoms in the crystal structure strive for an order of the highest possible coordination number. Which means atoms have as many neighbors as possible and can interact with them.

The regular crystal structures can be interrupted by so called defects. There are different kinds of defects like point-, line-, planar- or bulk- defects. The defects can be healed at the recrystallization temperature.

2.6 Recrystallization and Grain Growth

Recrystallization is a process to repair lattice defects. The recrystallization temperature (T_R) is around 0.4 times of the melting temperature[21]. The grains do not grow at T_R. They are reconstructed, new grains are formed and therefore smaller grains are in the structure. Due to the microstructure, properties like stiffness and hardness decrease. In contrast, the ductility increases.

At higher temperatures the grains grow. The neighboring grains with different orientations have varying sliding levels. Small grains have more grain boundaries in the material. Energy is required during deformation to overcome grain boundaries. In contrast to small grains, larger grains have less grain boundaries and therefore

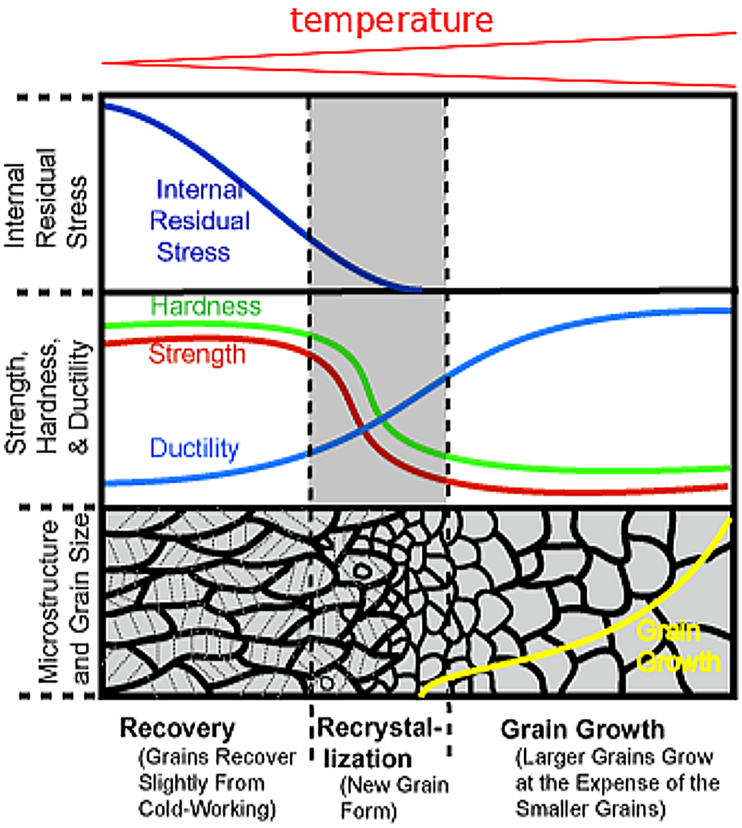

Figure 6: Influence of the temperature on the grain size and the mechanical properties.[21]

a higher ductility.

Figure 6 shows a picture of recovery, recrystallization and grain growth. In addition, some physical properties are shown. In the range of T_R new grains are formed.

At the edges of the grain boundaries are stress and strain and the surface tension is higher on smaller grains than on larger grains. For an energetically favorable state, the grains should be larger. Therefore, if there is enough thermal energy, the grains will grow.

The grain growth can be prevented by intermetallic phases of alloys with metals like Al, Mo, Nb, Ti optionally in combination with N or C[21]. In components which are exposed to high temperatures, the crystal structure must be stabilized in terms of grain growth.

In this master thesis, tungsten is recrystallized at 2100 K. This high temperature is needed for the formation of large grains which are required to study the grain dependency of oxidation. Mechanical properties of tungsten are not a topic of this master thesis.

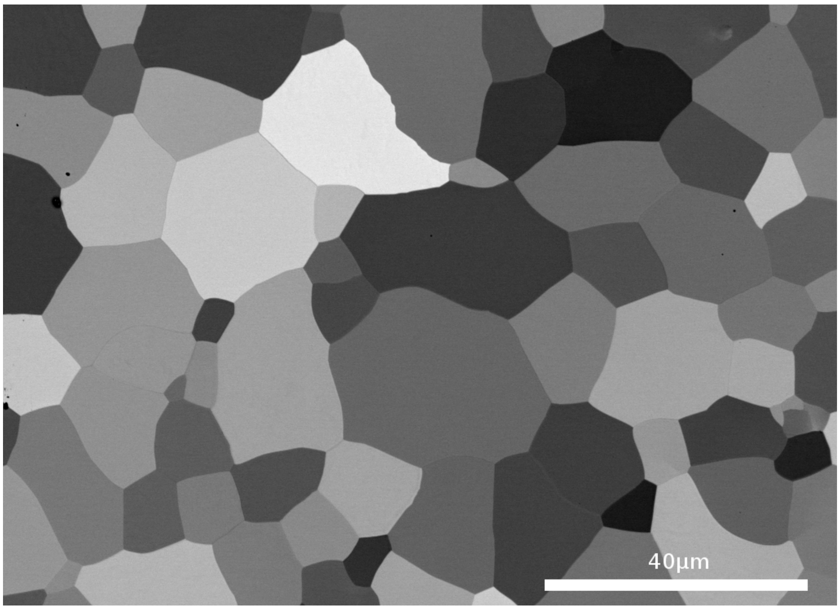

Figure 7: A SEM-picture taken with a backscatter detector of recrystallized tungsten sample. The grain growth took place at 2100 K. The grain size is around 20 μm.

At a temperature of around 2100 K, the used tungsten sample formed grains around 20 µm. Figure 7 shows grains of a recrystallized tungsten sample which demonstrates that the temperature of 2100 K is suitable for the necessary grain growth (subsection 3.1.2).

2.7 Preparation of the Surface by Electropolishing

There are different ways of surface preparation. Besides mechanical polishing electropolishing can be used.

Electropolishing is an electrochemical stripping using electrolysis. Electrolysis means, chemical processes and chemical changes take place in a substance on which a current is applied.

The appropriate conditions for electrolysis are essential for surface preparation. The current has to be adjusted to the electrolyte and is normally in the range between 0.04 A/cm^2 and 3 A/cm^2 [22]. A direct current (DC) voltage source is needed. The electrochemical process removes material from the positive pole, the anode. Normally, the tungsten sample is used as the anode.

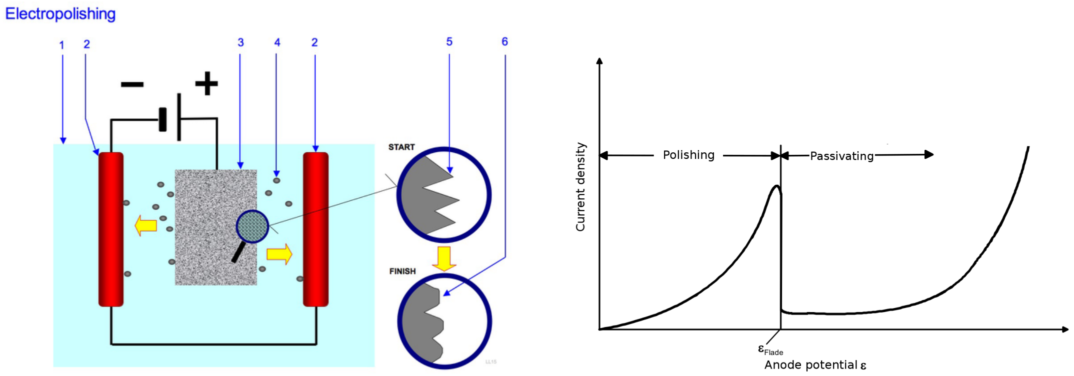

(a) Electropolishing principle: 1. Electrolyte 2. Cathode 3. Workpiece to polish (Anode) 4. Particles moving from the workpiece to the cathode 5. Surface before polishing 6. Surface after polishing [23].

(b) Current density potential curve. If the potential is too high, oxygen will be formed. Therefore, an oxidized layer at the anode can be produced which passivates the surface at ϵ_{Flade}.

Figure 8: The left hand side shows the principle of electropolishing. On the right hand side, the potential curve is given for an oxidized layer during electropolishing.

For the current flow between two electrodes, an electrically conductive medium is required. In general, it is an aqueous solution like sodium nitrate ($NaNO_3$) or an alkaline solution like sodium hydroxide (NaOH). In this master thesis, NaOH is used for the electrochemical polishing.

At the anode, the metal is released into the electrical conductive medium. In contrast to the cathode, there is no effect at the metal. In addition, there is a chemical reaction in the electrolyte.

Figure 8(a) shows the basic principle of electropolishing. There are two cathodes and the sample is situated in the middle, operating as anode. The electrolyte is around the cathodes and anode.

The removal of the material can be described by Faraday's laws. The mass (m) is proportional to the molar mass (M) of the dissolved material and to the amount of electrical charge ($I \cdot t$).

$$m = \frac{M}{z \cdot \mathrm{F}} \cdot I \cdot t \tag{2.3}$$

where F is the Faraday's constant (96 487 As/mol), t is the time in seconds (s), I is the electric current and z is the electrovalence of change. An example of z with iron (Fe) is $\mathrm{Fe} \rightarrow \mathrm{Fe}^{2+} + 2\mathrm{e}^{-}$ where e is the electron charge and z=2.

The workability of a material depends only on its electrochemical properties and the reaction products. It does not depend on the mechanical properties like tensile strength.

During the electrochemical process, the velocity of the metallic dissolution process depends on the electrochemical kinetics. The electrode potential is the main factor on this process.

At a specific electrode potential, the electrolyte is transformed into oxygen at the anode. The oxygen can oxidize the sample or the metallic ions in the electrolyte and thereby influence the polishing. Figure 8(b) shows the current density versus the potential. This shows the effect of an oxidized layer on the sample during electropolishing. At the flade-potential (ϵ_{Flade}), the oxidized layer passivates the surface and the current decreases. This should be avoided.

The advantages for electropolishing over mechanical polishing are:

- Short processing time
- High reproducibility
- High surface quality

As a disadvantage, in comparison to the mechanical polishing, "Long waves" were found on the tungsten surfaces in this master thesis. The height of the long waves was up to 100 nm (subsection 3.2.3).

2.8 Scanning Electron Microscope

A large part of the experimental work in this thesis was done with a scanning electron microscope (SEM). The main advantages of a SEM are the extensive depth of sharpness and a high resolution. The resolution depends on the diameter of the electron beam. The beam scans the sample step by step. In addition, the sample is under vacuum and must be electrically conductive. The images should be carefully interpreted because optical illusions easily lead to misinterpretation.

Advantages of a SEM are:

- Depth of sharpness
- High resolution
- 3D impression
- Images with many information
- Simultaneous view on images with different contrast [24]

2.8.1 Components of a Scanning Electron Microscope

The SEM basically consists of an electron gun which generates the focused electron beam, an electrical field which accelerates the electrons, a lens system of electric and magnetic fields which forms the beam and a scan unit. These components together are also called column. A sample and several detectors are located after the column. The composition of the basic components on an electron microscope is shown in figure 9(a). The main components are explained in the following subsections.

2.8.2 Electron Gun

The first step to generate an image with an electron microscope is to generate an electron beam. A picture of an electron gun is shown in figure 9(b). In principle, a tungsten filament electron gun consist of a Wehnelt assembly and an anode.

First, electrons are emitted from a cathode. Therefore, there are different types of cathodes. The main ones are the tungsten filament, lanthanum hexaboride crystal and the field emission cathode. The cathode is located behind a Wehnelt cylinder which has a negative charge and pushes the electrons away. The electrons move to the anode and form a beam. Between cathode and anode a crossover is situated

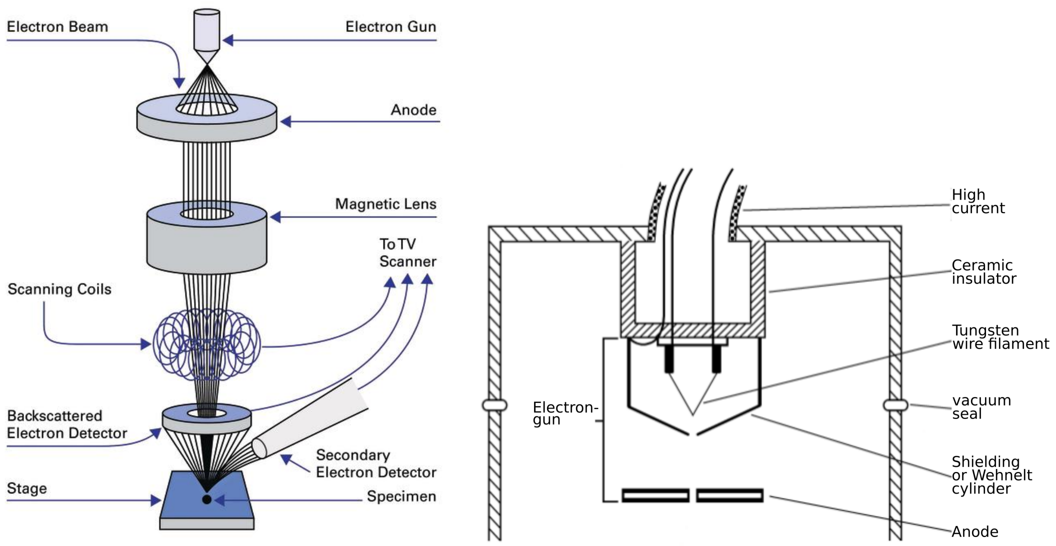

(a) Assembly scheme of a SEM.[25]. (b) Assembly scheme of an electron gun[26].

Figure 9

which has the highest electron density. The anode which accelerates the electrons is located behind the Wehnelt cylinder. At this place, the electrons move into the lens system.

2.8.3 Image of a Scanning Electron Microscope

A SEM produces each pixel of an image step by step and scans row for row. If the detector records electrons, the pixel will change in gray scale according to the number of electrons.

There are several detectors in a SEM. One of them is the Everhard-Thornley-Detector which is the standard secondary electron detector of the most SEMs. The front part of the detector consists of a Faraday cage which is carried out either as a wire mesh or a metal ring. With a positive changeable voltage around 300 V, the secondary electrons are drawn into the detector. If the electrons are in the Faraday cage, they will be accelerated through a voltage of 1200 V and will hit the scintillator which acts as collector. When the secondary electrons collide with the scintillator photons are generated. The light pulses are lead to a photomultiplier which generates and multiplies electrons. The output voltage of the photomultiplier is amplified by a preamplifier.

2.9 Electron Backscatter Diffraction

The electron backscatter diffraction (EBSD), also known as backscatter Kikuchi diffraction (BKD), is an accepted technique for the measurement of microtextures.

The lateral resolution of this technique is around 100 nm. The sample must be tilted to achieve BKD, because the electron beam has to strike the sample at a small angle. A large fraction of electrons are diffracted (backscattered) by the lattice planes in the sample.

The raw data form is a Kikuchi diffraction pattern for the microtexture detection. Figure 10(a) shows a Kikuchi diffraction pattern of a body-centered cubic (bcc) tungsten sample which was recrystallized at 2100 K. The electrons are influenced by the geometry of lattice planes in a crystal and form the Kikuchi pattern.

Pairs of parallel lines with a diffuse background and pairs of lines which intersect at certain points are shown in figure 10(a).

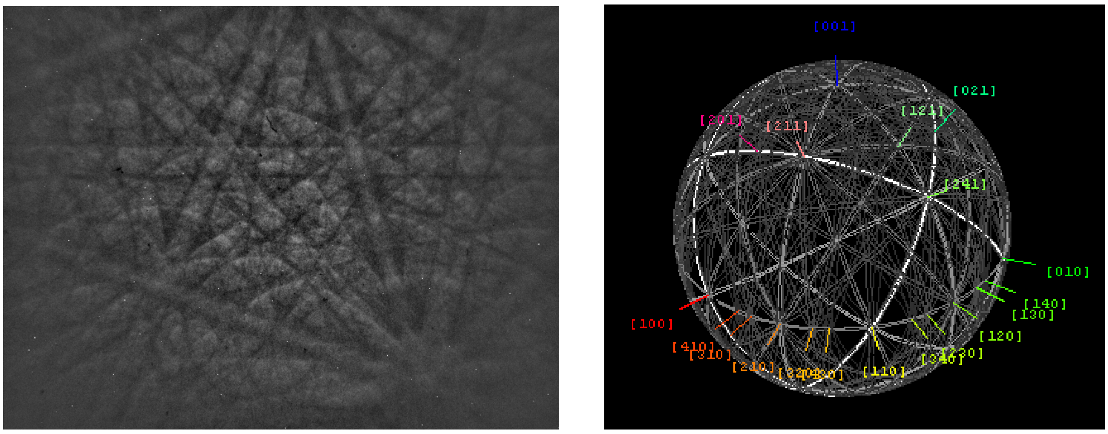

(a) An electron backscatter diffraction pattern of a recrystallized tungsten sample, taken at 20 kV and 1.4 nA with a field-emission electron source under a tilt of 57°.

(b) A 3D-model of the Kikuchi lines is shown. [27]

Figure 10: The left hand side shows an image of the detector and the right hand side shows a 3d-model of the Kikuchi lines.

Each line is a plane in the crystal. The planes scatter the electrons elastically in a crystal. Therefore, the electrons are scattered and some of them interact based on the Bragg condition. Bragg's law describes the condition on θ_B for the constructive interference to be at its strongest [28].

$$\lambda n = 2d\sin(\theta_B) \tag{2.4}$$

where λ is the wavelength of the electrons, n is the order of reflection, d is the distance between two planes and θ_B is the Bragg angle. Electrons reflected through the Bragg condition give diffraction cones of electron radiation. These cones come from the front and back surface of the plane. The cones of the electrons are shown in figure 11.

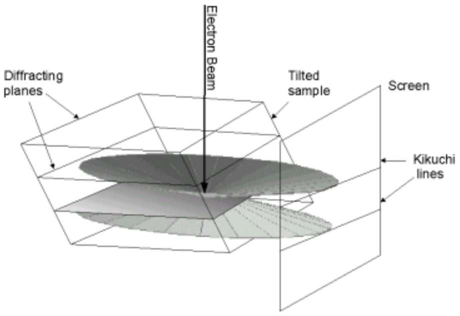

Figure 11: A schematic formation of radiation cones is shown during electron diffraction. Therefore, Kikuchi lines are formed.[27]

Because of the small Bragg angle around 0.5° (smaller than shown in figure 11), the apex angle of the reflected cones is so large that two straight lines, known as Kikuchi lines, appear on the screen. Each pair of lines represents a plane in the crystal. Distances on the pattern are equivalent to angles.

An angle of 45° is an example for a distance between Kikuchi line of the (001) plane and the (110) plane in a cubic crystal. In figure 10(b), the Kikuchi sphere with many Kikuchi lines as a 3D-model is shown. Orientation analysis is the primary application of EBSD.

By solving the Kikuchi pattern for each pixel of a scanned area, an image of the

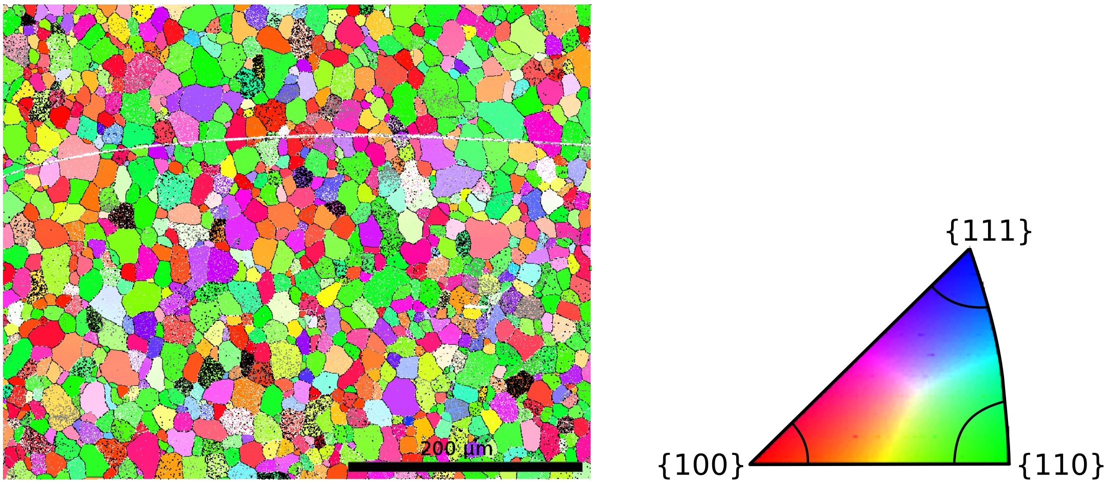

(a) An electron backscatter diffraction map of a recrystallized tungsten sample, taken at 20 kV and 1.4 nA with a field-emission electron source under a tilt of 57°.

(b) The electron backscatter diffraction-color scale of the grain orientation in respect to the surface normal is shown. The cycles at the corners show a variation of 10° of the Euler angle.

Figure 12: The left hand side shows an image of an orientation map and the right hand side shows the electron backscatter diffraction-color scale of the grain orientation.

orientations present on that area can be obtained. Therefore, such images are orientation images and one example of a W surface recrystallizied at 2100 K is shown in figure 12(a). A color-scale for the orientation is shown in figure 12(b).

The information depth of the electron in the EBSD measurement is up to 20 nm below the surface[29]. To avoid inelastic scattering of electrons into the surface, the sample must be cleaned and must not have any contaminations like an oxide layer. Also, crystal defects at the surface influence the EBSD pattern negatively. Electropolishing is an effective method to achieve surfaces with a sufficient quality.

2.10 Confocal Laser Scanning Microscopy

A confocal microscope is a special type of optical microscope. At any time, only one focused plane of the sample is scanned. A physical barrier (a pinhole) is placed at a confocal location in the imaging path between the lens and the detector. The scheme of this microscope is shown in figure 13(a).

The pinhole allows light from just one focal plane to pass through to the detector.

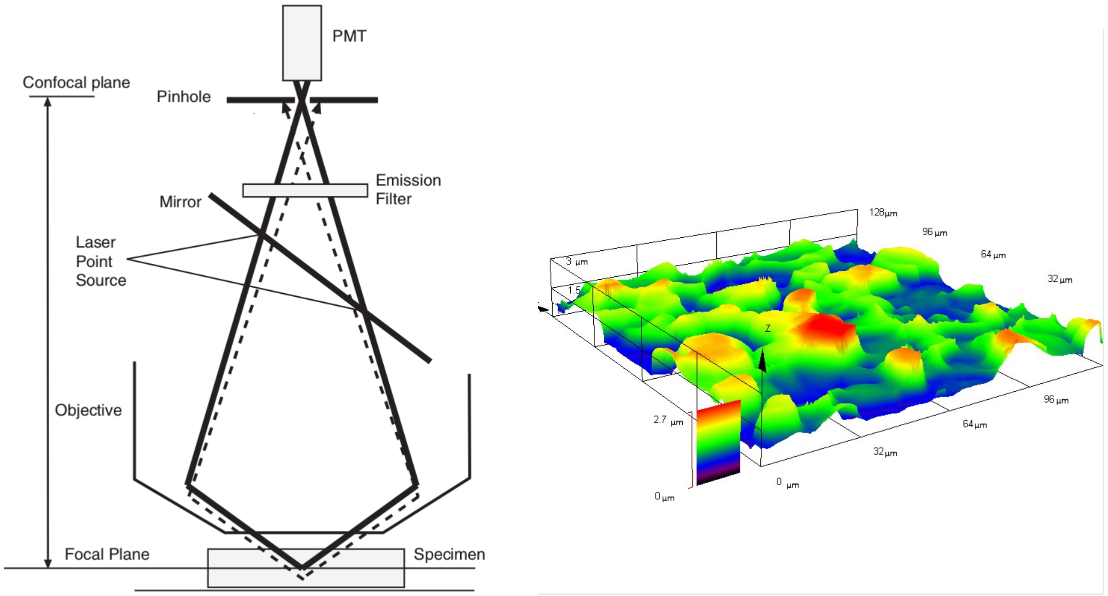

(a) The optical path of a CLSM is shown. The beam is rastered across the sample and arrives precisely at the opening of the pinhole aperture which is found directly in front of the detector (a photomultiplier tube). Light from an out-of-focus plane (a below-focus plane is shown dotted) arrives to either side of the pinhole and is rejected. [30]

(b) A 3D image of the confocal laser scanning microscopy. The tungsten sample is recrystallized and oxidized. Depending on the grain orientation, there are differences in the oxidation rate. This creates different heights of the oxide layer.

Figure 13: Confocal laser scanning microscopy.

The software of the microscope scans each focal plane step by step and creates a height profile picture.

In a confocal laser scanning microscope (CLSM), the laser beam forms a small point and is rastered across the sample. In a rough sample, the process is repeated at different focal planes for up to hundreds of planes.

These planes are combined into a three-dimensional representation of the sample by the software of the microscope. An example of a recrystallized, oxidized sample with different height levels is shown in figure 13(b).

3 Experimental Procedures and Method Development

The main goal of this master thesis is to develop a method to determine the dependence of oxidation on the grain orientation of tungsten. Of course, it is possible to analyze grain dependent oxidation with single crystals, but they are expensive.

The idea is to have different grain orientations in one polycrystalline tungsten sample. With different grain orientations, it is possible to evaluate several orientation dependent effects in one oxidation experiment. Having different grain orientations in one tungsten sample, makes it possible to analyze not only low indexed surfaces but also high indexed surfaces. Additionally, the tungsten sample is placed in one oxidation experiment and every grain orientation has the same experimental condition during this oxidation run. This is difficult to achieve with single crystals.

In this chapter the development of a method is described to determine grain dependent oxidation rates on one polycrystalline tungsten sample. This is achieved by pre-characterizing the tungsten sample, oxidizing the sample and using thickness measurements on specific grains of the oxidized sample.

For thickness measurements of the oxide layer on each tungsten grain, the size of the tungsten grain has to be large enough to avoid influences from neighboring grains. This is described in section 3.1.

Not only the grain size is important but also the quality of the tungsten surface. Before the sample is oxidized, a flat surface is needed for a reliable thickness measurement of the tungsten oxide layer. In addition, a clean, distortion-free surface is needed for the determination of the grain orientation. The preparation of the surface of the tungsten samples is described in section 3.2.

In section 3.3 the determination of the grain orientation is described as well as the marking of the samples to find specific grains before and after the oxidation. Furthermore, the thickness of the oxide layer is determined on cross-sections with focused ion beam (FIB) using the SEM.

This measurement method is time consuming and therefore, another method is introduced in section 3.4 for measuring the relative height of the oxide layer.

Prior to measuring the thickness or the relative heights of the oxide layer, an oxidation of a tungsten sample has to be performed. The oxidation experiment and the possible parameters which influence the oxidation are described in section 3.5.

The last section 3.6 gives an overview of possible parameters, which influence the oxidation.

3.1 Recrystallization and Grain Growth

As a prerequisite to measure grain dependencies, a minimal grain size is essential. This can be achieved through recrystallization of a tungsten sample (see also section 2.6) and is described below.

3.1.1 Instrument: Oven called "HORST"

"HORST" is the name of an oven at the IPP. This heating system is a graphite heater with an argon atmosphere. A picture is shown in figure 14.

Figure 14: Oven called "HORST". The machine is used to heat up the sample at approximately 2100 K for 35 min.

The heating chamber provides enough space to recrystallize 60 tungsten samples at the same time. It has an electrical heating system. The surrounding shell is cooled by water. Therefore, all samples have the same thermal treatment and the properties like grain size should be the same.

3.1.2 Size of the Tungsten Grains

A suitable tungsten grain should have the size of around 20 µm. If the grains are larger, the thickness measurements will be more precise, because the grain boundaries influence the oxide layer and a constant oxide layer is needed for the thickness measurements. But on the other hand, only limited areas can be measured by an electron backscatter diffraction (EBSD) measurement. The compromise was to choose a grain size around 20 µm.

To find the right temperature, a heating system called ”Torf” at the IPP was used. It is an evacuated electron heating system and the temperature is measured by infrared measurement on the sample surface. The reason for using this heating system is that each sample can be recrystallized at different temperatures. Only three minutes are sufficient for the whole recrystallization process. To achieve grains around 20 µm, the appropriate temperature was 2100 K.

The next step was to produce many tungsten samples with grain sizes of approximately 20 µm. For this step, the heating system called HORST was used. 40 tungsten samples were recrystallized at 2100 K. To ensure that all samples had reached the target temperature, the incubation time was set to 35 minutes, because the temperature was measured in the heater and not directly on the sample.

3.2 Preparation of Tungsten Surfaces

As stated before, for an accurate determination of the thickness of the oxide layer, a flat surface is required before starting an oxidation experiment. This is achieved by grinding and electropolishing. Using this sample preparation, oxides and other impurities are removed from the sample surface.

3.2.1 Instruments: Grinding and Electropolishing Equipment

Two machines were used for the sample preparation. The sample was fixed with a double-sided adhesive tape on a metal cylinder and mounted into the grinding machine. A picture of this machine is shown in figure 15(a). During grinding, the sample was cooled with water. Several variables like pressure, time and revolutions per minute (RPM) can be controlled using the machine.

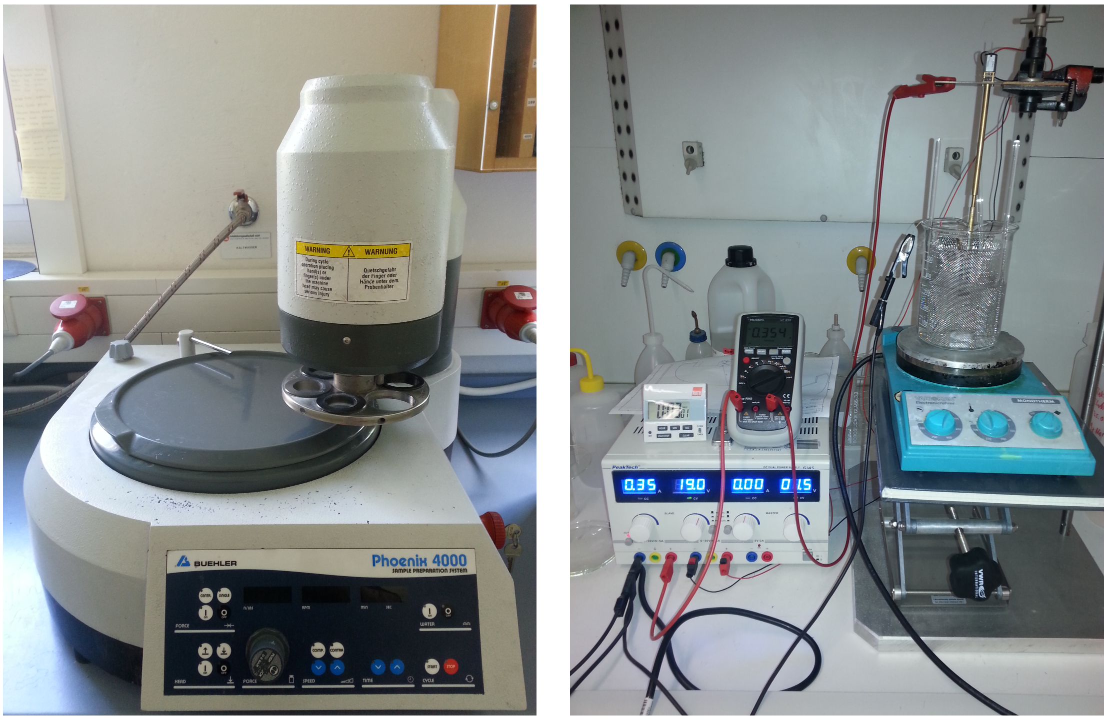

(a) ”Phoenix 4000” grinding machine. (b) Electropolishing machine.

Figure 15: Machines which are used to prepare the tungsten samples for the oxidation experiments.

The electropolishing setup was assembled by Armin Manhard from IPP. A picture of this machine is shown in figure 15(b). To achieve a standard polishing result,

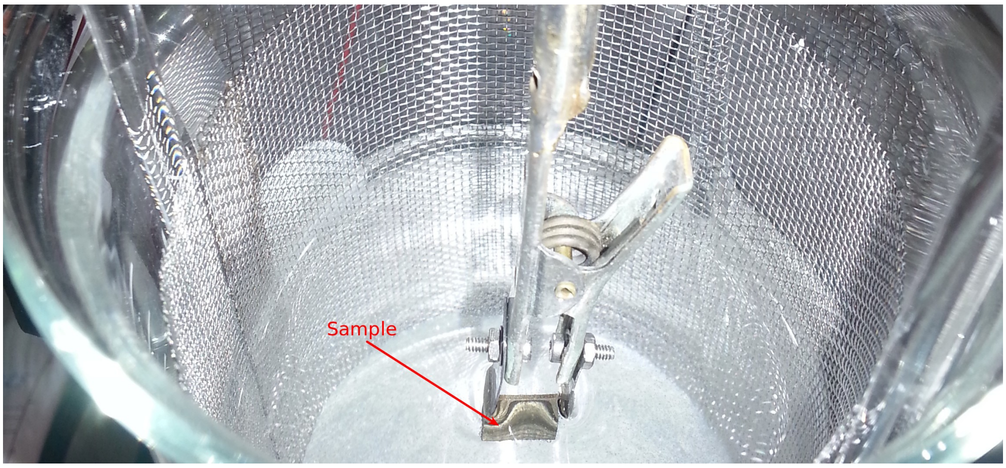

Figure 16: Fixing the tungsten sample onto the crocodile clip. The material on the top of the crocodile clip is tungsten as well. The metal mesh is the cathode and the sample is the anode. The voltage was 19 V during the electropolishing process.

variables like current, time, voltage and mixing of the electrolyte are controlled. The sample is fixed with a crocodile clip as shown in figure 16. The material at the top of the crocodile clip is tungsten as well as the sample. This gives the opportunity to plunge the full sample into the electrolyte. With this technique, both sides of the sample are polished at the same time.

3.2.2 Grinding Procedure

Table 2: Grinding and polishing steps for preparation of the tungsten surface recommended by Gabriele Matern from IPP.

Granular / P	Time / s	Pressure /LBS	Rotation / RPM
400	30	10	150
800	30	10	150
1200	30	10	150
2500	60	10	150
4000	60	10	150
Liquid Red (Bio Diament)	900	20	150
SF1 Polishing Suspension	1200	20	150
Water	300	20	150

The different grinding steps for the first oxidation experiments are shown in table 2.

After grinding, the surface was polished mechanically with Liquid Red (Bio Diament) for 15 minutes (min), a pressure of 20 pound-force (LBS) and 150 RPM. Afterwards, the tungsten sample was polished with the liquid SF1 Polishing Suspension for 20 min, a pressure of 20 LBS and 150 RPM. Finally, the sample was washed with water for 5 min, a pressure of 20 LBS and 150 RPM.

After this preparation the surface is suitable for the determination of EBSD patterns. These preparation steps were used for two oxidation experiments at 870 K.

After the first successful measurements, the procedure was optimized. Samples were ground up to P4000 (International Organization for Standardization (ISO) / Federation of European Producers of Abrasives (FEPA) grit designation) and afterwards electropolished. The advantage of electropolishing is to achieve a better surface, which means that there are virtually no grain boundaries visible. In addition, the electropolishing step is faster than mechanical polishing and both sides are polished simultaneously. In figure 17, the comparison between a mechanically polished sample and an electro polished sample is given.

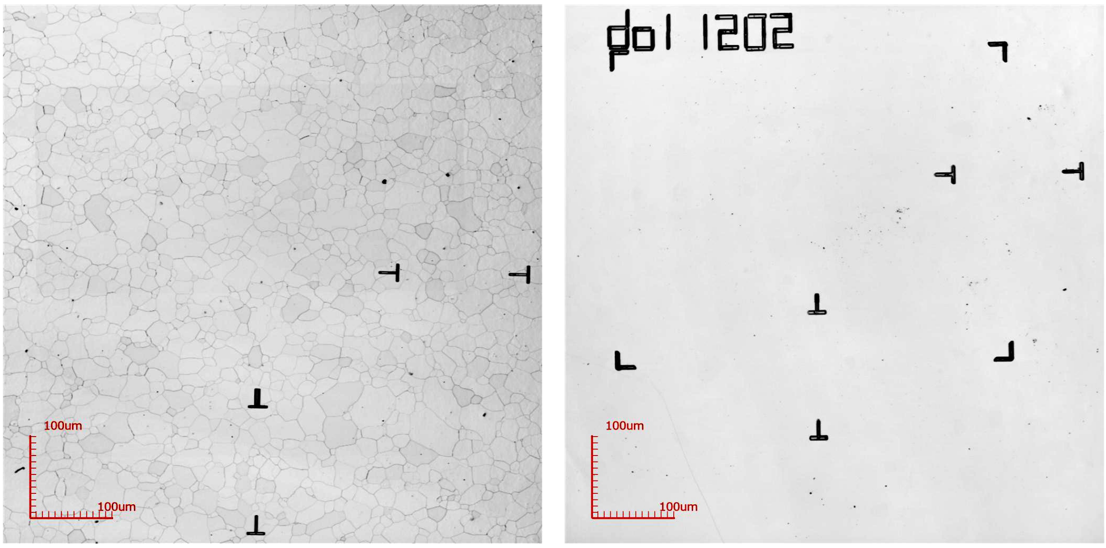

(a) Image of a mechanically polished sample. Four T markers are visible on the sample. The grain boundaries are well visible.

(b) Image of an electropolished sample. Four T markers, four L markers and the sample name are visible. In contrast to the mechanically polished sample the grain-boundaries are not visible.

Figure 17: Comparison between a mechanically polished sample on the left hand side and an electropolished sample on the right hand side.

Using the electropolishing method, the preceding grinding steps were optimized as shown in table 3. Prior to the electropolishing step, all samples were cleaned using aceton followed by an isopropanol wash.

Table 3: Grinding steps for preparation of the tungsten surface before electropolishing.

Granular / P	Time / s	Pressure /LBS	Rotation / RPM
400	30	10	150
800	30	10	150
1200	60	10	150
2500	60	10	150
4000	120	10	150

3.2.3 Electropolishing Procedure

A 1.5 % NaOH solution was used as electrolyte at a voltage of 19 Volt. This procedure was established by Armin Manhard from IPP.

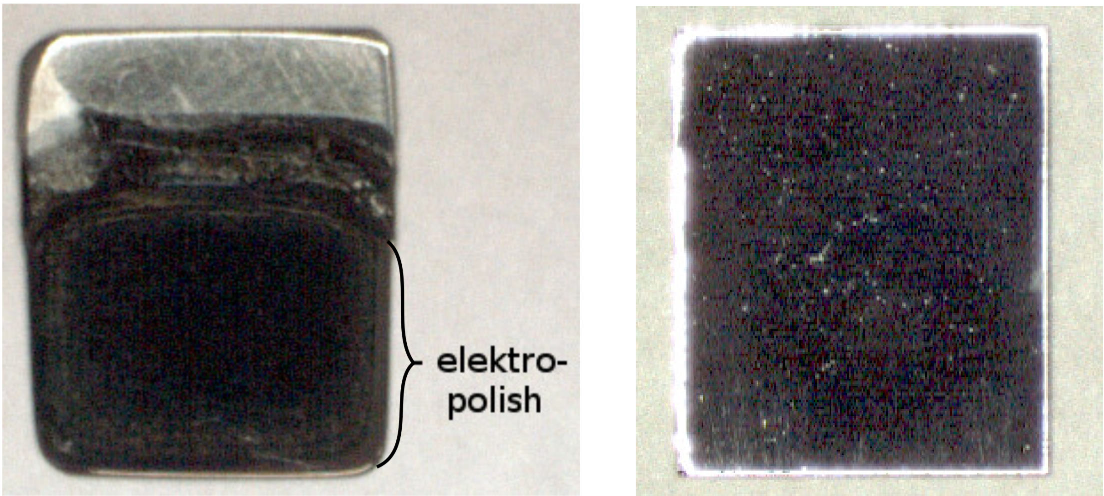

(a) Electropolished sample with a stirring speed of 700 RPM. The sample was not completely dipped into the electrolyte solution. Therefore, only twothirds of the sample is polished.

(b) Electropolished sample with a stirring speed of 150 RPM. The sample was completely dipped into the electrolyte solution. Therefore, the whole sample is polished.

Figure 18: Comparison of different stirring speeds. An electropolished sample with a stirring speed of 700 RPM is shown on the left hand side and an electropolished sample with a stirring speed of 150 RPM is shown on the right hand side. The erosion is faster with higher stirring speed. This is visible by the rounded edges on the sample.

Figure 18(a) shows a tungsten sample which was not completely dipped into the electolyte and therefore not completely polished. The electropolishing was applied for five minutes with a stirring speed of 700 RPM in the electrolyte. The current was around 1.2 A with a voltage of 19 Volt. With these settings, significant variations around 500 nm in height are observed on the electropolished surface, which are too high for an accurate determination of the thickness of the oxide layer.

The process was slowed down for optimization. The stirring speed was reduced from 700 RPM to 150 RPM. Because of that the current drops from 1.2 A to 0.4 A. The electropolish was applied for seven minutes with a constant voltage of 19 Volt.

A sample after the polishing is shown in figure 18(b). This sample shows a lower erosion rate than the sample in figure 18(a). With these settings, the height variations are smaller and around 100 nm. This is shown in figure 19. These height variations are acceptable and should have a negligible effect on the oxidation measurements which show height differences up to 4000 nm.

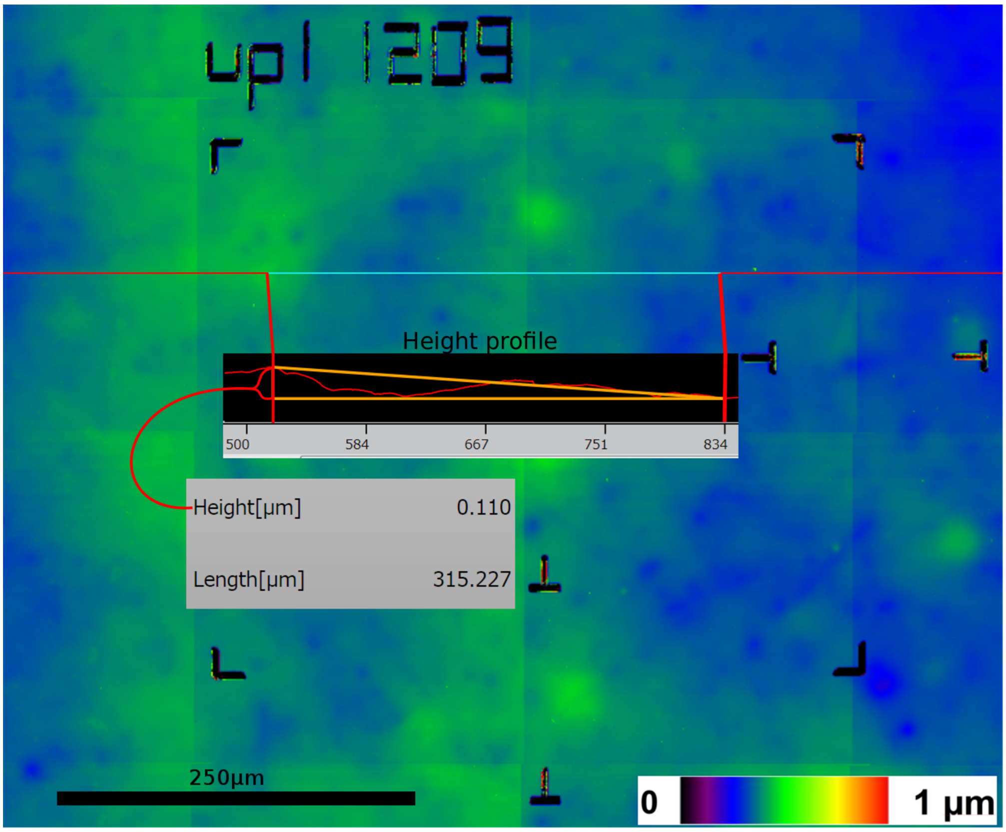

Figure 19: A height profile image of an electropolished sample is shown. The color scale of the height is on the bottom right side. This image consists of 16 pictures taken by the CLSM with a 50 times magnification objective and is stitched together. The lines are artifacts of the stitching procedure. The red/blue line gives the height profile and is shown in the inserted graph. The triangle therein shows a height difference of about 110 nm.

3.3 Scanning Electron Microscope

The scanning electron microscope (SEM), equipped with a focused ion beam and an EBSD detector, was used to take pictures, to set markers on the sample, to measure the orientation of the grains, and to measure the thickness of the oxide layer.

3.3.1 Instrument: SEM Device HELIOS

For the experiment the SEM device ”HELIOS NanoLab 600” from Field Electron and Ion Co. (FEI) is used. This SEM has, in addition to a field emission electron gun for SEM-pictures, an energy dispersive X-ray spectroscopy (EDX) detector, a FIB (gallium$^+$-gun) e.g. for cross-sections, a gas injection system (GIS) for platinum-carbon (Pt-C) coating and an EBSD-detector to measure the grain orientation.

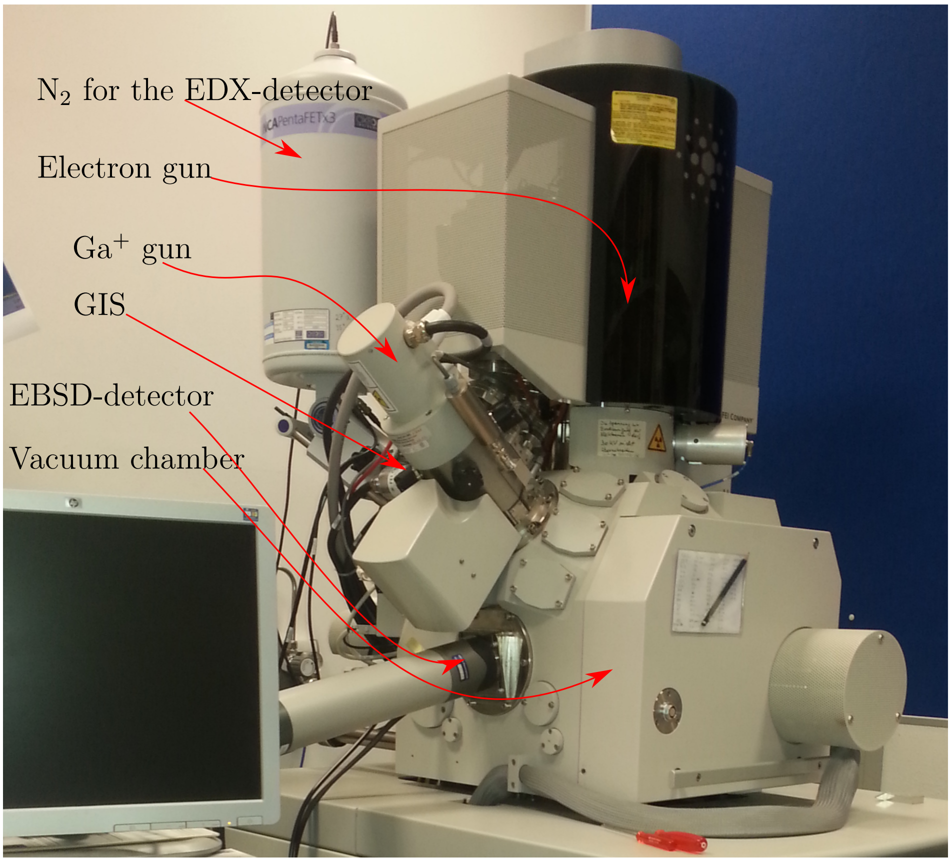

Figure 20: Picture of the SEM device HELIOS. This SEM has, in addition to a normal SEM, some extensions which are marked in the picture.

An image of the machine is shown in figure 20. Standard settings for imaging are an accelerating voltage of 5 kV for the electron beam and a current of around 0.69 nA.

3.3.2 Marking of Samples

After sample polishing, T markers on the sample are prepared using the FIB. The resulting T markers are shown in figure 21(a). The markers allow a comfortable localization of the same position before and after the oxidation in all measurement systems.

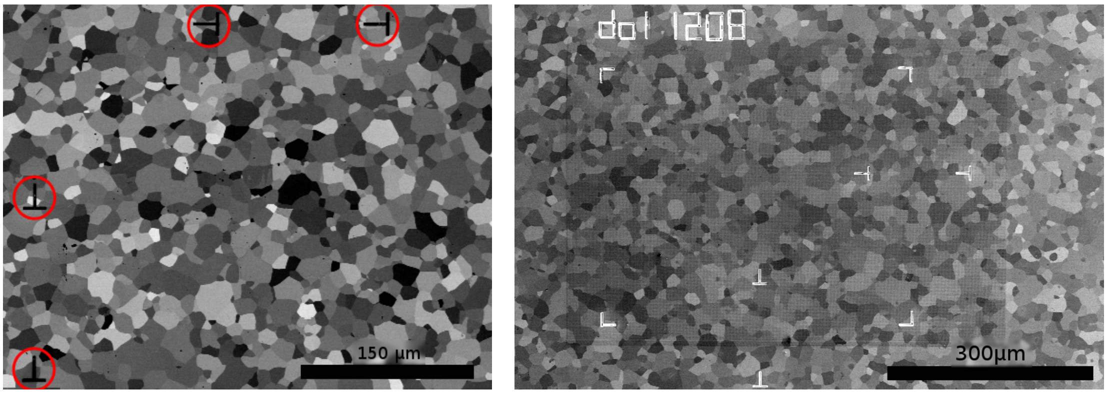

(a) SEM image taken with a backscatter detector. Four T markers are visible on the tungsten sample. By merging EBSD data and CLSM data it was learned that additional markers are useful.

(b) SEM image taken with an ETD detector. Four T markers and four L markers are visible on the tungsten sample. In addition to the markers, the sample name is labeled wtih FIB. This avoids errors in the merging procedure from different measurment systems.

Figure 21: On the left hand side a tungsten sample with four T markers is shown. On the right hand side a tungsten sample with four T markers, four L markers and the sample name is shown.

Four T markers are sufficient to find the correct position in an overlay. Pictures taken with different measurement systems show variable aberrations. Therefore, additional markers are required to correct errors like lens errors, image distortion or rotation in an overlay of the sample.

Additional L markers were prepared with a FIB on the sample as shown in figure 21(b). Also the sample name is labeled near by the markers to avoid mistakes. These steps were introduced for the optimization during the development of the method.

3.3.3 Analysis by EBSD using SEM

The grain orientations were measured and analyzed by electron backscatter diffraction. The HELIOS was also used for this. For this measurement, the electron accelerating voltage was set to 20 kV and the electron current was approximately 1.4 nA. A tilt angle of 57° between the electron beam and the surface was taken to get Kikuchi patterns. These settings were used for all EBSD analyses. An example of a colored orientation map is shown in figure 12.

Low indexed surfaces were evaluated with two different deviations of the orientations. The thickness measurement was evaluated with a deviation of ±5° and ±10° of the Euler angle for the low indexed surfaces. But the results of both evaluations were equivalent. It was expected that the standard deviation of the thickness measurement should be lower by lower deviation of the orientation.

The standard deviation of the thickness measurement was around 0.2 µm. The oxide layer on a single grain had a variation of 0.3 µm and was in the same range.

3.3.4 Cross-sections using FIB

Cross-sections of an oxidized tungsten sample are used to measure the absolute thickness of the oxide layer. The cross-sections were prepared by FIB. The beam profile of the ion beam (as well the electron beam) is not constant and has a peak with tails. This means that by making a cross-section, the edge of the oxide layer is rounded.

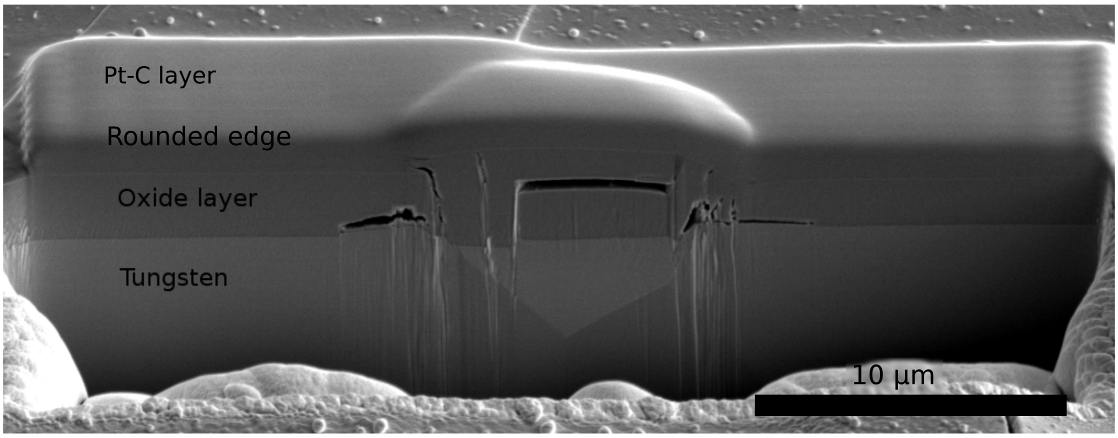

Figure 22: Cross-section of a recrystallized and oxidized tungsten sample. The Pt-C layer, tungsten oxide layer, the tungsten grain, and the rounded edge are labeled.

With a rounded edge the thickness of the oxide layer is hardly to measure. Therefore, the gas injection system was used to deposit a Pt-C layer. The Pt-C layer protects the edge of the oxide layer and an accurate thickness measurement is possible. In figure 22 an example of a cross-section is shown and the Pt-C layer, tungsten oxide layer, the tungsten grain, and the rounded edge are labeled.

3.4 Confocal Laser Scanning Microscopy

The confocal laser scanning microscope (CLSM) can be used to determine height differences on surfaces. The measurements are fast, compared to a thickness measurement using the cross-section technique as described in the previous section. The results are height profiles of the oxidized samples.

3.4.1 Instrument: Olympus LEXT OLS4000

The CLSM device Olympus LEXT OLS4000 was used to take images before and after the oxidation. The microscope together with the software allows one to obtain 3D data and takes optical images and laser images.

A picture of the microscope is shown in figure 23(a). The image of the first samples were taken with a 20x magnification objective. This was done during the method development. Afterwards, the pictures of the oxidized grains were taken with a 50x magnification objective.

The advantage of the 20x magnification objective is that just one image is required to analyze a sufficient number of grains. The area resolved by the CLSM is large enough that the EBSD data fit in.

The 50x magnification objective allows to resolve more details in the image. But at least nine images are required to cover the area of the EBSD data. The images were stitched together by the CLSM software and can be evaluated.

Images were taken with a 20x magnification objective to study possible errors by stitching. It was unknown how well the stitching software merges images together. Later, the comparison between 20x and 50x magnification objective showed that the stitching software works adequately.

From that time on, the 50x magnification objective was used because of the higher quality.

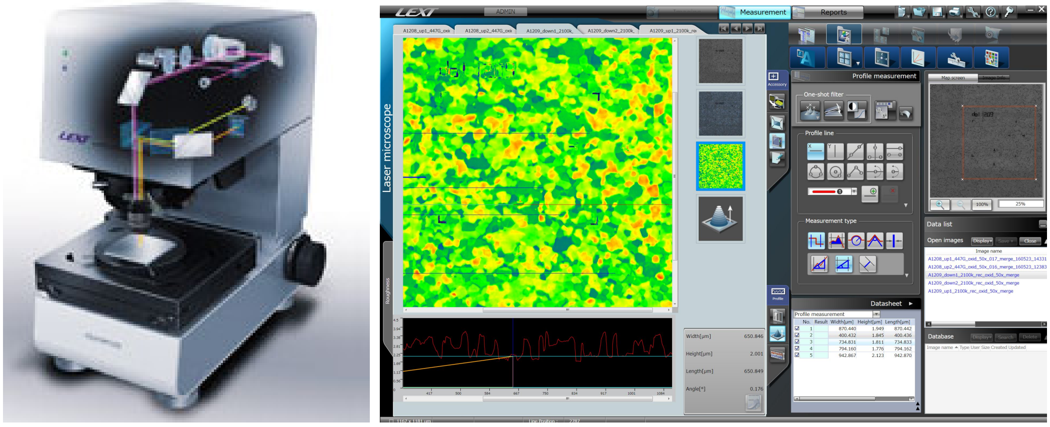

(a) Picture of Olympus LEXT OLS4000[31].

(b) Screenshot of the CLSM software.

Figure 23: The left hand side shows a screen shot of the software and the right hand side shows the microscope.

3.4.2 Analysis of Relative Height

For measuring the height, the software from the CLSM is used. A screenshot of a measurement for one height value of one grain is shown in figure 23(b).

To compare different height measurements, a reference level must be defined. The grain orientation {100} has the highest oxidation rate. The samples have many grains in this orientation. Therefore, this grain orientation is optimal to adjust the relative height information from different measurements. The height of the mean value of the grains with the orientation {100} is set to zero, as the reference level. Relative to this reference level the differences between heights are measured.

3.5 Oxidation of Tungsten

The goal was to achieve an oxide layer with a thickness between 3 µm and 4 µm. The reason is on the one hand that the confocal laser scanning microscope is able to measure the height differences of the oxide layer around 1 µm between grains. On the other hand, the influence of the surrounding oxidized grains should be still insignificant. The grain size is around 20 µm. If the oxide layer is in the same range, the surrounding grains will influence the oxide layer and a grain dependent measurement would be distorted.

Furthermore, the oxide layer extends into the depth, beneath the initial surface level. Therefore, the oxidation can reach a second grain beneath the surface and the oxidation takes place at two different grains. This is discussed in subsection 3.5.2.

To study the oxidation dependency on the grain orientation, evaporation of tungsten oxide should be avoided. The temperature during the oxidation should be under the evaporation temperature of tungsten oxide which is 1020 K[12]. The absence of evaporation is verified at a temperature of 870 K and discussed in subsection 3.5.3.

The first goal of this master thesis was to develop a method for grain dependent oxidation. The second goal was to verify this method and compare it to gravimetric analyses. Third, the method should be applied to determine grain orientated oxidation at different temperatures.

During method development, the samples were oxidized at 870 K for 30 min in a 20 % oxygen/80 % argon atmosphere. At this temperature, tungsten oxide does not evaporate and the oxidation time is short enough to perform a few experiments per day for parameter optimization.

3.5.1 Instrument: Thermobalance

The thermobalance allows a simultaneous thermal analysis (STA) of different parameters in real-time. In this master thesis, the thermogravimetric analysis (TGA) function was used. For that purpose, the STA 449 F1 Jupiter manufactured by Netzsch was used. It combines a real-time measurement of weight change, temperature and gas flow.

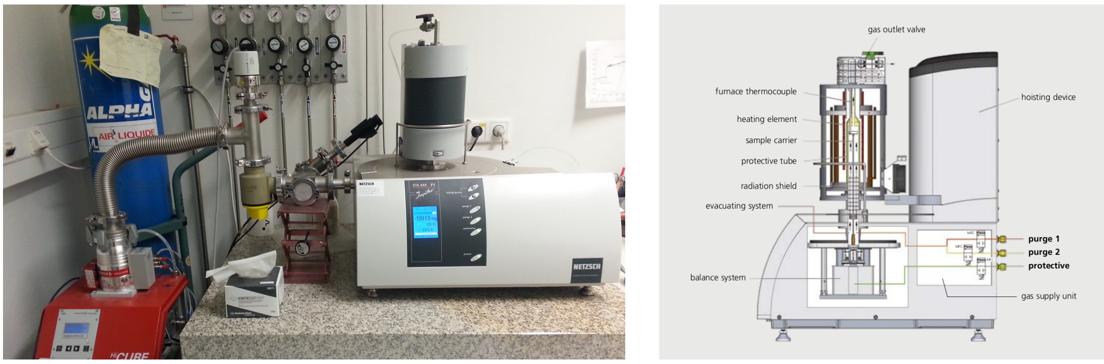

(a) The TGA system and the vacuum system used in the laboratory.

(b) Assembly scheme of the thermobalance 449 F1 Jupiter.[32]

Figure 24: Picture of the thermobalance 449 F1 Jupiter and of the assembly scheme of the thermobalance.

A picture of the instrument is shown in figure 24(a). The thermobalance has three gas connections. This is shown in figure 24(b). The gas flows from the bottom to the top. In the experiment argon (purity of 99.9999 %) was connected to the gas valve "protective" and "purge 2". Oxygen was connected to the gas valve "purge 1".

During the oxidation time, a 20 % oxygen/80 % argon atmosphere was used. Before and after oxidation, only argon flowed through the system. A vacuum pump was used to achieve a clean chamber. Therefore, a pressure under 2.5×10^{-5} mbar was produced to clean the chamber from water, oxygen and other gases. Afterwards, the system was flushed with argon for one minute.

3.5.2 Thickness and Variation of Oxide Layer

An oxide layer with a thickness of around 4 µm is aimed for the experiment. The thickness of the oxide layer must be sufficient to measure the height differences between oxidized grains of different lattice plane orientations. The influence of the surrounding oxidized grains should be negligible.

Therefore, the size of the grains should be large enough to minimize the influence of grain boundaries in order to get a homogeneously thick oxide layer for reliable measurements. A cross-section of a grain boundary is shown in figure 25(a).

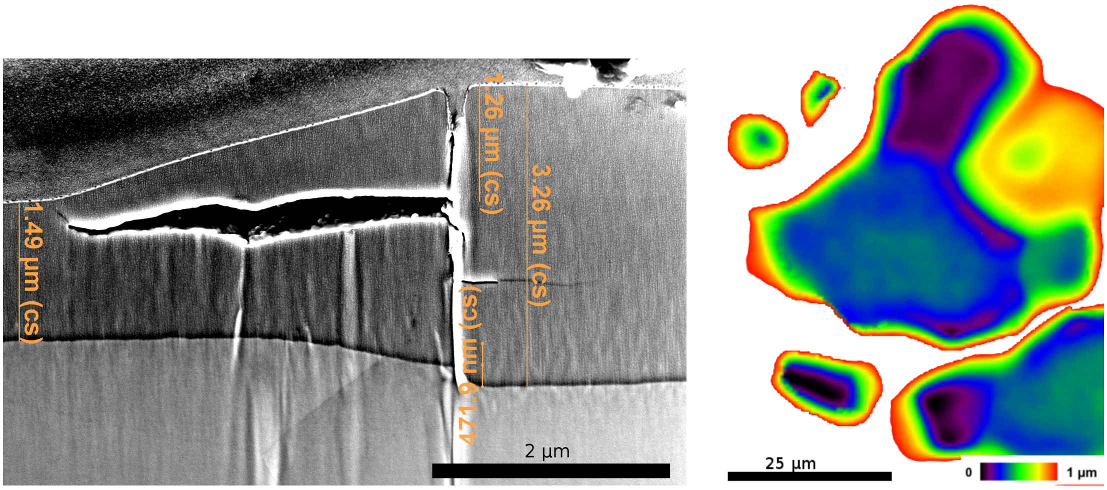

(a) A cross-section at a grain boundary. A Pt-C layer to protect the oxide layer is seen on top. Tungsten is located under the oxide layer. The thickness of the oxide layer is marked by orange lines. Two different grains have different oxidation rates. The influence of the grain-boundary on the oxidation rate is around 4 µm in distance.

(b) A height profile image from the CLSM. The grain boundary effect is shown.

Figure 25: Variation of the oxide layer at grain boundaries. On the left hand side a cross-section of a SEM micrograph and on the right hand side a height profile image obtained with the CLSM is shown. The grain boundaries effect the oxide layer around 4 µm in distance.

The oxide layer varies around 1.3 µm in height and 4 µm in the distance between two grains. This is also observed and confirmed using the CLSM. A height profile image obtained with the CLSM is shown in figure 25(b). There are different grains and the oxide layer varies around 1 µm in height and 6 µm in distance between neighboring grains. Therefore, large enough grains are needed to get reliable thickness measurements of the oxide layer.

In addition to the effect of grain boundaries, the oxide layer can vary over the same grain. An example is shown in figure 26. The oxide layer varied about 300 nm over one grain. Reasons could be that the oxidation took place on two different grains.

On a tungsten surface, the tungsten oxide expands around 70 % above and 30 % below the original surface level (this is discussed in chapter 5.1.3). This means, an oxide layer of 4 µm is approximately 1 µm below the original tungsten surface. Therefore, oxidation could take place on two different grains.

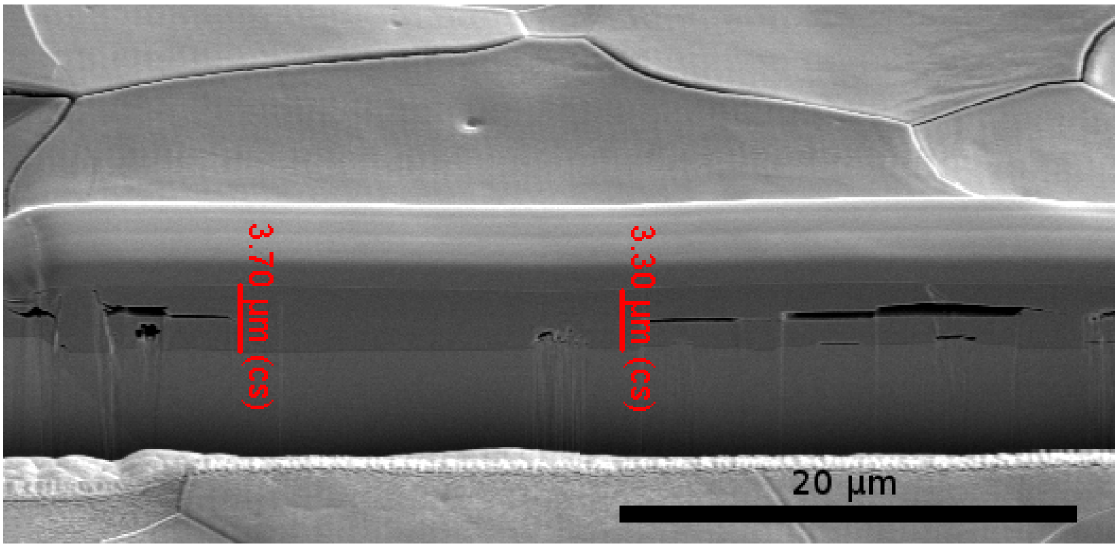

Figure 26: A cross-section over one grain. Pt-C layer is coated on top to cover the oxide layer. The oxide layer is marked red by the measurement lines and under the oxide layer tungsten is situated. The oxide layer varied about 300 nm over the same grain.

3.5.3 Tungsten Oxidation in Argon Atmosphere

The highest used temperature for oxidation was 870 K. Most of the experiments were done at this temperature. In order to interpret the results, effects like oxidation of tungsten in argon atmosphere by impurities should be investigated. Therefore, a non-oxidized sample was put into the TGA system and a standard incubation was performed at 870 K without oxygen.

This means, only argon was in the TGA system during the experiment. Without oxygen, the sample should not have any mass change. This was confirmed using gravimetric analysis systems.

The TGA and an analytical balance were used for the analyses. The analytical balance was used to measure the weight of the sample before and after the incubation. During the incubation the weight measurement was measured with the TGA system.

The measurements of the analytical balance are listed in table 4. The non-oxidized sample A1189 showed a weight difference of 0.02 mg after the incubation. No relevant mass change was obtained for grain dependent oxidation experiments. In addition, the visual inspection of the surface showed no sign of an oxidation. The sample was adequately polished and no color change was observed which would indicate an oxidation film. This showed that the TGA system had negligible oxidizing impurities in argon atmosphere and that the system had no leaks.

Table 4: Measurements obtained with the analytic balance before and after the incubation in argon atmosphere. This was done at a temperature of 870 K for 30 min. The mass differences (Δ mass) were insignificant so that no evaporation or oxidation was observed under argon atmosphere.

Sample	Oxidized sample	Mass before	After oxidation /mg	Δ mass /mg
A1187	Yes	1595.329	1595.331	0.00
A1189	No	1588.352	1588.372	0.02

Habainy and Nilsson[33] showed that the oxidation rate is around $5 \times 10^{-6} \frac{\text{mg}}{\text{cm}^2 \cdot \text{s}}$ under argon atmosphere with an oxygen partial pressure of $\leq 5 \cdot 10^{-6}$ standard atmosphere (atm) and at a temperature of 820 K. This is a low oxidation rate, comparable to our oxidation experiment under argon atmosphere, and is in the range of the error of the measurement system STA 449 F1 Jupiter. Both TGA systems are comparable.

In addition, the evaporation of tungsten oxide should be investigated at the highest temperature at 870 K. Therefore, the oxidized sample A1187 was put into the TGA system and the same experiment was performed under argon atmosphere a second time.

The graph in figure 27 shows the temperature, mass, gas flow and time during the incubation. The mass is constant and does not change during the incubation at a temperature of 870 K. If tungsten oxide evaporates, there will be a decrease of mass during the incubation. If tungsten oxidizes, there will be an increase of mass during the incubation. It could be a small oxidation and evaporation at the same time but it can be assumed that these processes are very slow. In addition, the weight of the sample was measured by the analytical balance. The mass difference was insignificant which is shown in table 4. This means that there is no evaporation of tungsten oxide measured under argon atmosphere.

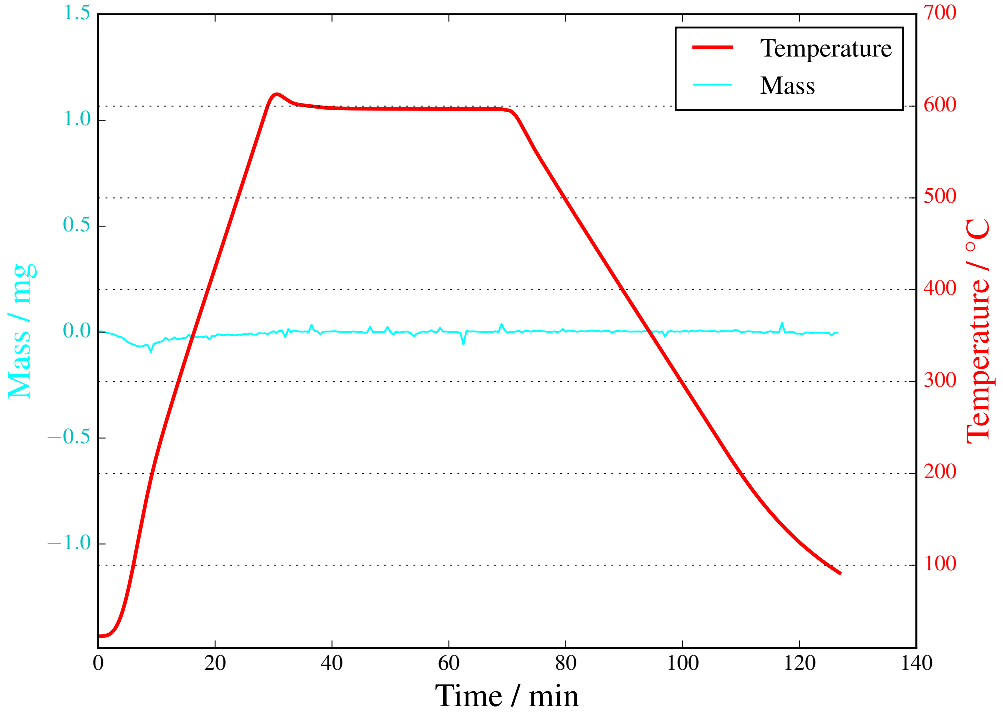

Figure 27: Evaporation of tungsten oxide. The time is shown on the x-axis and the temperature on the right and the mass on the left hand side on the y-axis.
An oxidized sample was put into the TGA system and was heated up to 870 K for 30 min to check if the tungsten oxide evaporates. Evaporation of tungsten oxide is not observed.

To summarize, it is shown that evaporation and oxidation under argon atmosphere can be neglected for determining the oxidation rate. The samples are in a stable condition and the start of the oxidation process can be trigged by changing the gas flow from 100 % argon to 20 % oxygen/80 % argon atmosphere.

3.5.4 Parameters at Thermogravimetric Analysis

The following parameters are adjustable in the TGA:

- Temperature
- Time
- Gas flow
- Speed of heating and cooling
- Sample position on the sample holder

The time must be adjusted to reach the aim having the same thickness of the oxide layer for different temperatures. Therefore, the influence of gas flow, speed of heating and cooling, and sample position on the sample holder will be discussed in the following subsections.

3.5.5 Gas Flow during Thermogravimetric Analysis

The gas flow is a parameter of the TGA which can be varied and is 160 ccm/min in our oxidation experiments. Netzsch (the manufacturer of the TGA) recommends a gas flow between 120 ccm/min to 200 ccm/min. To see if there is an effect related to the gas flow, a comparison of our standard oxidation at 870 K was performed. Therefore, an oxidation with a gas flow of 160 ccm/min and a second oxidation with a gas flow of 40 ccm/min were performed.

Table 5: Gas flow experiment using the TGA. Measurement of the masses before and after the oxidation. The mass difference (Δ mass) between the two oxidations are negligible, which means that the gas flow does not have a significant effect on the incubation.

Sample	Gas flow /$\frac{\text{ccm}}{\text{min}}$	Mass before	After oxidation /mg	Δ mass /mg
A1198	160	1748.087	1748.855	0.768
A1199	40	1600.606	1601.360	0.754

The mass difference between the two measurements is shown in figure 28. The mass difference is constant during the whole oxidation. This means the gas flow does not affect the oxidation. In addition, the masses are measured before and after the oxidation using an analytical balance. The result is shown in table 5. There are no significant differences between the two oxidations.

The data of the two individual measurements of the TGA are shown in figure 57 and 58 in the appendix.

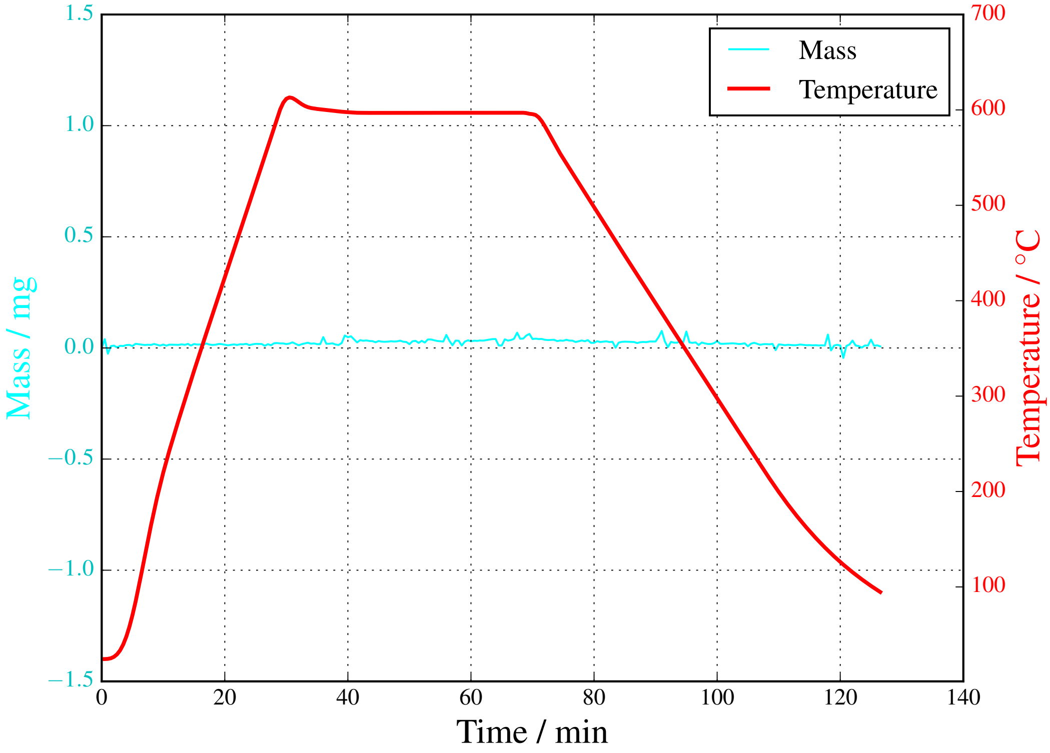

Figure 28: Gas flow experiment using the TGA. The time is shown on the x-axis and the temperature on the right and the mass on the left hand side on the y-axis. The mass difference between the 160 ccm/min and the 40 ccm/min incubation is shown. The data of the two individual incubations are shown in figure 57 and 58 in the appendix. The mass difference of the two incubations is constant, which means that the gas flow does not have a significant effect on the incubation.

3.5.6 Speed of Heating and Cooling

During heating up the sample and the chamber the gas expands. During cooling down the sample and the chamber, the opposite effect occurs. If the gas flow in the chamber is set too low, gas from the environment can enter the chamber.

This was one of the reasons why the gas flow experiment, discussed in the last section, was performed at the low gas flow of 40 ccm/min. A gas flow of 160 ccm/min was used for all oxidation experiments. This gas flow is so high that an expansion or contraction effect can be compensated.

The heating and cooling is performed under argon atmosphere. The $20\,\frac{\mathrm{K}}{\mathrm{min}}$ heating or $10\,\frac{\mathrm{K}}{\mathrm{min}}$ cooling speed should not affect the oxidation experiment. Tungsten has a high thermal conductivity of $173\,\frac{\mathrm{W}}{\mathrm{m}\cdot\mathrm{K}}$. Therefore, there should be no stress strain during the heating or cooling process. Also chemical reactions can be neglected because the heating or cooling process takes place under argon atmosphere. In chapter 3.5.3 is shown that there are negligible reactions under argon atmosphere at 870 K which influence the gravimetric analysis.

3.5.7 Sample Position on the sample holder

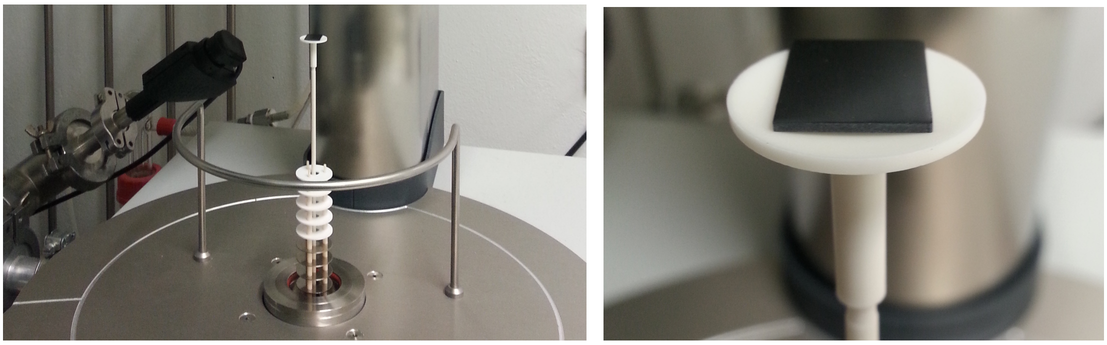

(a) The TGA system with opened chamber. The sample holder and an oxidized tungsten sample on top of the sample holder are shown.

(b) The sample holder with an oxidized tungsten sample. The upper side of the sample is facing to the atmosphere and the lower side of the sample is facing to the sample holder.

Figure 29: Position of the sample on the sample holder.

In figure 29, the TGA system with an oxidized tungsten sample is shown. The tungsten oxide is the black layer on the surface. The upper side of the sample in figure 29 is facing to the atmosphere and the lower side of the sample is facing to the sample holder.

The question was: Have both sides the same thickness of the oxide layer and therefore the same oxidation rate? The gas flow on the lower side of the sample is lower. Therefore, the oxygen concentration could be lower and influence the oxidation.

To check the oxidation rate on both sides, 14 cross-sections on each side were performed using FIB-SEM. The focus was on the {100} crystal orientation, because this orientation has the highest oxidation rate (shown in chapter 5.1) and therefore, it was expected that the influence on oxygen is higher.

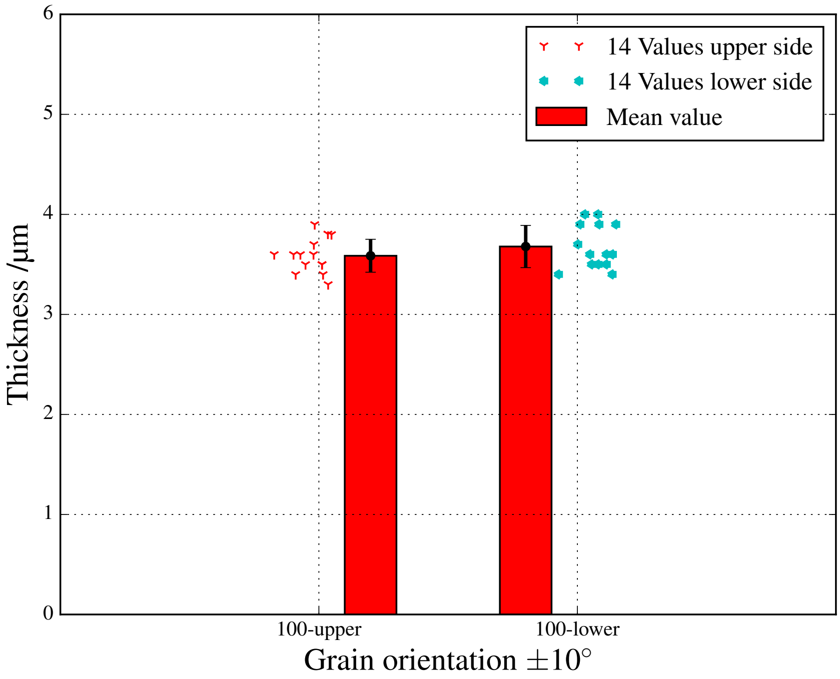

Figure 30: Thickness of the oxide layer. The thickness was measured on cross-sections using a SEM. The lower side is facing to the sample holder and the upper side is facing to the atmosphere. The thickness of the oxide layer is nearly the same, which means that the position of the sample on the sample holder does not have any effect on the incubation.

Figure 30 shows the thickness of the oxide layer at the lower and upper side of the sample. Both sides have nearly the same oxide layer thickness. This means that the transported oxygen is not the limiting factor at this temperature and comparable to the results of the gas flow experiments in the previous chapter.

Because there is no effect of the oxidation rate on either sides of the sample, the thickness analysis of the oxide layer on both sides can be used to increase speed of the measurements for different grain orientations.

3.6 Overview of Possible Parameters which Influence the Oxidation

The different effects on the oxidation procedure and the subsequent analysis of the oxide layer are shown in table 6 to give an overview of chapter 3.

Table 6: Overview of different effects on the oxidation procedure and the subsequent analysis of the oxide layer.

Oxidation	**Parameter**	**Result**
Sample position on the holder	upper and lower side	no influence (3.5.7)
Gas flow variation	40-160 ccm/min	no influence (3.5.5)
Speed of heating and cooling	$20\,\frac{\mathrm{K}}{\mathrm{min}}/10\,\frac{\mathrm{K}}{\mathrm{min}}$	no influence (3.5.6)
Temperature	720-870 K	influence on oxidation rate
Time	0.5-96 h	influence on oxide layer
Outgassing of tungsten	870 K in argon	no outgassing (3.5.3)
Evaporation of tungsten oxide	870 K in argon	no evaporation (3.5.3)

Analysis		
Depth growth/oxidation height	30 % / 70 %	influence the analyses (5.1.3)
Variation of the oxide layer	$\sim$300 nm	small influence (3.5.2)
Grain dependent electropolishing	$\sim$50 nm	negligible influence (5.1.3)
Grain boundaries	Grain size $\sim$20 µm	select big grains (3.1.2)
Grain orientation	±5° to ±10°	no influence (3.3.3)

4 Overview: Final Method

The method development was done at an oxidation temperature of 870 K. After optimizing the method, a standardized experimental procedure was used for all samples which is described in section 4.1. The evaluation of the data is summarized in section 4.2.

4.1 Experiment

The tungsten samples were recrystallized at a temperature of 2100 K. Details are described in section 3.1. Afterwards, the samples were ground. The grinding steps are shown in table 3 in subsection 3.2.3. The samples had a flat, oxide free surface. Afterwards, the samples were cleaned and electropolished to reduce roughness and to improve the surface quality. The electropolishing took around seven minutes in a 1.5 % NaOH solution. A constant voltage of 19 V was used and the current was around 0.5 A (subsection 3.2.3). For further experiments, including EBSD analysis, clean surfaces are required. Therefore, the sample has to be cleaned first with aceton and then with isopropanol.

In the next step, makers were created on the sample using a FIB (shown in figure 21(b)) and the grain orientation was measured by EBSD (subsection 3.3.3). The pre-characterization using EBSD is the most time consuming step in the experiments. Afterwards, the sample was checked with the CLSM for surface cleanliness and roughness, and the weight of the sample was measured with an analytical balance.

After these steps, the sample was ready for the oxidation experiment in the TGA. Therefore, the sample was put into the TGA system and the oxidation experiment was controled by the TGA software. For all oxidation experiments, the same heating rate of 20 $\frac{\mathrm{K}}{\mathrm{min}}$ was applied and the heating was performed in argon atmosphere. The target temperature was between 720 K and 870 K. The target temperature was hold for 10 min before the oxidation was started with a 20 % oxygen/80 % argon atmosphere. The oxidation time depends on the experiment and was between 30 min and 5760 min (96 h). The oxidation was stopped by flushing the chamber with argon. Afterwards, the chamber of the TGA system was cooled down with a cooling rate of 10 $\frac{\mathrm{K}}{\mathrm{min}}$ (chapter 3.5).

After the cooling procedure, the sample weight was measured again with the analytical balance. The mass difference of the measurement before and after the oxidation gives the amount of oxygen and therefore the amount of tungsten oxide can be calculated.

After the gravimetric analysis, the relative height and the absolute thickness are measured using the CLSM system (section 3.4) and the SEM device Helios (section 3.3), respectively.

4.2 Evaluation and Merging of the Data

The developed method comprises four main steps for the evaluation of the data.

- Measurement of the relative height from an oxidized sample with the CLSM
- Assignment of the relative height to the crystal orientation by overlaying of a CLSM image and an EBSD map
- Verification of the absolute thickness of the grain with the {100} orientation by cross-sections with FIB

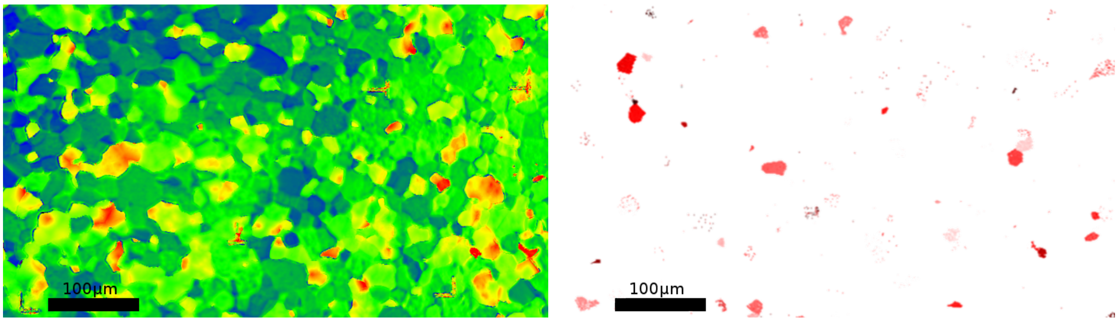

(a) An image obtained with a CLSM. This is a height profile image. Red is the highest point and blue the lowest point.

(b) An EBSD image obtained with a SEM. The red labeled grains have the crystal orientation {100} ±10°.

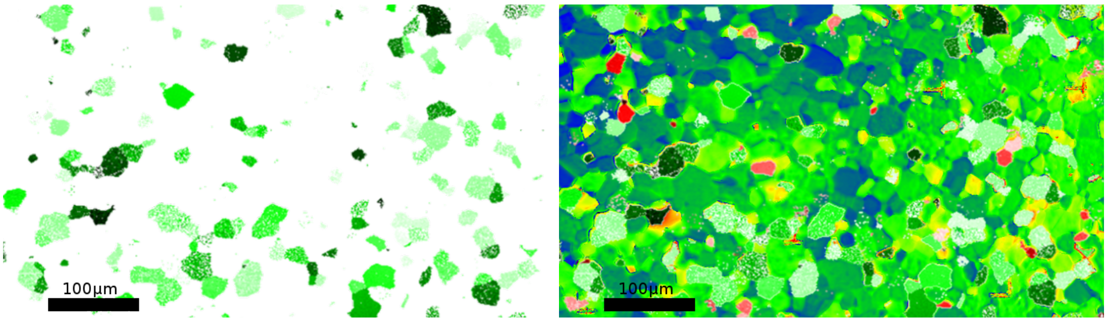

(c) An EBSD image obtained with a SEM. The green labeled grains have the crystal orientation {110} ±10°.

(d) An overlay of image a, b and c. Height measurements can be associated to a crystal orientation.

Figure 31: An example of merging the data is shown. The images (a) to (c) are overlaid in image (d).

- Leveling of the relative height on the {100} orientation and calculating the total height for the other orientations

EBSD data and the relative height data from the CLSM are merged manually by overlaying the images. For this aim a graphic tool called GIMP was used. In figure 31 an example of an overlay is shown.

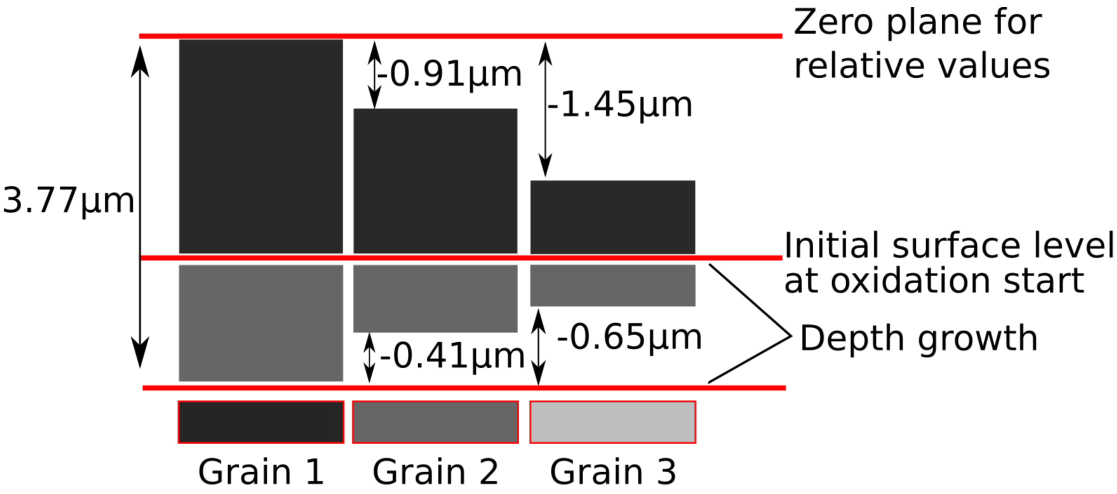

Figure 32: Schematical figure to illustrate the growth of the tungsten oxide.

EBSD images (figure 31(b) and 31(c)) and a CLSM image (figure 31(a)) were overlaid (figure 31(d)) used to assign the height to the grain orientation. The relative height for each grain was extracted by the program of the CLSM shown in section 3.4.

With the SEM, the absolute values of the heights were measured on cross-sections (shown in section 3.3.4). At least eight cross-sections on each sample were done on the grains with the orientation {100} to verify the absolute height of the oxide layer. This grain orientation has the highest oxidation rate and therefore the biggest oxide layer. The relative heights from the CLSM are used to calculate the absolute height of the grain orientation {110} and {111}.

On a tungsten surface, the tungsten oxide expands around 70% above and 30% below the original surface level (this is shown in chapter 5.1.3). The oxide layer grows into the tungsten layer which must be taken into account. This is corrected by an experimentally determined correction factor. The correction factor is 0.45 and its determination is described in chapter 5.1.3. An example of the calculated absolute height is shown in table 7. The values of the table are illustrated in figure 32.

Table 7: A calculation example to calculate relative values to absolute values. The orientation {100} is the reference plane of the relative values. From this plane the relative values are calculated. "abs.", "rel." and "corr." are the abbreviations for absolute, relative and correction, respectively.

$h_{abs.\{100\}}$/µm	$h_{abs.\{100\}}$/µm	$h_{rel.\{100\}}$ /µm	$h_{corr.}$ (= $h_{rel.\{100\}} * 0.45$)
3.77	3.77	0	0

$h_{abs.\{110\}}$ /µm	$h_{abs.\{100\}}$/µm	$h_{rel.\{110\}}$ /µm	$h_{corr.}$ (= $h_{rel.\{110\}} * 0.45$)
2.45	3.77	-0.91	-0.41

$h_{abs.\{111\}}$ /µm	$h_{abs.\{100\}}$ /µm	$h_{rel.\{111\}}$ /µm	$h_{corr.}$ (= $h_{rel.\{111\}} * 0.45$)
1.67	3.77	-1.45	-0.65

For example, the height (h) of grains with {111} orientation is calculated with the following equation.

$$h_{abs.\{111\}} = h_{abs.\{100\}} + h_{rel.\{111\}} + h_{rel.\{111\}} * 0.45 \tag{4.1}$$

where $h_{abs.\{100\}}$ is the absolute height on cross-sections, $h_{rel.\{111\}}$ is the relative value of the CLSM (this value is negative and illustrated in figure 32) and the last term is the correction for the depth growth.

This procedure allows to evaluate many thickness measurements on different grains with selected orientation at one sample.

5 Results

This chapter is subdivided into three sections. Each section describes the results of one of the main goals of the master thesis.

The first section contains the results obtained during the method development of measuring the grain dependent oxidation at 870 K. This includes relative height and thickness measurements on the oxide layer. The grain dependency of the oxidation was detected by thickness measurements of the oxide layer on distinct grains. Therefore, the relative height was measured by the CLSM (subsection 5.1.1) and the absolute thickness was measured by FIB (subsection 5.1.2). The relative heights were transformed into absolute thickness data (subsection 5.1.3).

In the second section 5.2, a comparison of the thickness measurements of the oxide layer to the gravimetric analyses is shown. The gravimetric analyses were evaluated for the two borderline cases, the linear oxidation rate and the parabolic oxidation rate. The thickness data are transformed into parabolic oxidation rates in $\frac{\mathrm{mg}^2}{\mathrm{cm}^4 \cdot \mathrm{s}}$ to compare them with the gravimetric analyses.

In the third section 5.3, the developed method was applied to investigate grain dependent oxidation at four different temperatures for the low indexed orientations {100}, {110} and {111}. The oxidation rates at different temperatures were fitted using the Arrhenius equation.

A comparison of height measurements on oxidized, low indexed tungsten surfaces to height measurements on oxidized single crystals was planed. But the supplied single crystals had an insufficient surface quality and the customer complaint took several months. Also, in the second delivery the single crystals had an insufficient surface quality. Some results of the analyzed surface of the delivered single crystals are shown in the appendix A.3. The planned oxidation experiments could not be performed.

5.1 Dependence of Oxidation on the Grain Orientation

The method development for measuring the grain dependent oxidation took place in several steps. Firstly, grain dependent oxidation was evaluated by the measurement of relative heights of the oxide layer. This means that a measurement with the confocal laser scanning microscope (CLSM) gives the different heights of the oxide layer of each grain. The relative heights for up to 100 grains were evaluated individually on each sample.

The next step was to evaluate the absolute height of oxide layer dependent on the grain orientation. Therefore, the thickness of the oxide layer for grains with low indexed orientations was measured by SEM on FIB prepared cross-sections. These measurements were the basis to transform the relative height data from the CLSM into absolute thickness data.

This was done using thickness measurements of not less than eight cross-sections on different grains with the low indexed orientation. The {210} and {211} orientation were also evaluated to enlarge the data set. The mean value of the absolute thickness measurements was used to verify the transformation of the relative height values of the CLSM into the absolute thickness of the oxide layers. The transformation of the relative height into absolute thickness data is described in the subsection 5.1.3.

The relative heights of many different grain orientations were measured by using the CLSM and all different grain orientations can be evaluated by the absolute thickness of the oxide layer using the combination of FIB-SEM and CLSM. For developing this measurement method, the oxidation experiments should be suitable for testing different parameters. The tested parameters are summarized in subsection 3.6. Therefore, all oxidation experiments were performed at 870 K for 30 min during the method development. Under these conditions eight oxidation experiments were performed and the increase of mass was measured with the thermobalance. A second independent gravimetric analysis system, an analytical balance, was used to measure the mass difference. The sample weight was determined before and after the oxidation. Oxidation rates were calculated based on weight differences.

5.1.1 Relative Heights of the Oxide Layer obtained with the CLSM

The measurement of relative heights was performed with a CLSM. It was possible to take a height profile image and evaluate the data with the software of the microscope for each grain separately. It was of interest to see if there is a grain dependency. The analysis is described in subsection 3.4.2. The merging of EBSD and CLSM data are described in section 4.2.

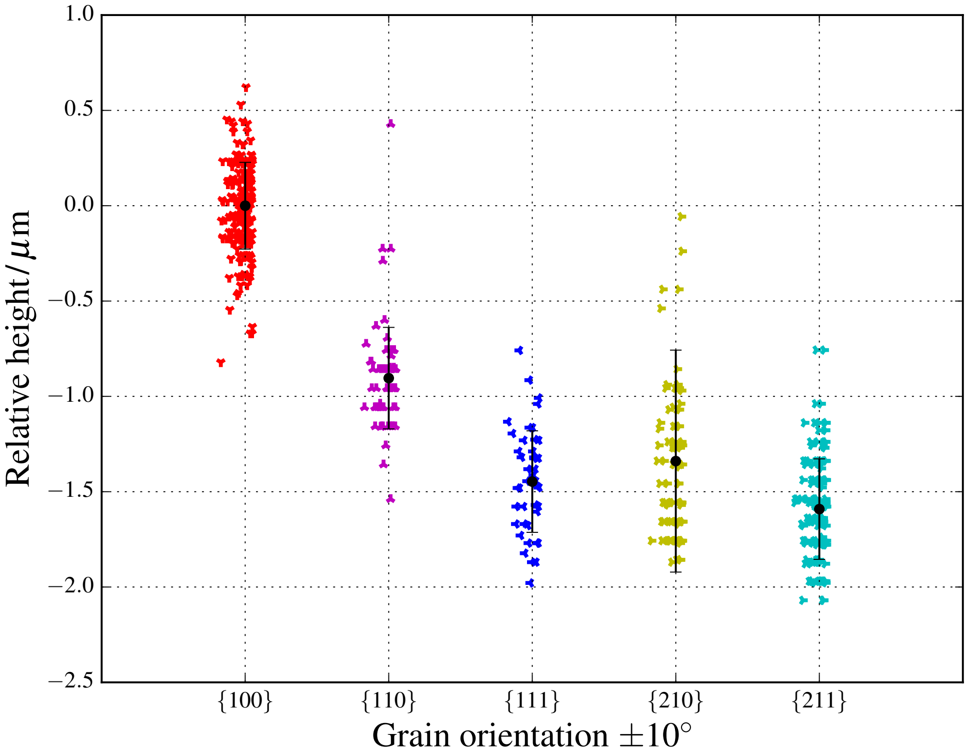

Figure 33: Grain dependent oxidation. On the y-axis, the relative thickness of the oxide layer leveled to the index (100) and on the x-axis, the grain orientation are shown. The values vary randomly on the x-axis to enhance the visibility. The values are measured using a CLSM.

The results from the CLSM measurement in figure 33 show that the {100} orientation has a higher oxidation rate than the orientation {110} and {111}. The orientation {110} has an oxidation rate between the orientation {100} and {111}. The {210} and {211} orientation show also low oxidation rates comparable to the {111} orientation.

The mean values of the relative height differences between the grain orientated oxidation are listed in table 8.

Table 8: Difference of the relative oxide layer height between the {100} and the other four orientations. 225 grains were measured for the {100} orientation, 72 grains for the {110} orientation, 46 grains for the {111} orientation, 94 grains for the {210} orientation and 147 grains for the {211} orientation.

Orientation	{100}	{110}	{111}	{210}	{211}
Relative height to the {100} orientation	0.00 µm	−0.90 µm	−1.45 µm	−1.34 µm	−1.59 µm

It is obvious that crystal orientation has as significant impact on the oxidation rate. In the next section this behavior will be investigated by measuring the absolute thickness of the oxide layer.

5.1.2 Absolute Thickness of the Oxide Layer obtained with FIB

The focused ion beam (FIB) was used to make cross-sections. Several cross-sections were performed on each sample to obtain an average value of the absolute height of each orientation. Cross-sections on a sample are shown in figure 34. The grains were selected for the cross-sections regarding their crystal orientations, known from the EBSD data. Figure 34(a) shows grains with a Pt-C layer. This layer allows to generate a sharp edge at the oxide layer for an exact thickness measurement.

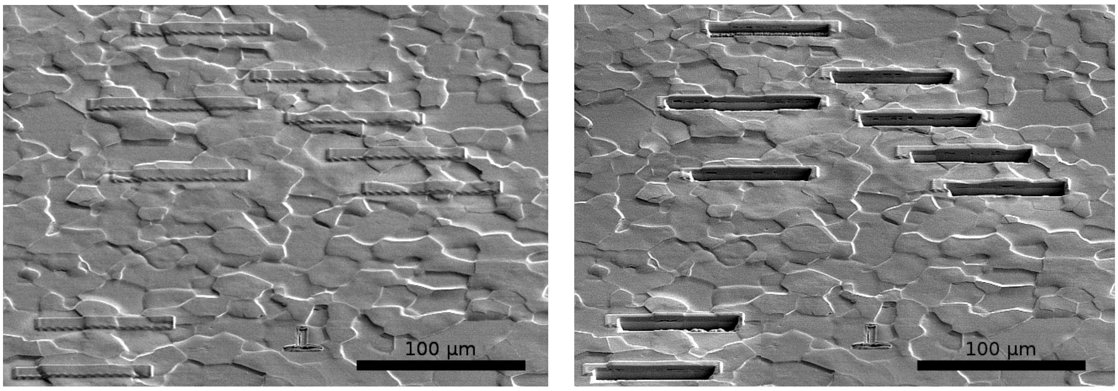

(a) A SEM image of an oxidized sample. The sample is viewed under an angle of 52°. Pt-C was coated on top of the oxide layer on selected grains. Pt-C allows to generate a sharp edge at the oxide layer.

(b) A SEM image of the same area as shown in (a). Several cross-sections were prepared by FIB.

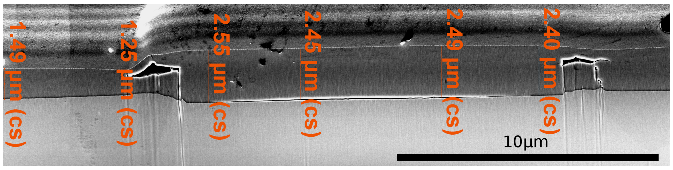

(c) A SEM image of a cross-section. The cross-section is viewed under an angle of 38°. Pt-C layer is coated on top, the oxide layer is in the middle and tungsten is on the bottom of the image. The length measurements were performed with the software of the SEM.

Figure 34: Three SEM images taken with a secondary electron detector. The pictures (a) and (b) show the cross-section preparation and picture (c) shows the thickness measurement of the oxide layer.

Cross-sections are shown in figure 34(b). These cross-sections were imaged at high magnification for evaluation of thickness measurements. In figure 34(c) an example of a measurement is shown. A few thickness measurements were taken on one grain and a mean value was calculated. The non-uniform oxide layer close to the grain boundaries was avoided for the thickness measurement.

The grain orientations are not homogeneously distributed. More grains with the

{100} orientation and {110} orientation are on the sample than with the {111} orientation. An orientation map from the sample is shown in figure 41 in chapter 5.2 and illustrates the orientation distribution. Manhard et al.[34] published an article about the microstructure of the samples from the same tungsten batch and described the distribution of the grain orientations.

Therefore, more measurements were performed on the {100} and {110} orientation as on the {111} orientation. For a comparison between the calculated thickness from the CLSM to absolute thickness data obtained on cross-sections using a FIB-SEM, the {210} and {211} orientation were also measured. The measurements are shown in figure 35.

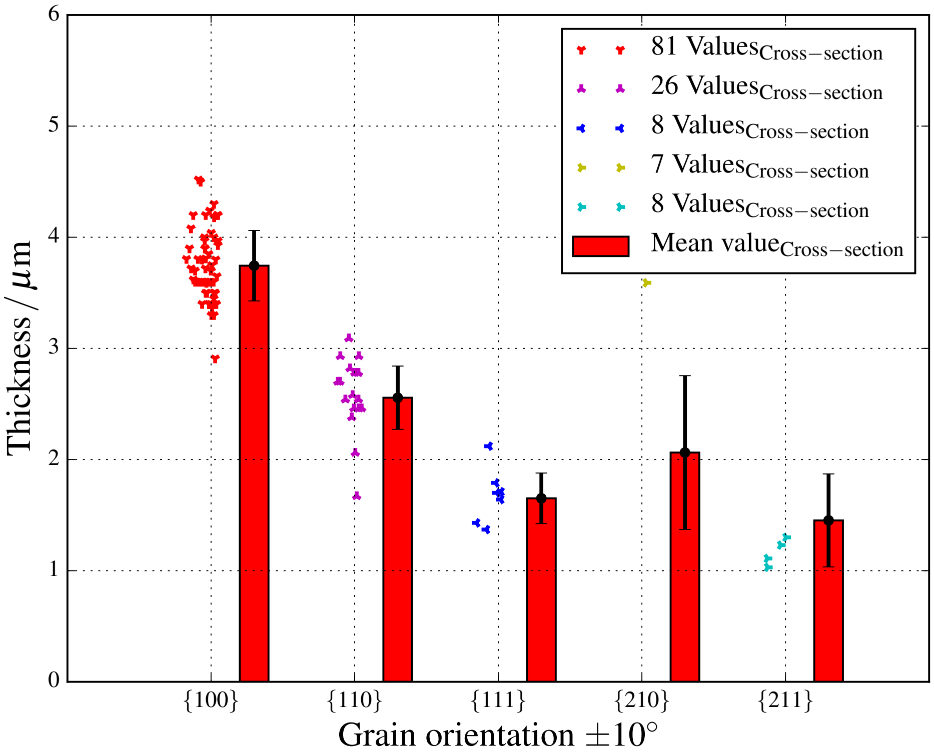

Figure 35: Grain dependent oxidation. The thickness of the oxide layer is plotted against the grain orientation. The values vary randomly on the x-axis to enhance the visibility. The values were measured using a SEM on FIB cross-sections.

The absolute thickness of the oxide layer varies by a factor of two between the {100} and the {111} and {211} orientation. This confirms the results using the CLSM, that the oxidation is the fastest at the {100} orientation.

5.1.3 Conversion of Relative Heights into Absolute Thickness Data

To generate absolute thickness data from the CLSM measurements, cross-sections by FIB and images using a SEM have to be performed.

At least eight absolute thickness measurements were performed on cross-sections of each sample. The grain orientation with the highest oxidation rate was chosen which was the {100} orientation.

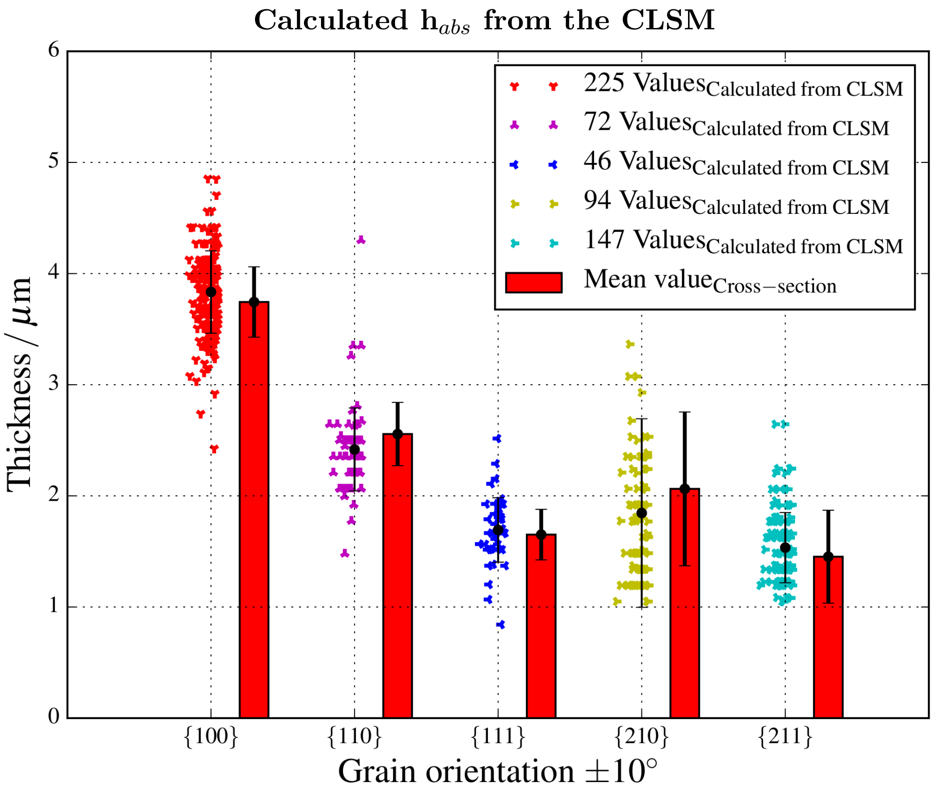

Figure 36: Grain dependent oxidation. The thickness of the oxide layer is plotted against the grain orientation. The values vary randomly on the x-axis to enhance the visibility.
The calculated values from the CLSM measurements are shown as points. The growth into the depth is calculated with the experimental correction factor of 0.45 which is described in chapter 5.1.3. The absolute thickness values on cross-sections are shown as bars to compare them with the calculated values from the CLSM. This figure includes data from samples of five independent incubations.

The tungsten oxide expands also below the original surface. This is illustrated in figure 32 and 37. This must be taken into account for converting relative values from the CLSM into absolute values. The growth of tungsten oxide below the original surface was verified by an experiment. The height and depth growth was measured at the grain boundaries.

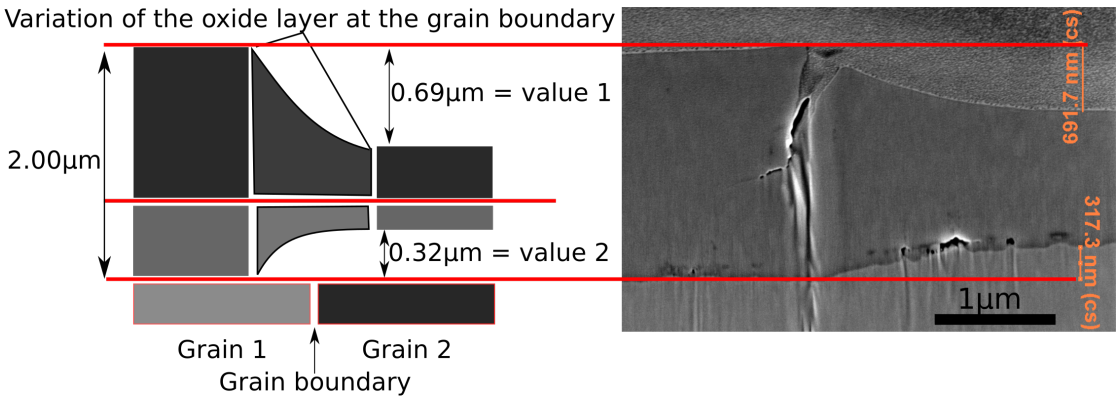

Figure 37: An illustration of the experimental measurement of the correction factor to convert the CLSM data to absolute thickness data. As an example, grain 1 is the {100} orientation with a high oxidation rate and grain 2 is the {111} orientation with a low oxidation rate.

A grain boundary between two grains with different oxidation rates is shown in figure 37. At these positions it is possible to measure height differences between the oxide layer. Two measurements were done. In figure 37 the value one and the value two were measured and the ratio was calculated.

Over 22 measurements were performed at grain boundaries and the mean ratio was 0.45 ± 0.13 between depth growth and height growth. The error of 0.13 is the standard deviation of the measurements.

It was expected that the mean ratio, derived from these measurements, is similar to the quotient of the number densities of tungsten and tungsten oxide (WO_3) which is 0.29. The experimental correction factor is higher than the ratio of the number densities and therefore the depth growth into the tungsten is higher than expected. The relative values with the correction of the ratio of number densities compared to the absolute thickness measurements on cross-sections are shown in the appendix in figure 59. The calculated mean values from the CLSM are in the error range of the absolute thickness measurements on cross-sections, but the calculated mean values are above the mean values of the absolute thickness measurements.

Compared to figure 36, in which the relative values from the CLSM are calculated with the experimental correction factor, the calculated values are sometimes above and sometimes below the values of the absolute thickness measurements derived by cross-sections.

Because of this comparison the values were calculated with the experimental correction factor.

As stated in equation 4.1, the absolute height was calculated using the following

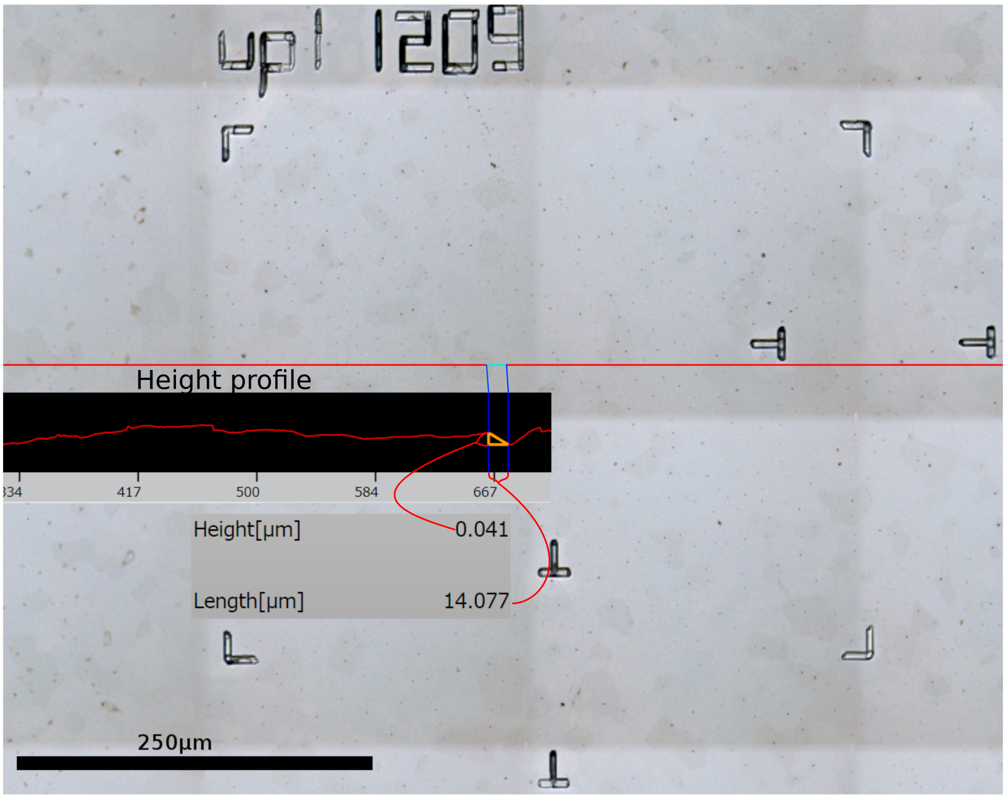

Figure 38: A picture from a CLSM with a 50x magnification objective. 16 pictures were stitched together. The sample was electropolished and height differences are seen of around 40 nm between neighboring grains.

equation.

$$h_{abs.\{110\}} = h_{abs.\{100\}} + h_{rel.\{110\}} + h_{rel.\{110\}} * 0.45 \tag{5.1}$$

$$h_{abs.\{111\}} = h_{abs.\{100\}} + h_{rel.\{111\}} + h_{rel.\{111\}} * 0.45 \tag{5.2}$$

where $h_{abs.\{100\}}$ is the absolute height on cross-sections, $h_{rel.\{110\}}$ is the relative value of the CLSM (this value is negative and illustrated in figure 32) and the last term is the correction for the depth growth.

A CLSM image of an electropolished sample is shown in figure 38. Steps around 40 nm are observed. These steps are big enough to get a deviation between the ratio of the number density and the experimental values. Also holes are observed in the oxide layer which influence this too.

To conclude, the conversion of relative values into absolute thickness values is the appropriate way to evaluate the grain dependent oxidation rates. The influence of grain dependency induces a factor of two in the thickness, and therefore in the oxidation rate between the {100} and the {111} orientation.

5.2 Comparison of Oxidation Rates

The linear oxidation rate K_l and the parabolic oxidation rate K_p are two limiting cases of oxidation kinetics. A weight increase over time is necessary to verify an oxidation kinetics. To evaluate an oxidation kinetics with a two point measurement, assumptions had to be made for the calculation.

- The linear oxidation rate was calculated under the assumption that the mass increase is linear from the beginning of the oxidation to the end.
- The parabolic oxidation rate was calculated under the assumption that the mass increase is parabolic from the beginning of the oxidation to the end according to $t \propto \sqrt{m}$.

The mean values of the oxidation rate from the analytical balance and the thermobalance are shown in table 9. All oxidation rates of the individual measurements of the samples are listed in the appendix in table 16.

Table 9: Mean values (MVs) of oxidation rates from gravimetric analysis measurements. The standard deviation (SD) was calculated from eight measurements. All data are shown in table 16 in the appendix.

Sample	Thermobalance fit		Thermobalance Δm_{O_2}		Analytical balance	
	K$_l/\frac{mg}{cm^2 * s}$	K$_p/\frac{mg^2}{cm^4 * s}$	K$_l/\frac{mg}{cm^2 * s}$	K$_p/\frac{mg^2}{cm^4 * s}$	K$_l/\frac{mg}{cm^2 * s}$	K$_p/\frac{mg^2}{cm^4 * s}$
MV	2.58E-04	2.56E-04	3.26E-04	1.94E-04	3.68E-04	2.45E-04
SD	3.28E-05	8.95E-05	4.30E-05	4.91E-05	2.83E-05	3.72E-05

The linear oxidation rates of the gravimetric measurements were calculated according to the following equation:

$$K_l = \frac{\Delta m_{0_2}}{A \cdot t}, \tag{5.3}$$

where K_l is the linear oxidation rate, Δm_{0_2} the mass difference, A the surface area which is 2.4 cm^2 and t is the oxidation time.

The parabolic oxidation rate of the gravimetric measurements was calculated according to the following equation:

$$K_p = \frac{(\Delta m_{0_2})^2}{A^2 \cdot t}, \tag{5.4}$$

where K_p is the parabolic oxidation rate.

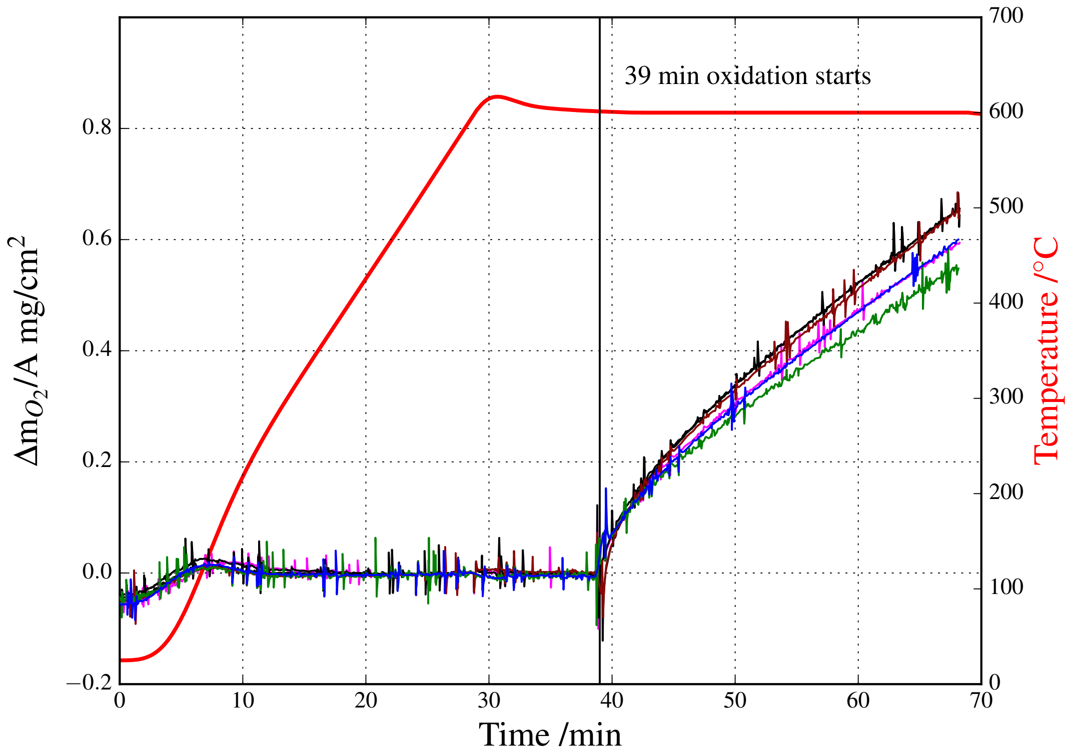

Figure 39: Oxidation at 870 K for 30 min. Data of five different oxidation tests are shown. At first, a pure argon atmosphere was in the thermobalance. After 39 min oxygen was switched on and a 20 % oxygen/80 % argon atmosphere was sustained in the thermobalance.

The mass difference was evaluated with the analytical balance by the measurement before and after the oxidation experiment. With the thermobalance the mass difference was evaluated by measurements before and after oxygen gas flow was triggered.

In contrast of measuring only the mass difference, the thermobalance records the mass change over time. The oxidation rate using the data of the thermobalance can be evaluated by a linear or a parabolic regression. The parabolic regression was fitted from the start point of the oxidation to the end point of the oxidation.

The linear regression was fitted from the second half of the oxidation time to the end. The reason is explained below.

If diffusion processes occur, a parabolic behavior of the oxidation rate will be expected. If cracks in the oxide layer influence the oxidation, the parabolic behavior will change to a linear behavior. Cracks only influence the oxidation when the oxide layer is thick enough. The limiting case of a linear oxidation rate is not at the beginning of the oxidation. This is the reason why the linear fit is only applied in the second half of the oxidation time.

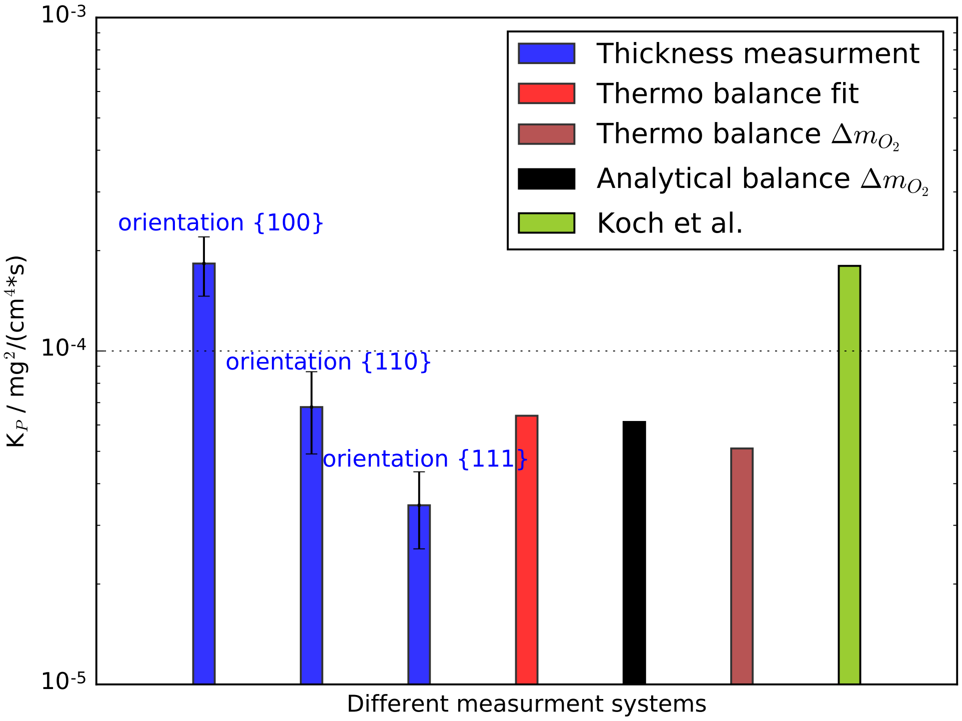

Figure 40: The parabolic oxidation rates obtained by different data evaluation methods. The data of the thermobalance, analytical balance and the thickness measurement are mean values of at least five independent oxidation experiments. The orientation {100} has the fastest oxidation and the orientation {111} the slowest. All other oxidation rates are between these two values. The oxidations were performed at 870 K for 30 min whereas Koch et al.[35] oxidized longer time (12 h) and at 873 K.

In figure 39 several measurements derived from the thermobalance are presented. There is a strong mass increase at the beginning of the oxidation. In the second part, a mix of linear to parabolic mass increase is observed.

Koch et al.[35] expected that tungsten oxidizes with linear oxidation behavior at a temperature of 870 K[35]. But Koch et al.[35] oxidized over 12 h at 873 K. The oxidation time in the standard incubation procedure was 30 min at 870 K in this thesis. Since cracks do not significantly influence the oxidation procedure used here, a parabolic oxidation rate is assumed. The oxidation results in figure 39 show a parabolic behavior as well. These are the reasons for focusing on parabolic oxidation rates in this thesis.

To compare the thickness measurement from the CLSM and SEM with the analytical balance, thermobalance, and the previous data from Koch et al.[35] for the same and for higher oxidation temperatures, the thickness measurements have to be converted into oxidation rates. According to equation

$$K_p = \frac{(l_{thickness} * \rho_{WO_3} * \frac{3*u_O}{u_W+3*u_O})^2}{t_{ox}}, \tag{5.5}$$

where K_p is the parabolic oxidation rate, $l_{thickness}$ is the thickness of the oxide layer, $\rho_{WO_3} = 7.25\,\frac{\mathrm{g}}{\mathrm{mL}}$[12] is the density of tungsten oxide, t_{ox} is the oxidation time and $\frac{3*u_O}{u_W+3*u_O}$ is the ratio of the atomic mass of oxygen and tungsten oxide. The reason for using the atomic ratio is that the thermobalance and analytical balance measured the mass increase by oxygen uptake and not the mass of tungsten oxide.

It is unknown which tungsten oxides are formed during the oxidation. Fortunately, the product of density and the atomic ratio is similar for all tungsten oxides as shown in table 10. This means the ratio of the different tungsten oxides does not effect the calculation of the oxidation rate. The density of WO_3 is used to convert the thickness measurement into a parabolic oxidation rate. The error estimation is done using the following equation.

$$K_{p_{error}} = \frac{\partial K_p}{\partial \rho_{WO_3}} * \Delta\rho_{WO_3} + \frac{\partial K_p}{\partial l_{thickness}} * \Delta l_{thickness} \tag{5.6}$$

The error of the density of tungsten oxide ($\Delta\rho_{WO_3}$) was estimated to be ± 0.3 $\frac{\mathrm{g}}{\mathrm{mL}}$ and $\Delta l_{thickness}$ is the standard derivation of the thickness measurement. The errors of this transformation are further discussed in section 6.2.

Table 10: Densities of different tungsten oxides[12]. This table shows that the different tungsten oxides do not effect the calculation of the thickness measurement to linear or parabolic oxidation rates. The values in the column "Density*$\frac{x*u_O}{u_w+x*u_O}$" vary less than 3 %.

	Density / $\frac{g}{mL}$	Atomic ratio ($\frac{x*u_O}{u_w+x*u_O}$)	Density*$\frac{x*u_O}{u_w+x*u_O}$/ $\frac{g}{mL}$
$WO_{x=3}$	7.25	0.26	1.89
$WO_{x=2.72}$	7.8	0.23	1.84
$WO_{x=2}$	10.9	0.17	1.89

In figure 40 the comparison of the parabolic oxidation rates is presented. The oxidation rates of the balances are a little below the {110} orientation oxidation rate of the thickness measurement. A reason could be that the grain orientations are not equally distributed on the sample.

The tungsten sample has two different textures on each side[34]. EBSD data from both sides are shown in figure 41. On the samples most of the grains have the {100} and {110} orientation. Just a small amount of grains has the {111} orientation.

The gravimetric methods give a mean value over all grain orientations. Because of the high amount of the {100} and {110} orientation the oxidation rates were expected to be between the specific oxidation rate of {100} and {110} orientation. But it was also observed that the {210} and {211} orientation have a low oxidation rate. It might be that the high indexed surfaces have a lower oxidation rate in average than the oxidation rate of the {110} orientation.

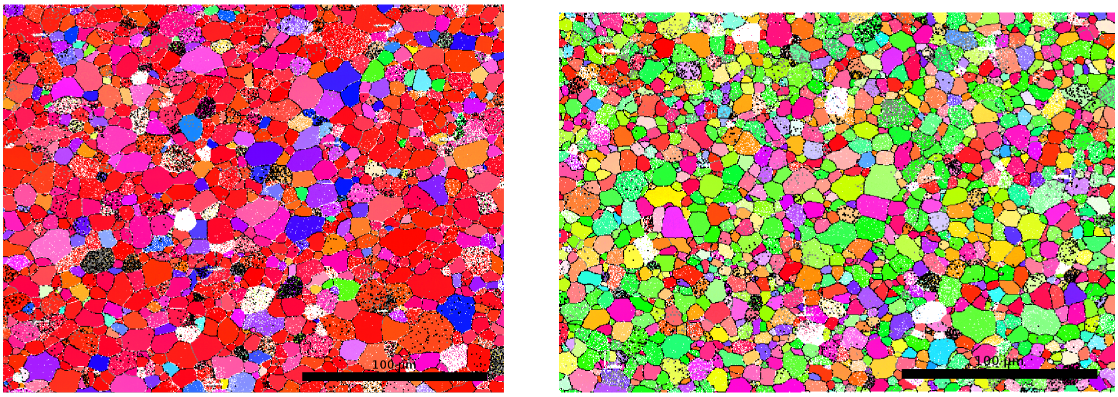

(a) The A-side of the tungsten sample. Most grains possess the {100} orientation[34].

(b) The B-side of the tungsten sample. Most grains possess the {110} orientation[34].

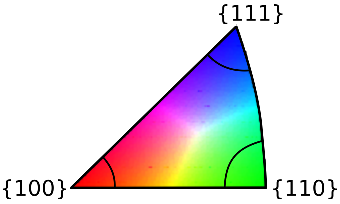

(c) The electron backscatter diffraction-color scale of the grain orientation. The cycles at the corners show a variation of 10° of the Euler angle.

Figure 41: Comparison of orientation maps. Most of the grains on the sample possess the {100} and {110} orientation. Only a small amount of grains are in the {111} orientation.

In general, the grain orientated oxidation rates from thickness measurement agree well with the oxidation rates of the gravimetric methods and the data from Koch et al.[35]. Furthermore, it is shown that the different tungsten oxides do not effect the conversion of the thickness measurements to oxidation rates.

5.3 Grain Dependent Oxidation at Different Temperatures

The developed method was applied to investigate grain dependent oxidation at different temperatures. To facilitate the comparison at different temperatures the same thickness of the oxide layer was aimed. Oxidation pretests were necessary to adjust the oxidation time. The temperature, oxidation time and the absolute thickness, verified by cross-sections, are shown in table 11.

Table 11: Oxidation time to produce an oxide layer of around 3 µm to 4 µm in the crystal orientation {100}. The oxidation time was too short at a temperature of 770 K.

temperature / K	time/h	thickness/ µm
870	0.5	3.8
820	2.5	3.6
770	6.5	1.5
720	96	3.9

The oxidation at 770 K had a too short oxidation time and therefore a too thin oxide layer. The other oxidations fitted very well into the expected thickness of the oxide layer. Five independent oxidations were performed at a temperature of 870 K because the method development was performed at this temperature. At the other oxidation temperatures one sample was oxidized to study all 3 lowest indexed grain orientations. The temperature dependence is shown in figure 42. The absolute thickness of the oxide layer is plotted against the grain orientation. The evaluation is described in subsection 5.1.3. The grain specific evaluation shows the same grain dependency at all temperatures, except for the oxidation with the too thin oxide layer at 770 K.

The thickness of the oxide layer oxidized at 770 K is in the {110} orientation the same as in the {111} orientation and only 30 % lower than for the {100} orientation. Oxidation experiments, at lower or higher temperatures than 770 K, showed that the {110} orientation has a thicker oxide layer than the {111} orientation. Maybe the effect of the grain orientated oxidation is low on a thin oxide layer and more pronounced on a thick oxide layer.

The final results demonstrate that the oxide layers will have the same, crystal orientated thickness differences at all tested temperatures, if the oxide layers have approximately the same thickness. The thickness measurements were converted into parabolic oxidation rates with equation 5.5 to compare the data with the data obtained from gravimetric measurements and the data of Koch et al.[35].

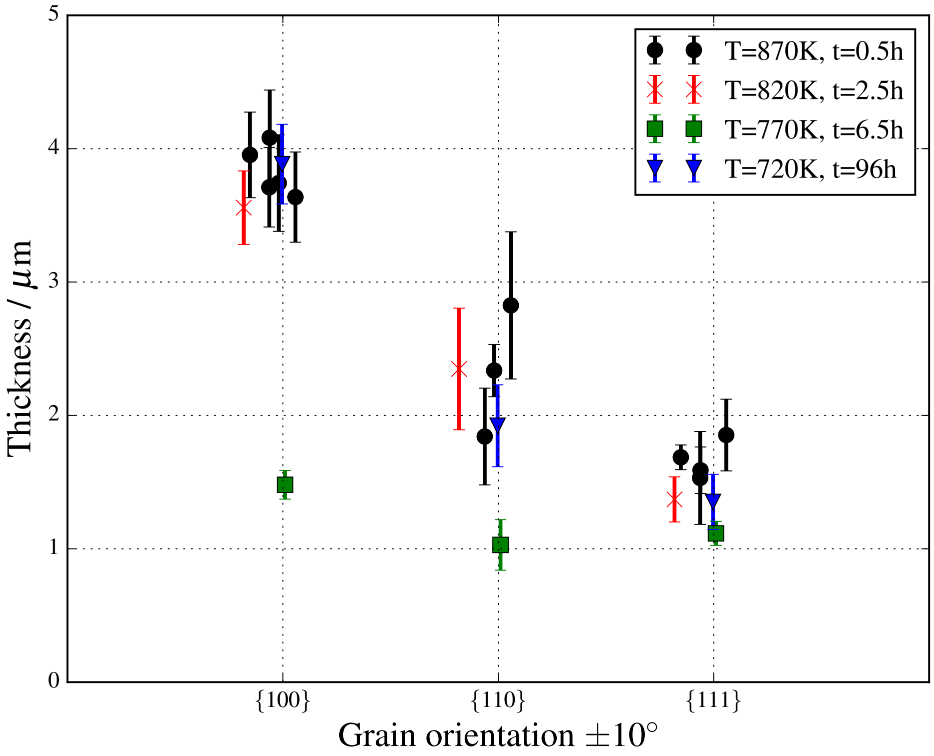

Figure 42: Grain dependent oxidation at four different temperatures. The absolute thickness of the oxide layer is plotted against the grain orientation. The values vary randomly on the x-axis to enhance the visibility. The oxidation time at 770 K was too short and therefore the oxidation layer was too thin for a comparison.

The comparison is shown in figure 43. It is an Arrhenius plot which describes the dependence of a chemical reaction on the inverse absolute temperature.

Koch et al.[35] oxidized from 873 K to 1273 K. The oxidations in this master thesis were performed for 30 min at 870 K whereas Koch et al.[35] oxidized for 12 h. During a longer oxidation the oxide layer is influenced by cracks and a linear oxidation rate would be expected. Koch et al.[35] only evaluate the oxidation rate parabolically, to compare it with self-passivating tungsten alloys which have a parabolic oxidation rate. Therefore, the oxidation rates of pure tungsten from Koch et al.[35] can be slightly too high.

The comparison of the data from Koch et al.[35] fit very well and allow an extension of the Arrhenius plot. The mean parabolic oxidation rates from the gravimetric analysis systems are shown in table 12.

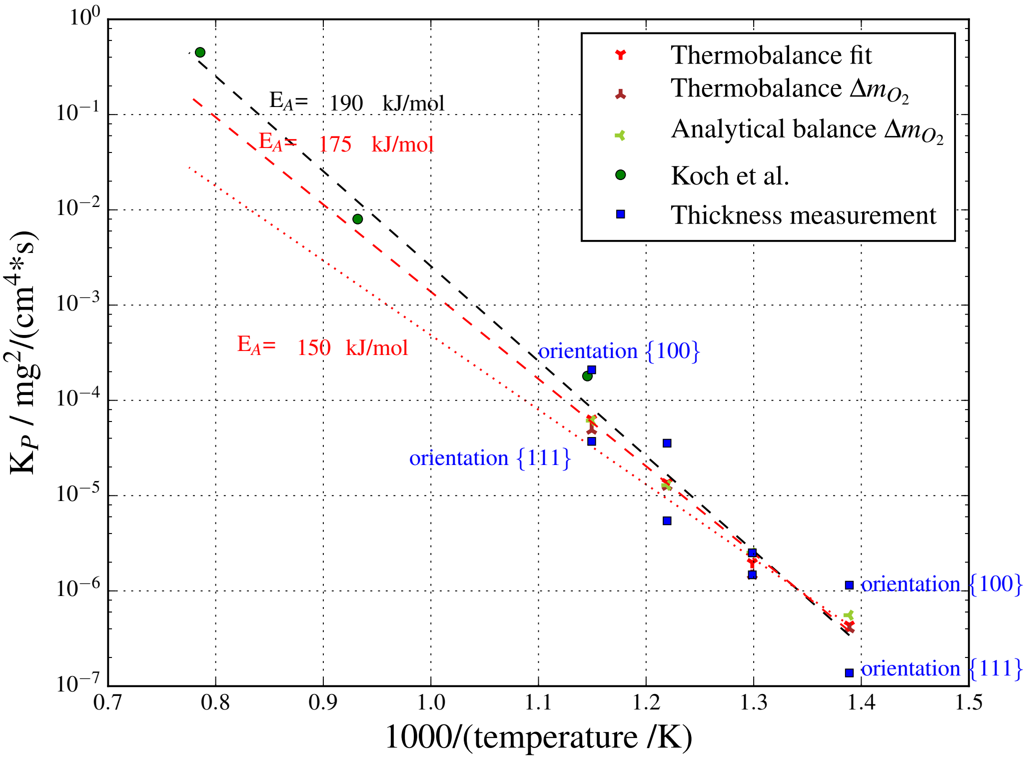

Figure 43: The parabolic oxidation rate is plotted against the inverse of the temperature. This figure compares data of different measurement systems with the data from Koch et al.[35]. The mass increase is only due to oxygen uptake.
The "thermobalance fit" data are used for the red regression lines. The red dotted regression line is fitted with equation 5.7 and the standard deviation of the measurements are taken into account for the regression. The red dashed line is a linear regression and the same relative errors are taken into account. The black dashed line shows a linear regression including the data of Koch et al.[35] with same relative errors for each data point.

The oxidation rates at different temperatures fit well into the regressions of the Arrhenius model. Three regressions are done to evaluate activation energies. The "thermobalance fit" data are used for the red regression lines.

The red dashed line is a linear regression and the same relative errors are taken into account. The black dashed line shows also the linear regression including the data of Koch et al.[35] with same relative errors for each data point.

The red dotted regression line is fitted with the Arrhenius function and the standard deviation of the measurements are taken into account for the regression. The

Table 12: Mean value of the oxidation rates at different temperatures. The oxidation rates for the temperatures at 1273 K, 1073 K and 873 K are from Koch et al.[35].

temperature / K	time/h	$K_p / \frac{mg^2}{cm^4 * s}$
720	96	4.3×10^{-7}
770	6.5	1.9×10^{-6}
820	2.5	1.3×10^{-5}
870	0.5	6.3×10^{-5}
873	12	1.8×10^{-4}
1073	12	8.0×10^{-3}
1273	12	4.5×10^{-1}

Arrhenius function is shown below:

$$C_1 \cdot e^{\frac{E_A}{R \cdot T}}, \tag{5.7}$$

where R is the gas constant, T is the temperature and E_A is the activation energy. All regressions are shown in figure 43 and the activation energy is between 150 $\frac{\text{kJ}}{\text{moL}}$ and 190 $\frac{\text{kJ}}{\text{moL}}$.

6 Discussion and Experimental Uncertainties

The chapter is subdivided into five sections.

The first section 6.1 discusses the errors of the measurement. This includes EBSD analysis, relative height measurements with the CLSM and the thickness measurements by the SEM device HELIOS.

Uncertainties in transforming thickness data and effects which can influence the oxidation are discussed in section 6.2. This includes the comparison of the thickness measurements with the data obtained by gravimetric analysis systems.

In section 6.3 the appearance of squared holes in the oxide layer is discussed. The reason for these holes is unknown. An investigation of this effect on single crystal surfaces would be of great interest.

Section 6.4 discusses the dependency of oxidation on the crystal orientation. In this respect, possible reasons like roughness of the surface, absorption of oxygen, diffusion of tungsten, diffusion of oxygen and effects on an atomic scale are discussed.

The last section 6.5 discusses the grain orientated oxidation at four different temperatures. This behavior is not temperature dependent and the activation energy is similar for all low indexed crystal orientations.

6.1 Error of Measurements

The EBSD measurements have an impact on all evaluations. The low indexed grain orientations were evaluated with a variation of 10° of the Euler angle. The standard deviation of the thickness measurement was around 300 nm (subsection 5.1.3). The thickness of the oxide layer varies on one grain up to 300 nm (subsection 3.5.2). A smaller variation of 5° of the Euler angle at the low indexed surfaces did not change the results of the oxidation rates and the standard deviations did not decrease significantly. A semi-automated analyses software would be necessary to study these effects in more details. Then it would be possible to evaluate more data, to evaluate the grain depend oxidation with a smaller variation of the Euler angle, and to evaluate the high indexed surfaces too.

Accurate results are obtained using the thickness measurement on cross-sections with the SEM because the absolute thickness is a direct measurement. The error of this measurement is around 10 nm. This is negligible in relation to the variation of the oxide layer on one grain up to 300 nm. But these measurements are time-consuming and it is not possible to get many data points with this method.

Therefore, the measurements are performed with the CLSM in combination with the SEM, and the relative values from the CLSM are transformed into thickness values of the oxide layer. There are several steps and for each step the corresponding error could influence the results.

To verify these measurements, a comparison was done with cross-sections in different grain orientations. This shows that the variation of the data is smaller than 10 % (subsection 5.1.3.

The total error over all measurements is small and therefore the method is suitable to get accurate and precise results. The comparison with two gravimetric methods confirms the determination of oxidation rates by thickness measurements.

6.2 Comparison of Thickness Measurements with the Data of Gravimetric Analysis Systems

The EBSD data showed a large amount of grains with the {100} and {110} orientation on the samples. Only a few grains have the orientation {111}. Therefore, it was expected that the data points of the oxidation rate from the gravimetric analysis systems are between the {100} and {110} orientation. But it was also observed that the {210} and {211} orientation have a low oxidation rate. It might be that the high indexed surfaces have in average a lower oxidation rate than the {110} orientation. The oxidation rates of the gravimetric analysis systems were close to the oxidation rate of the {110} orientation. This is shown in figure 40.

Several factors, like spalling of the oxide layer, handling of the sample or evaporation of tungsten oxide, can influence the gravimetric measurements. Spalling of the layer during the oxidation decreases the mass gain at gravimetric analysis. But no pieces were found in the thermobalance. Grain boundaries are a reason for spalling tungsten oxide from the layer during the oxidation. The oxidation rates are different at these locations and therefore stress and strain occur.

Also the handling of the sample can lead to a weight loss. To avoid this, plastic tweezers were used.

The evaporation of tungsten oxide was checked under argon atmosphere. There was no hint of an evaporation of the tungsten oxide which would lead to a smaller oxidation rate. This is shown in chapter 3.5.3.

It is possible that the oxide layer has a different thickness in the middle than on the edges of the sample. The thickness measurements were always performed in the middle of the sample and no thickness measurements were performed at the edge of the sample. It is unknown if the sample oxidizes differently at the edges. It is known that sometimes the oxidation has strange effects at the edges of the sample. Freimut Koch from the Max Planck Institut for Plasma Physics (IPP) oxidized a W-10 %Cr-2 %Ti alloy at 1273 K and oxidized structures were seen at the edges of the sample. A picture of that sample is shown in figure 44. Thickness measurements, performed in the middle of the sample, may not represent the measurement of the whole sample.

Figure 44: An oxidized W-10 %Cr-2 %Ti alloy at 1273 K. Oxidized structures appeared at the edges of the sample.

The density of tungsten oxide in the oxide layer is an additional uncertainty. Because there are holes in the oxide layer, the density is lower than for pure tungsten oxide. This means according to equation 5.5 that the oxidation rates are too high.

The calibration of the SEM device HELIOS for the distance measurements was also checked by a reference sample. The result was that the SEM measurements were accurate and precise.

The oxidation rates of gravimetric analyses are in accordance with the transformed thickness measurements. For revision, the effect of the oxidation rates by grain dependencies is far bigger than the variation of different analysis systems.

Both measurement techniques have their specific advantages and disadvantages. The thickness measurements are more precise for slow oxidations than the measurements with gravimetric methods because of the small increase of weight per time. The thermobalance measurement has generally a drift of 2 µg/h. The measurement of the oxidation takes several days for a slow oxidation, and the environment can influence gravimetric analysis systems. The gravimetric methods are better for faster oxidations because of the fast mass increase. In this case, the influence of the environment is small. Furthermore, the measurement is faster than doing time consuming cross-sections at the SEM.

6.3 Holes in the Oxide Layer

Square holes were observed in the oxide layer. Actually, this is something which is difficult to explain, because the holes did not look like cracks caused by stress and strain.

A cross-section with several holes is shown in figure 45.

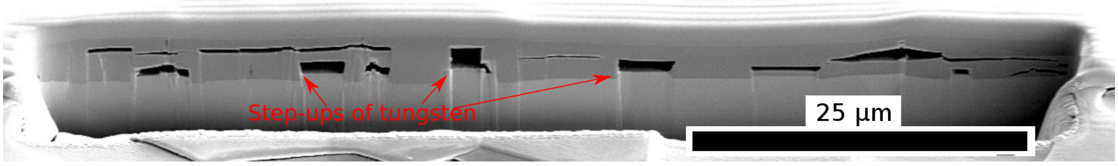

Figure 45: Cross-section of a recrystallized, oxidized tungsten sample. Many holes with rectangular side walls in the oxide layer are seen. The reason for this is unknown.

Most of the holes had rectangular side walls. It seems that the oxidation had stopped. Sometimes these holes were directly on the tungsten surface and sometimes in the middle of the oxide layer. It seems that the oxidation started again and formed a tungsten oxide layer under the hole. Before the oxidation, tungsten surface was flat and it looked like under a hole tungsten did not transform to tungsten oxide. The cross-section in figure 45 shows step-ups on tungsten surface under a hole.

It is impossible to see the holes without performing a cross-section. There is no sign of the holes on the surface of the oxide layer.

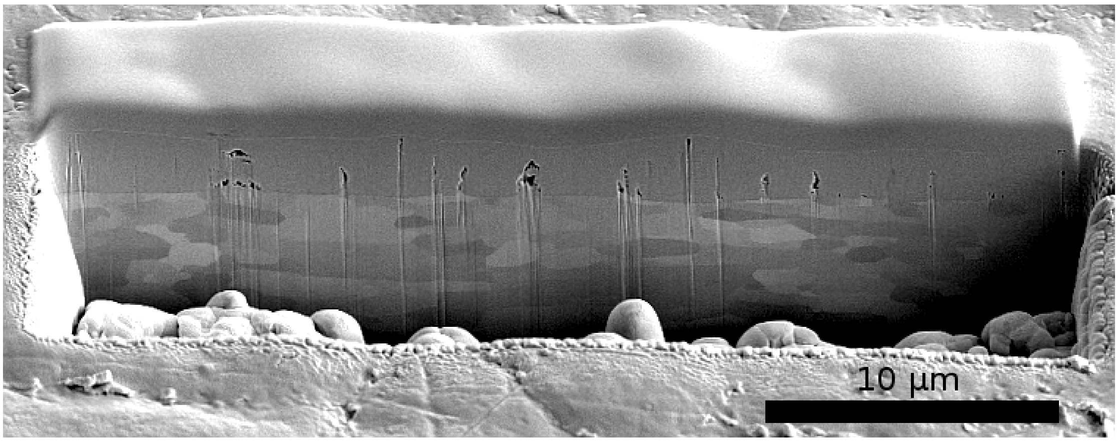

Figure 46: Cross-section of a non-recrystallized, oxidized tungsten sample. There are just a few holes in the oxide layer.

A non-recrystallized and oxidized sample with smaller grains did not have holes with rectangular side walls. Holes were observed but they were smaller. A cross-section of this sample is shown in figure 46. The oxidation was performed at 870 K for 30 min as for the recrystallized sample.

Cifuentes et al.[36] and Gulbransen and Andrew[37] tried to explain small holes and called them cavities. They were thinking about an oxidation mechanism where little cracks are formed at the oxidation front on which the oxidation takes place. They discussed cavities as shown in the appendix in figure 55, but I do not think that this mechanism can describe the holes in figure 45. It is also of interest that these big, rectangle holes are only in the recrystallized samples.

Finally, the holes influence the measurement to higher oxidation rates, because the volume and therefore the height of the oxide layer is larger. This error is around 5 %. The error was evaluated on many cross-sections by estimating the area of the holes and the area of the oxide layer.

6.4 Dependence of Oxidation on the Grain Orientation

Oxidation is a complex process. The oxidation of tungsten depends on several things like roughness of the surface, the absorption of oxygen, the diffusion of tungsten, the diffusion of oxygen and effects on an atomic scale.

The roughness has an influence at the very beginning of the oxidation. In this thesis samples were polished with different techniques and no significant difference in the oxidation rate was seen. The samples were very flat in all sample preparations and the roughness was in the order of some nm (around 40 nm as shown in figure 38).

The tungsten oxide expands around 70% above and 30% below the original surface level. A tungsten surface with a roughness of some nm is influencing the oxidation only for a short time until the scratches are oxidized. An oxide layer with a thickness around 4 µm was in focus. This means that the tungsten oxide is around 1 µm below the original tungsten surface. Of course, if the sample has a very rough surface, then the influence will rise.

At the starting point of the oxidation, oxygen is absorbed at the tungsten surface. Engel and Gomer[38] measured the absorption of inert gases into tungsten with different orientations. The {110} orientation has the highest absorption. At grain depending oxidations on tungsten the {100} orientation has the highest oxidation rate. This means that there is no correlation to the experiments of this thesis, and other factors dominate the oxidation.

It is known that WO_3 is permeable to oxygen[12]. If the first layer of tungsten oxide is produced, the absorption and diffusion of oxygen in tungsten oxide should

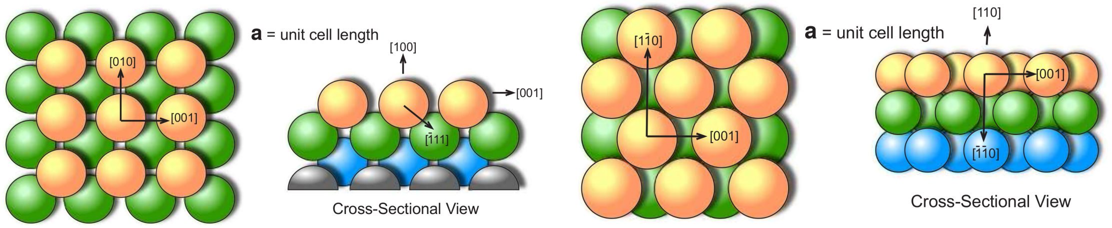

(a) A (100) crystal lattice. The distance between atoms in the [100], [010] or [001] direction is one unit cell length.

(b) A (110) crystal lattice. This is the closest surface in the first atomic layer.

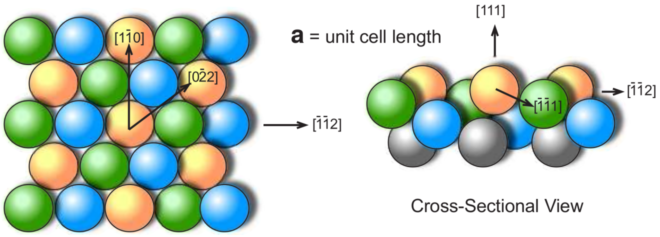

(c) A (111) crystal lattice. This is the most open surface in the first atomic layer.

Figure 47: Comparison of the lattice between different crystal orientations[39].

be the same in all crystal orientations because tungsten oxide is amorph. This was tested through EBSD and there was not any Kikuchi line visible on tungsten oxide.
To investigate the tungsten oxide layer, a μ-Rutherford Backscattering Spectrometry (RBS) would be a suitable method. The result of this investigation would be an areal density ($\frac{atoms}{m^2}$) of the oxide layer. The number density can be calculated with the thickness of the oxide layer. If the number densities have different values depending on the grain orientation, this will be a first hint for a different diffusion or absorption rate in tungsten oxide.

Another parameter to explain the order of the oxidation rate could be the atomic surface density of the low indexed surfaces.

Different low indexed surfaces of bcc-lattices are shown in figure 47. The (110) crystal orientation has the highest atomic surface density (atoms per area) in the first atomic layer. This does not correspond to the grain dependent oxidation of tungsten, because the {110} orientation has an oxidation rate between the {100} and {111} orientation.

In 1961 Ligenza[40] oxidized silicon with different crystal orientations. Ligenza[40] suggested that the crystal orientation effect depended on the surface density of atoms in the first atomic layer. He argued that the number of bonds are important and the Si-Si bonds had to be broken to proceed the oxidation. This is also the case in the bcc-lattice but do not fit to the tungsten oxidation. The tungsten {110} orientation has the highest surface density of atoms in the first atom layer but has an oxidation rate between the {111} and {100} orientation.

There are many effects which influence the oxidation and maybe it is a combination of some of them that leads to the final result. It is not possible to investigate a specific oxidation mechanism with the developed method. The master thesis had the focus to measure grain dependent oxidation.

6.5 Grain Orientated Oxidation at Four Different Temperatures

Oxidation is a highly temperature dependent process. Therefore, different oxidation times were used to achieve the same thickness of the oxide layer. The oxidation with the temperature of 870 K, 820 K and 720 K showed that the difference in the thickness of the oxide layer was around a factor of 2 between the {100} orientation and the {111} orientation.

Actually, the mechanisms for grain orientated oxidation is not understood. The results indicate that the grain dependent oxidation mechanism on the low indexed surfaces is not triggered by the temperature. An experiment with different oxidation times would help to get a better understanding for grain orientated oxidation. The oxidation at 770 K had a thin oxide layer and showed another grain orientated oxidation behavior. But more data are required for a conclusion.

The grain dependent oxidation was not influenced by the temperature. The activation energy is similar on all low indexed surfaces, because the slopes in the Arrhenius plot are similar. The activation energy obtained by the thermobalance is between 150 kJ/mol and 190 kJ/mol. The Arrhenius plot is shown in figure 43.

7 Summary

A method was developed to measure heights of oxide layers for individual low indexed surfaces. On the basis of image overlays the data from two different measurement systems were merged together. The height data were obtained by a confocal laser scanning microscope (CLSM), and the grain orientation data were obtained by the electron backscatter diffraction (EBSD) measurements. The evaluation showed that the {100} orientation had a thicker oxide layer than the {111} orientation.

The results were verified on cross-sections using the focused ion beam (FIB) of a scanning electron microscope (SEM). The absolute thickness of the oxide layer varies by a factor of two between the {100} and {111} orientation. The {110} orientation has an oxidation rate between the {100} and {111} orientation. The results are confirmed by the CLSM.

Based on the results on cross-sections the relative height data from CLSM were transformed into absolute thickness data of the oxide layer. The growth behavior of the oxide layer has to be taken into account by transforming the data. On a tungsten surface the tungsten oxide expands around 70 % above and 30 % below the original surface level. The data of the CLSM were transformed according to equation 5.1.

The measured thickness data were compared with results obtained by gravimetric analyses. The mass gain due to oxidation, measured by thermobalance and analytical balance, were transformed into parabolic oxidation rates in $\frac{\mathrm{mg}^2}{\mathrm{cm}^4 \cdot \mathrm{s}}$. According to equation 5.5 thickness data from the CLSM and the FIB of a SEM were transformed into parabolic oxidation rates.

A comparison of all three measurement systems was performed at four different temperatures and the results were consistent. Different regressions were made through the oxidation rate data of the thermobalance and the activation energy was calculated to be between 150 kJ/mol and 190 kJ/mol.

Koch et al.[35] performed oxidation experiments on tungsten at the same and higher temperatures. The data fit well to the data in this master thesis. This is shown in the Arrhenius plot in figure 43.

Depending on the grain orientation, the oxidation can be reduced by a factor of two. This reduction of the oxidation rate is not relevant for a technical application. The self-passivating alloys reduce the oxidation rate by three orders of magnitude. Further investigations are needed to evaluate if self-passivating alloys exhibit this effect.

8 Outlook

The developed method was used to evaluate grain dependent oxidation. The evaluation focused on the low indexed surfaces. A semi-automated data merging would enhance the evaluation and therefore, much more grains could be evaluated. This allows more precise results and the high indexed surfaces can be evaluated. In addition, the evaluation will be faster and more oxidation experiments can be performed. Influence of other parameters, like time or partial pressure of O_2, can be investigated in grain dependent oxidation experiments. To verify these effects, the results can be compared with the results obtained by single crystals.

After an optimized work flow is established, other materials like iron could be investigated on grain dependent oxidation. More data are needed for a better interpretation of theses effects. The developed method could be applied on other properties like sputtering or evaporation.

At last, the process of data merging can be extended to all procedural image-based measurement systems. The method allows to evaluate large data sets.

A Appendix

A.1 Self-Passivating Tungsten Alloys

A.1.1 Introduction

During my master thesis I got the opportunity to support an international project about ”Self-Passivating Tungsten Alloys”. The assignment of the Max Planck Institut for Plasma Physics (IPP) was to characterize the oxidation behavior. Therefore, the weight increase was measured using two different gravimetric analysis systems. A scanning electron microscope (SEM) was used for images from the surface and on FIB prepared cross-sections and EDX analyses.

The appendix gives an overview of the additional work during my master thesis. The abstract summarizes the project and was written by Aida Calvo from Ceit-IK4 Technology Center (CEIT).

A.1.2 Abstract

The abstract was written by Aida Calvo from CEIT:

”Tungsten is presently the main candidate material for the first wall armour of future fusion reactors. However, if a loss of coolant accident with simultaneous air ingress into the vacuum vessel occurs, the temperature of the in-vessel components would exceed 1000 °C, leading to the undesirable formation of volatile and radioactive tungsten oxides. A way to prevent this serious safety issue is the addition of oxide-forming alloying elements to pure tungsten which, in presence of oxygen at high temperatures, promote the development of a self-passivating oxide layer and protects tungsten against further oxidation. In this work, bulk tungsten alloys of the W-Cr-Y system with different concentrations of the alloying elements are studied in order to establish their optimum composition for lowest possible oxidation rate and the best self-passivating behaviour together with acceptable thermal and mechanical properties. The materials are manufactured by mechanical alloying and subsequent densification by hot isostatic pressing. Microstructural investigations of the bulk material and the thin oxide layer developed after oxidation as well as the thermal conductivity and mechanical properties of the alloys at different temperatures are presented. The W-Cr-Y alloys exhibit an ultrafine grained microstructure with an average grain size around 100 nm. A summary of the results of different tests under conditions relevant to the expected operation as first wall material is shown: oxidation tests under isothermal and accident-like conditions; high heat flux tests at GLADIS (Garching Large Divertor Sample Test Facility) up to $2\,\frac{MW}{m^2}$, according to the power load expected at the blanket first wall; and thermal-shock tests at JUDITH (Juelich Divertor Test Facility Hot Cells) to simulate e.g. loads by photon flashes occurring at the first wall of a DEMO. Compared to previous alloys of the system W-Cr-Ti, the W-Cr-Y alloys exhibit significantly lower oxidation rates both under isothermal and accident-like conditions."

A.1.3 Samples prior to Oxidation

CEIT delivered tungsten (W) alloys with 10 wt% chromium (Cr) and 0.5 wt% yttrium (Y) called W-10Cr-0.5Y HIP. W-10Cr-0.5Y HIP alloys had two different production procedures. Both were manufactured by mechanical alloying and subsequent densification by hot isostatic pressing (HIP). Afterwards, one alloy got an additional temperatur treatment (TT) at 1550 °C. This alloy is called W-10Cr-0.5Y HIP + TT. CEIT delivered five of the W-10Cr-0.5Y HIP samples and one W-10Cr-0.5Y HIP + TT sample. Both manufactured samples were investigated by a SEM and cross-sections were performed by a FIB prior to oxidation. The cross-sections are shown in figure 48.

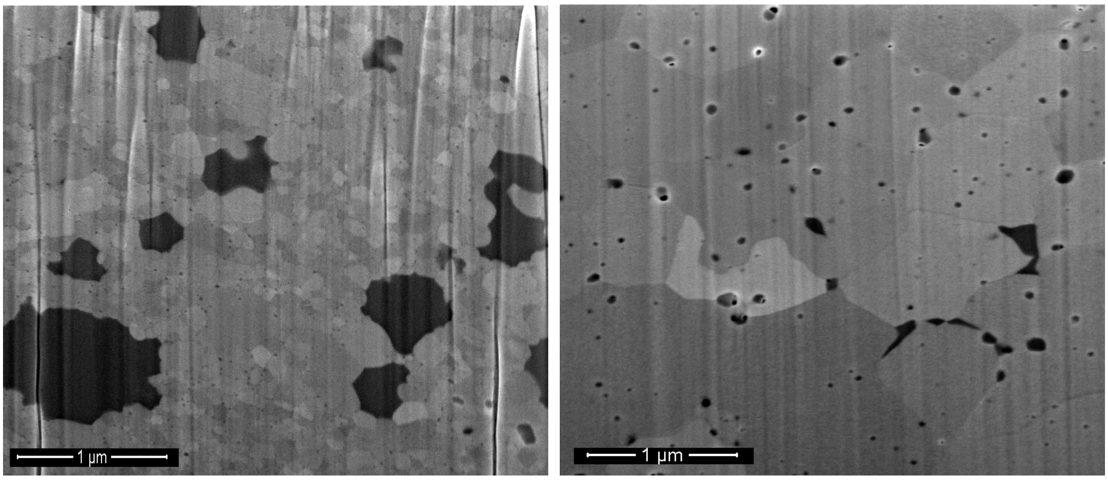

(a) A SEM-image showing a cross-section of a W-10Cr-0.5Y HIP alloy. The black areas in the image have a higher concentration of Cr.

(b) A SEM-image showing a cross-section of a W-10Cr-0.5Y HIP + TT alloy. The black areas in the image have a higher concentration of Cr as confirmed by EDX.

Figure 48: Comparison between the W-10Cr-0.5Y HIP alloy and the W-10Cr-0.5Y HIP + TT alloy.

The distribution of Cr in the W-10Cr-0.5Y HIP + TT alloy is more homogeneous than in the W-10Cr-0.5Y HIP alloy as EDX-analyses on cross-sections confirmed.

A.2 Oxidation Results of Self-Passivating Tungsten Alloys

Isothermal Oxidations at 800 °C

Isothermal oxidation tests were performed at 800 °C for up to 60 h. The results are shown in figure 49.

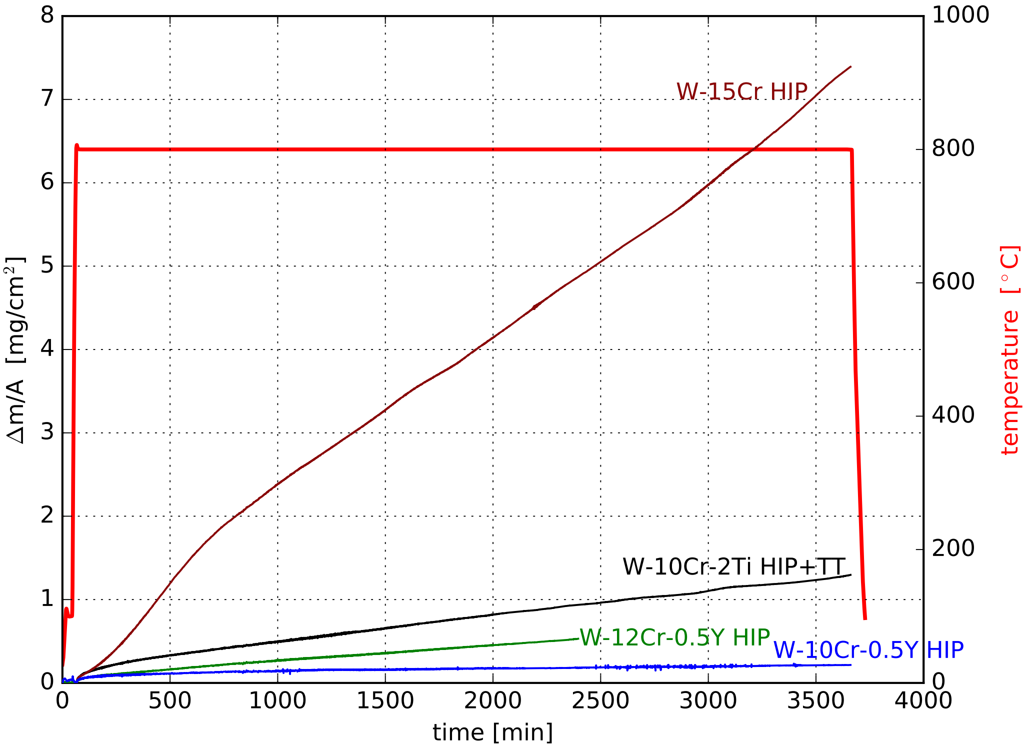

Figure 49: Oxidation at 800 °C for 60 h. Data of four different self-passivating tungsten alloys are shown. A 20 % oxygen/80 % argon atmosphere was applied during the oxidation in the thermobalance. The alloys W-12Cr-0.5Y HIP, W-10Cr-2Ti HIP and W-15Cr HIP were obtained from previous work of this project [14] [15].

The oxidation rate of W-10Cr-0.5Y HIP alloy is very low and shown in table 13. The two different kinetics, which were calculated in table 13, are described in section 5.1. A mix of linear to parabolic mass increase was observed for the W-10Cr-0.5Y HIP alloy during the oxidation experiments shown in figure 49.

The oxide layer of the W-10Cr-0.5Y HIP alloy is shown in figure 50. Big ”volcanoes” are observed on the oxide layer. The mechanisms for the formation of the volcanoes are unknown. Images of the oxide layer are shown in figure 50(b) at

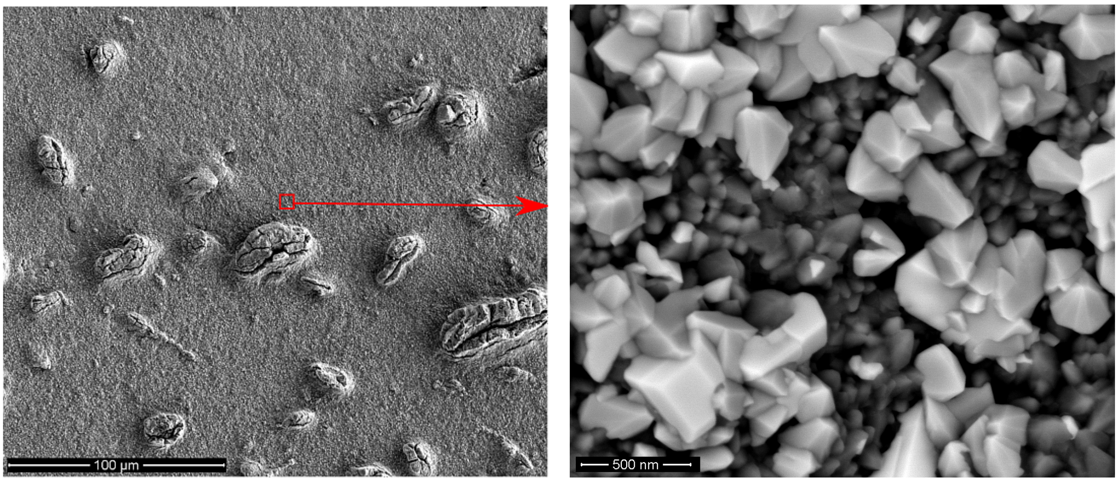

(a) A SEM-image of the oxide layer is shown. ”Vulcanos” are seen on the oxide layer.

(b) A SEM-image of the oxide layer is shown. Different oxides (chromium oxide, tungsten oxide and yttrium oxide) are observed at the surface.

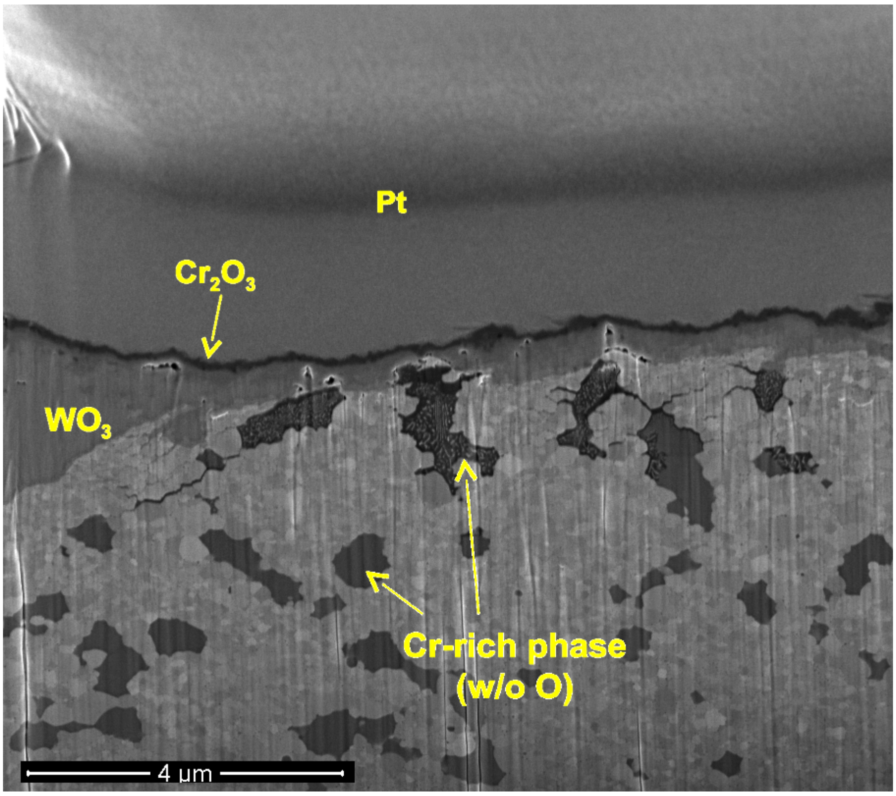

(c) A SEM-image on a cross-section is shown after oxidation. Pt-C layer is coated on top to cover the oxide layer. Under the Pt-C layer, a chromium oxide layer acts as an protective layer and a tungsten oxide layer is located under the chromium oxide layer.

Figure 50: Images of an oxidized W-10Cr-0.5Y HIP alloy at 800 °C.

Table 13: Isothermal oxidation at 800 °C for 60 h. Oxidation rates are derived from gravimetric analysis measurements (calculations are described in section 5.1). The alloys W-12Cr-0.5Y HIP, W-10Cr-2Ti HIP and W-15Cr HIP are from previous research in this project[14] [15].

Sample	Thermobalance fit		Analytical balance	
	$K_l/\frac{mg}{cm^2*s}$	$K_p/\frac{mg^2}{cm^4*s}$	$K_l/\frac{mg}{cm^2*s}$	$K_p/\frac{mg^2}{cm^4*s}$
W-10Cr-0.5Y HIP	3.97E-07	1.99E-07	1.31E-06	3.73E-07
W-12Cr-0.5Y HIP	3.09E-06	1.95E-06	-	-
W-10Cr-2Ti HIP + TT	4.72E-06	7.67E-06	-	-
W-15Cr HIP	2.91E-05	2.06E-04	-	-

higher magnification. Thin Cr_2O_3 particles, partly covered with W-Y mixed oxide particles, are observed at the surface. The cross-section in figure 50(c) shows a thin Cr_2O_3 layer just below the surface, followed by a thicker WO_3 layer.

Because of the oxidation inhibition on the surface of W-10Cr-0.5Y HIP alloy, the oxidation was performed at a higher temperature of 1000 °C.

Isothermal Oxidations at 1000 °C

Isothermal oxidation tests were performed at 1000 °C for 24 h and 60 h. The results are shown in figure 51.

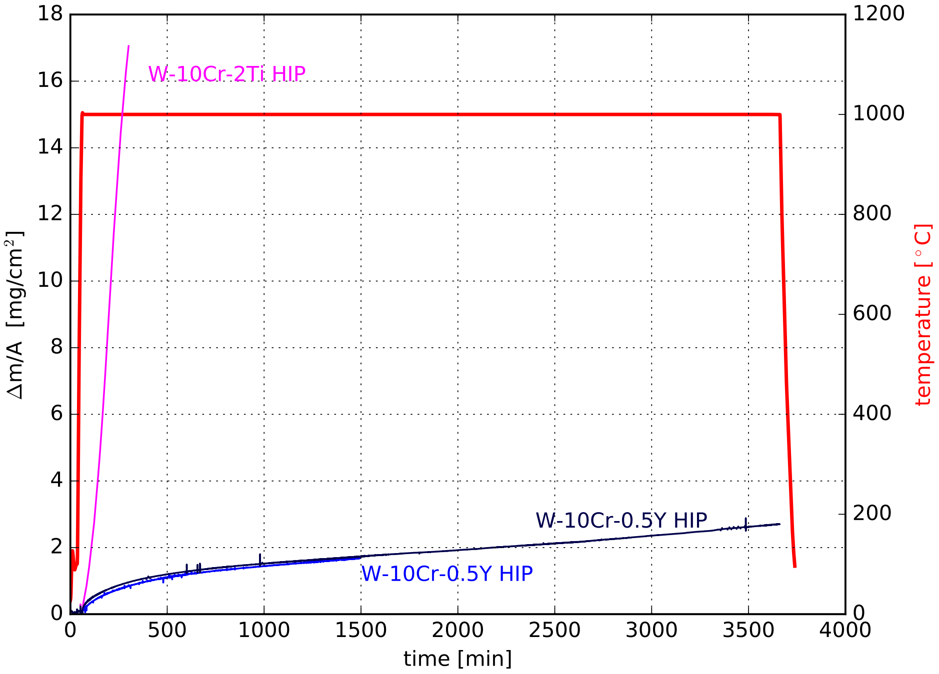

Figure 51: Oxidation at 1000 °C up to 60 h. Data of two different self-passivating tungsten alloys are shown. A 20 % oxygen/80 % argon atmosphere was applied during the oxidation in the thermobalance.

The oxidation rate of W-10Cr-0.5Y HIP is very low and shown in table 14. In the previous research in this project, the self-passivating tungsten alloys did not have a good resistance at a temperature of 1000 °C. The W-10Cr-2Ti HIP alloy was tested and shown in figure 51. The oxidation rate is approximately three orders of magnitude higher than for the new W-10Cr-0.5Y HIP alloy.

The results of the isothermal oxidation experiment at 1000 °C confirm the results of the isothermal oxidation experiment at 800 °C. The W-10Cr-0.5Y HIP alloy shows a good passivation during the oxidation at 1000 °C.

Table 14: Isothermal oxidation at 1000 °C for 60 h. Oxidation rates are derived from gravimetric analysis measurements (calculations are described in section 5.1). Freimut Koch from IPP tested the W-10Cr-2Ti alloy at 1000 °C for 4 h.

Sample	Thermobalance fit		Analytical balance	
	$K_l/\frac{mg}{cm^2*s}$	$K_p/\frac{mg^2}{cm^4*s}$	$K_l/\frac{mg}{cm^2*s}$	$K_p/\frac{mg^2}{cm^4*s}$
W-10Cr-0.5Y HIP	7.56E-06	2.91E-05	1.41E-05	4.28E-05
W-10Cr-2Ti HIP	1.20E-03	2.18E-02	-	-

Accident-Like Oxidation

The accident-like oxidation test is an experiment to simulate a temperature increase in a fusion power plant in case of a total break down of the cooling system. This test gives information at which temperature the self-passivating tungsten alloys lose their protective properties.

The temperature increases from 600 °C to 1000 °C under a 20 % oxygen/80 % argon atmosphere. After one hour, at the maximum temperature of 1000 °C, the chamber was flushed with argon and the argon atmosphere was hold in the TGA system for one hour to see if the oxide evaporates. Next, the oxygen content was set to 20 % to start the oxidation again.

After the next hour the chamber was flushed again with argon and the argon atmosphere was hold in the TGA system. Figure 52 shows the gas flow in the chamber of the TGA system during the experiment.

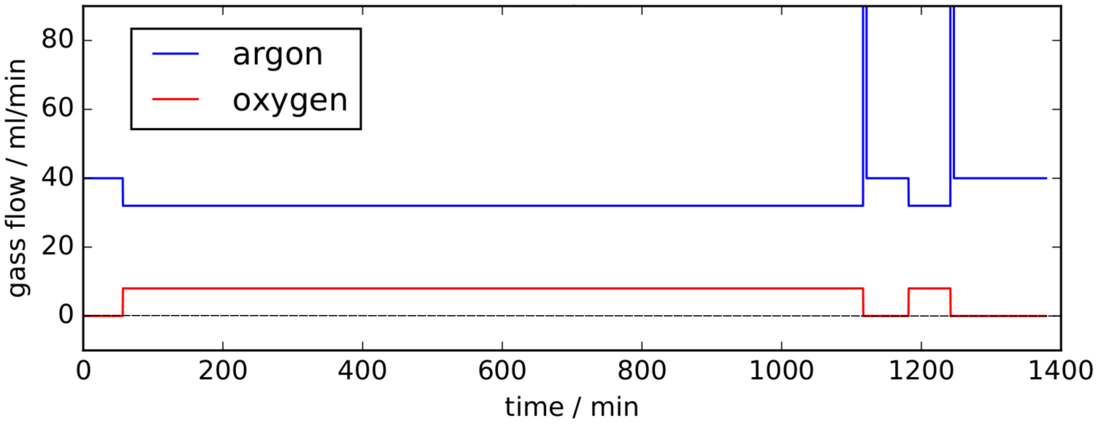

Figure 52: Gas flow in the chamber of the TGA system during the accident-like experiment is shown.

For example in figure 53 is shown that the W-10Cr-2Ti HIP + TT has a strong mass increase at a temperature around 900 °C. Due to the passivating properties,

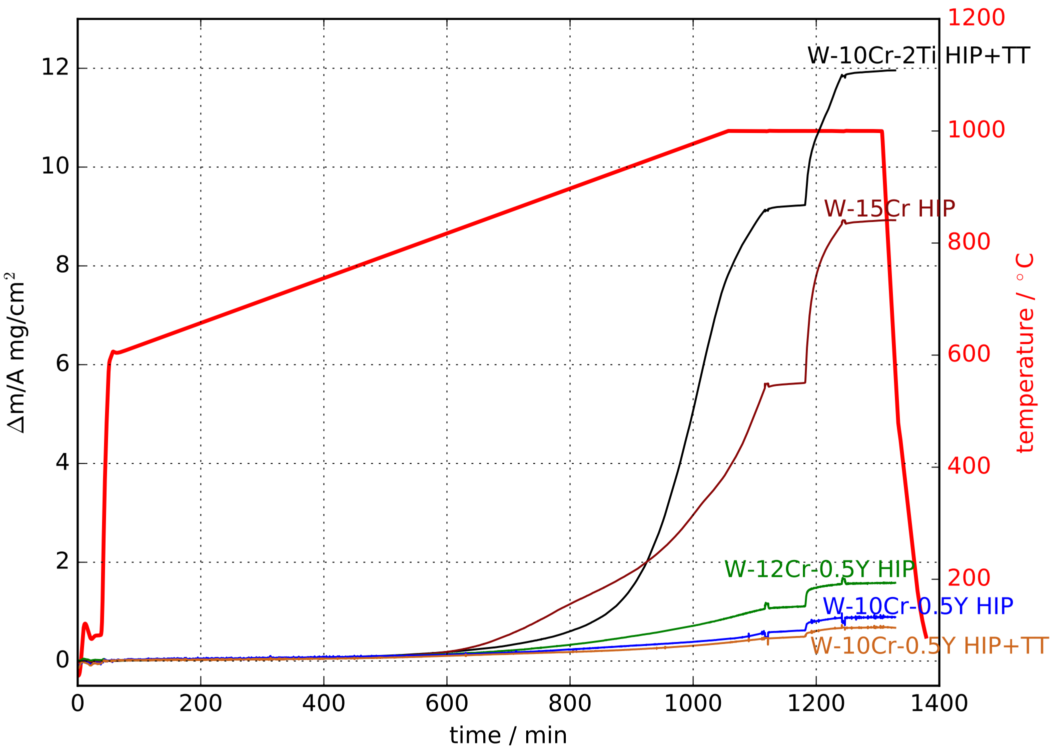

Figure 53: Oxidation experiment simulating accident-like conditions. W-10Cr-0.5Y alloy HIP and W-10Cr-0.5Y alloy HIP+TT were compared to previous research of this project [14] [15]. At the end of the oxidation an argon flash was applied twice to see if there is any evaporation of tungsten oxide.

the W-10Cr-2Ti HIP + TT alloy has a low oxidation rate at lower temperature, but over 900 °C the alloy loses its passivating properties.

The W-10Cr-0.5Y HIP and W-10Cr-0.5Y HIP + TT samples exhibit the lowest oxidation during the accident-like experiment. This behavior is shown in figure 54 with an adapted scale for the mass gain per area.

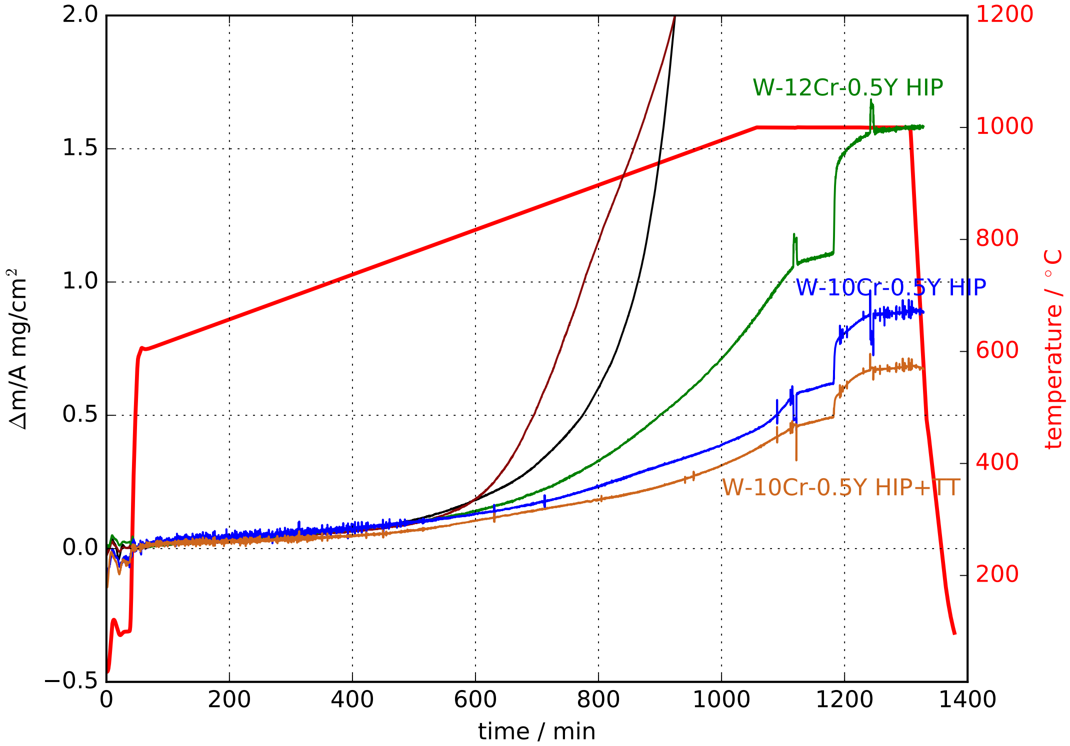

Figure 54: Oxidation experiment simulating accident-like conditions. W-10Cr-0.5Y alloy HIP and W-10Cr-0.5Y alloy HIP+TT were compared to previous research of this project [14] [15]. At the end of the oxidation an agron flash was applied twice to see if there is any evaporation of tungsten oxide.

The W-10Cr-0.5Y HIP + TT alloy shows a better passivating behavior than the same alloy without the temperatur treatment (TT). After flushing the chamber with argon, no evaporation was observed.

In addition to gravimetric analyses, many cross-sections were performed by a SEM and are shown in figure 55. The thickness of the oxide layer and the thickness of the "volcanoes" were measured. More than 13 measurements were performed for both on the W-10Cr-0.5Y HIP and W-10Cr-0.5Y HIP + TT sample and the mean values are given in table 15.

Table 15: The mean value of more than 13 thickness measurements of the oxide layer and of the ”volcanoes” are shown.

Sample	Thickness oxide layer/µm	Thickness ”volcanoes”/µm
W-10Cr-0.5Y HIP + TT	3.3 ± 0.7	10 ± 2
W-10Cr-0.5Y HIP	3.6 ± 0.5	23 ± 10

The thickness measurements confirmed the results of the gravimetric analyses, that the W-10Cr-0.5Y HIP + TT had a lower oxidation than without a TT.

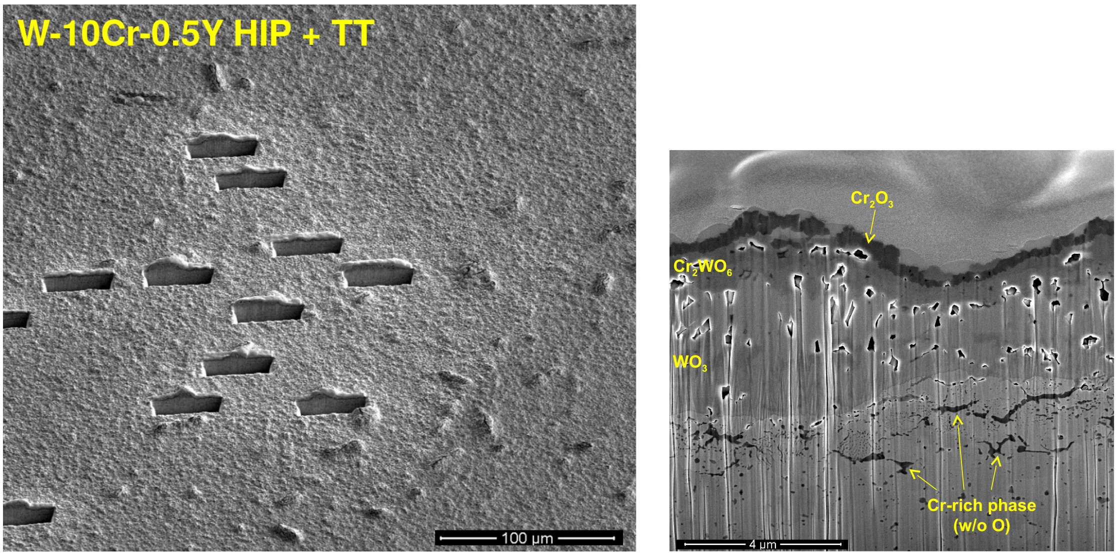

(a) A SEM-image of the surface of the W-10Cr-0.5Y HIP + TT alloy. Many cross-sections were performed.

(b) A SEM-image of an oxide layer of the W-10Cr-0.5Y HIP + TT alloy. Different oxides are observed by EDX.

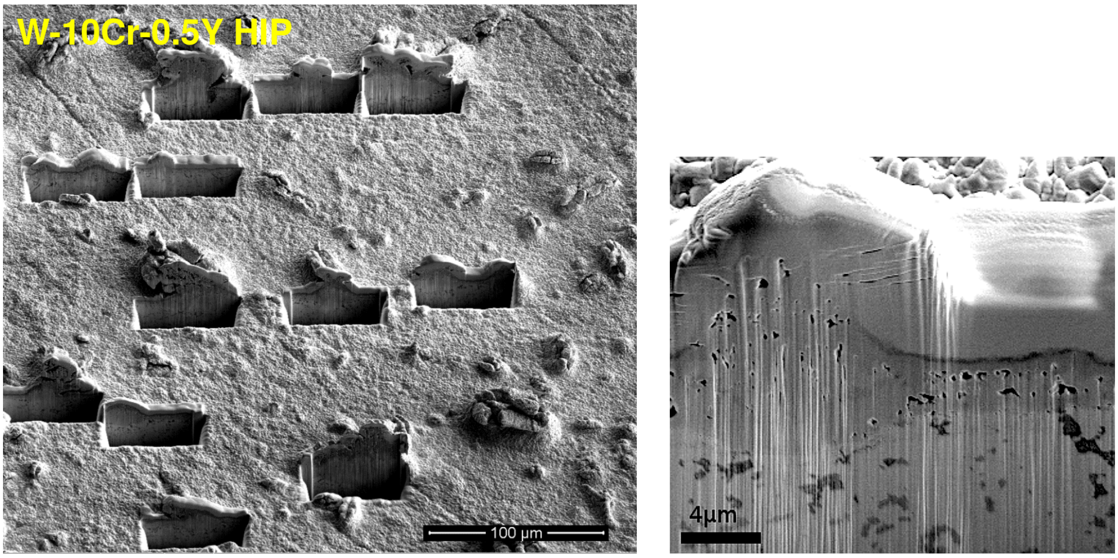

(c) A SEM-image of the surface of the W-10Cr-0.5Y HIP alloy. Many cross-sections were performed.

(d) A SEM-image of an oxide layer of the W-10Cr-0.5Y HIP alloy.

Figure 55: Comparison of the W-10Cr-0.5Y HIP + TT alloy with the W-10Cr-0.5Y HIP alloy.

A.3 Single Crystal

The plan was to compare the data in section 5.2 with oxidation rates obtained from single crystals. Unfortunately, Goodfellows delivered single crystals with an insufficient surface quality.

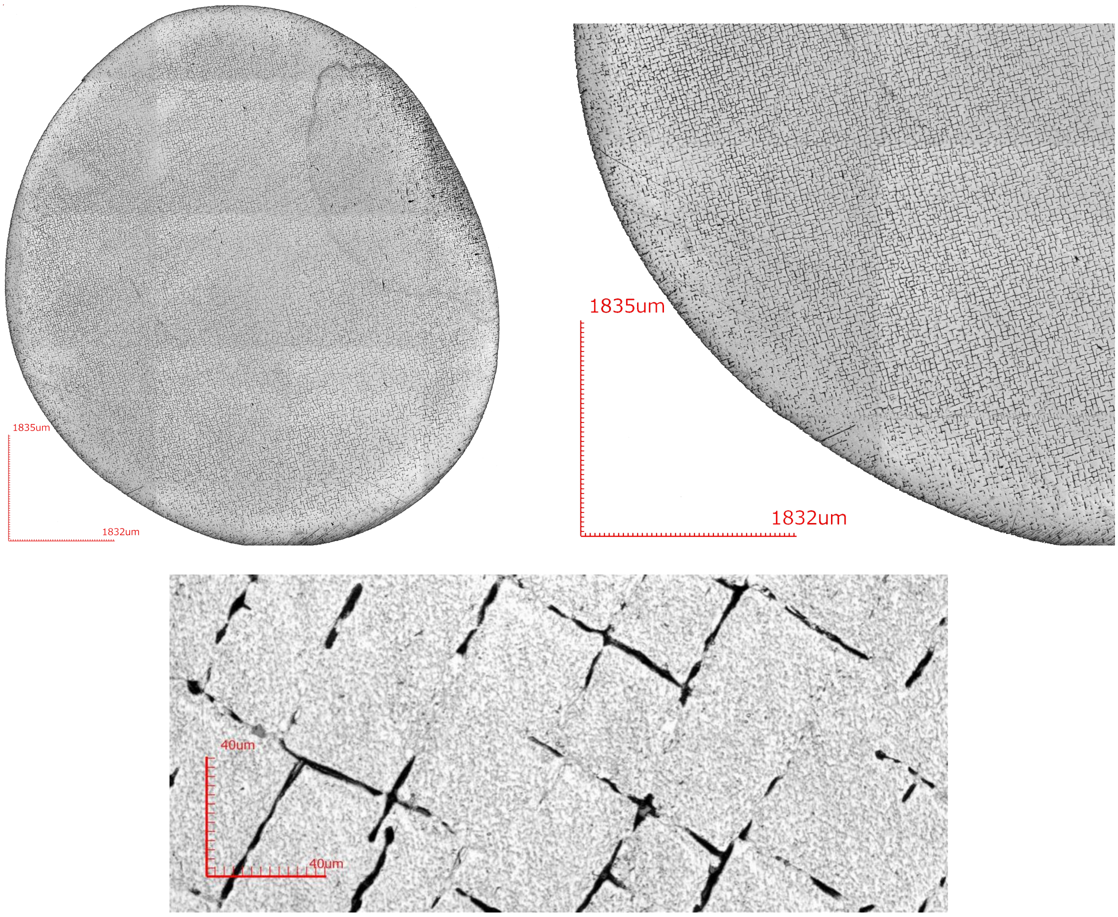

Figure 56: Intensity images of a CLSM at three different magnifications. The samples of Goodfellows were not suitable for oxidation tests because of the cracks on the surface.

An image of a polished single tungsten crystal from Goodfellow with cracks on the surface is shown in figure 56. As the oxidation depends strongly on the surface quality, the single crystals are not suitable for oxidation experiments. Cracks with a width of around 4 µm are present on the surface. This is shown in figure 56. In addition, it was not possible to obtain EBSD-patterns which means that at least the first 10 nm are not crystalline or strongly distorted, i.e. the single crystal polishing is insufficient. Goodfellows accepted the complaint but the reclamation took several months and a second delivery did not solve the problems. It was impossible to do a comparison of tungsten single crystals with polycrystalline tungsten samples in time.

A.4 Additional Graphs and Tables of the Thesis

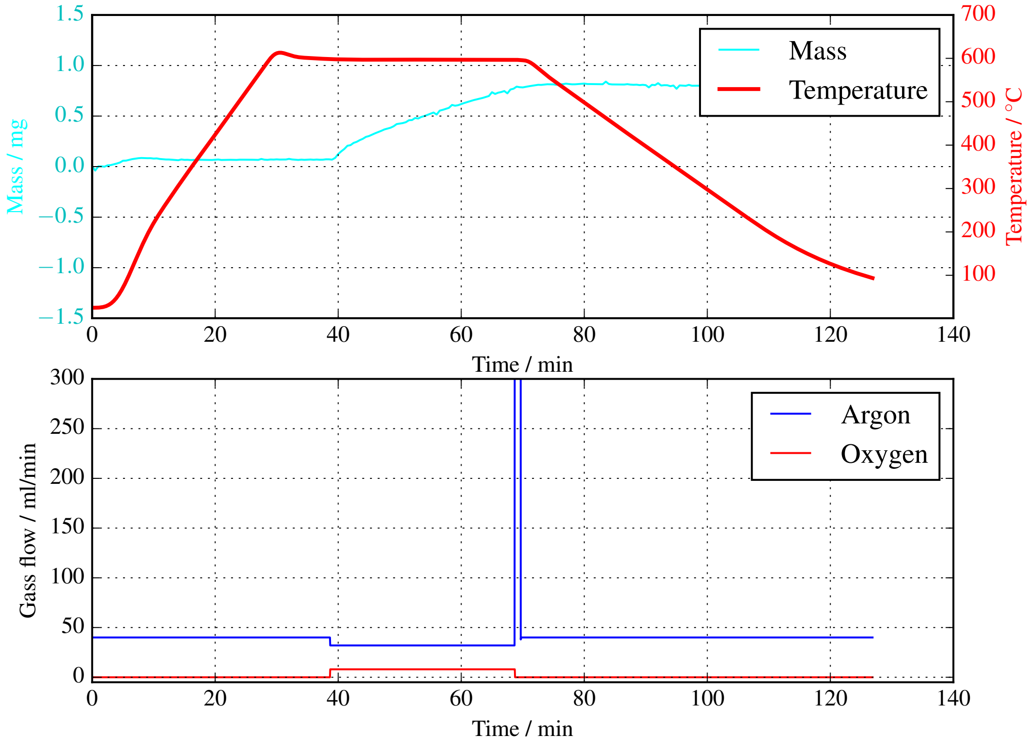

Figure 57: Gas flow experiment using the TGA. The time is shown on the x-axis and the temperature on the left and the mass on the right hand side on the y-axis. The figure below shows the gas flow during the incubation.
This is a single incubation with a gas flow of 40 ccm/min. The mass difference between the 160 ccm/min and the 40 ccm/min incubation is shown in figure 28.

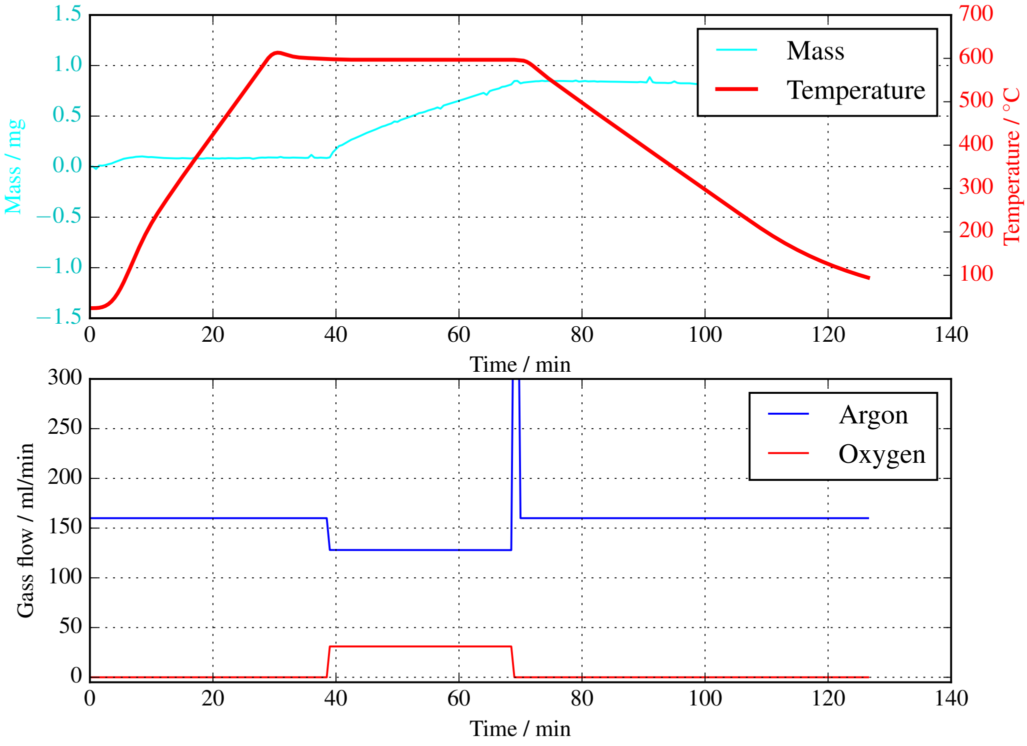

Figure 58: Gas flow experiment using the TGA. The time is shown on the x-axis and the temperature on the left and the mass on the right hand side on the y-axis. The figure below shows the gas flow during the incubation.
This is a single incubation with a gas flow of 160 ccm/min. The mass difference between the 160 ccm/min and the 40 ccm/min incubation is shown in figure 28.

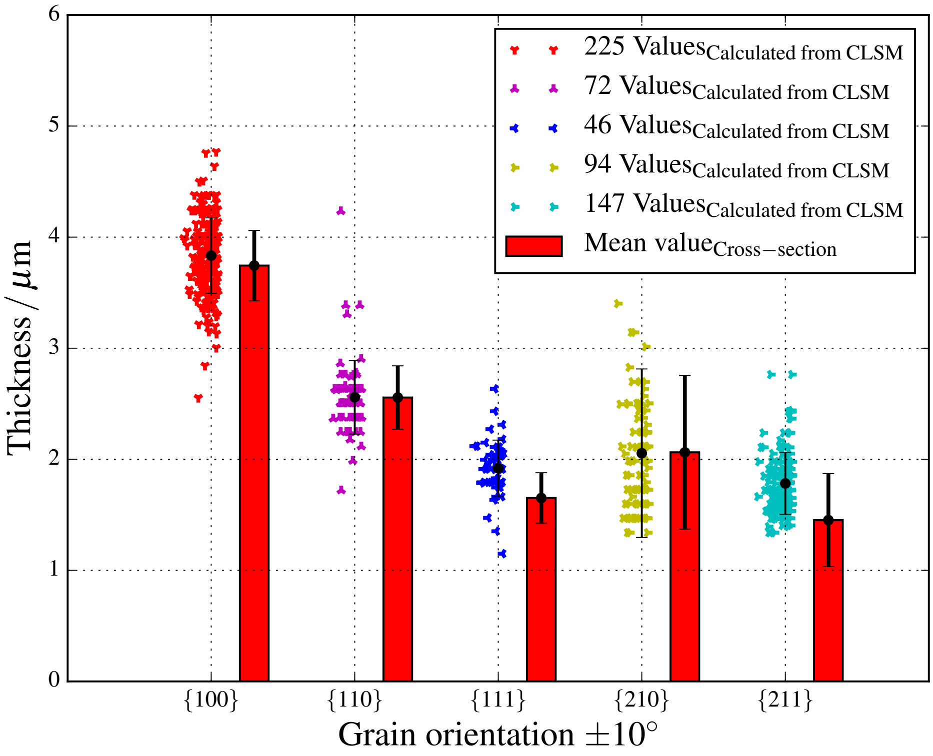

Figure 59: Grain dependent oxidation. The thickness of the oxide layer is plotted against the grain orientation. The values vary randomly on the x-axis to enhance the visibility. The calculated values from the CLSM measurements are shown as points. The growth into the depth is calculated with the number density factor of 0.29 which is described in chapter 5.1.3. The absolute values on cross-sections are shown as bars to compare them with the calculated values from the CLSM. This figure includes five independent incubations.

Table 16: Oxidation rates from gravimetric analysis measurements. The oxidation was performed at 870 K for 30 min.

Sample	Thermo balance Fit		Thermo balance Δm		Analytical balance	
	$\mathrm{K}_l/\frac{mg}{cm^2*s}$	$\mathrm{K}_p/\frac{mg^2}{cm^4*s}$	$\mathrm{K}_l/\frac{mg}{cm^2*s}$	$\mathrm{K}_p/\frac{mg^2}{cm^4*s}$	$\mathrm{K}_l/\frac{mg}{cm^2*s}$	$\mathrm{K}_p/\frac{mg^2}{cm^4*s}$
A1187	2.56E-04	1.71E-04	3.27E-04	1.93E-04	3.48E-04	2.18E-04
A1181	2.81E-04	2.22E-04	3.61E-04	2.34E-04	3.97E-04	2.83E-04
A1183	2.82E-04	2.24E-04	3.62E-04	2.35E-04	3.88E-04	2.72E-04
A1192	2.93E-04	2.18E-04	3.60E-04	2.34E-04	3.92E-04	2.77E-04
A1194	2.16E-04	2.73E-04	2.76E-04	1.37E-04	3.28E-04	1.93E-04
A1198	2.23E-04	4.26E-04	2.70E-04	1.32E-04	3.56E-04	2.28E-04
Mean value	2.58E-04	2.56E-04	3.26E-04	1.94E-04	3.68E-04	2.45E-04
Error	3.28E-05	8.95E-05	4.30E-05	4.91E-05	2.83E-05	3.72E-05

B List of Abbreviations

atm	standard atmosphere
bcc	body-centered cubic
BKD	backscatter Kikuchi diffraction
FEPA	Federation of European Producers of Abrasives
CEIT	Ceit-IK4 Technology Center
CLSM	confocal laser scanning microscope
Cr	chromium
DC	direct current
D-T	deuterium tritium
EBSD	electron backscatter diffraction
EDX	energy dispersive X-ray spectroscopy
Fe	iron
FEI	Field Electron and Ion Co.
FIB	focused ion beam
ϵ_{Flade}	flade-potential
GIS	gas injection system
H	hydrogen
He	helium
HIP	hot isostatic pressing
IPP	Max Planck Institut for Plasma Physics
IPF	inverse pole figure
ISO	International Organization for Standardization
ITER	International Thermonuclear Experimental Reactor

LSM	laser scanning microscope
LBS	pound-force
NaOH	sodium hydroxide
$\mathbf{NaNO_3}$	sodium nitrate
m	mass
MV	mean value
min	minutes
O	oxygen
P	partial pressure
Pt-C	platinum-carbon
PPCS	European Power Plant Conceptual Study
PFC	plasma facing components
RBS	Rutherford Backscattering Spectrometry
RPM	revolutions per minute
s	second
SD	standard deviation
SEM	scanning electron microscope
STA	simultaneous thermal analysis
t	time
TEM	transmission electron microscopy
TGA	thermogravimetric analysis
$\mathbf{T}_R$	recrystallization temperature
TT	temperatur treatment
W	tungsten

WD	working distance
WO_3	tungsten(VI)-oxide
Y	yttrium

References

[1] Anthony J Mcmichael, Diarmid Campbell-Lendrum, Sari Kovats, Sally Edwards, Paul Wilkinson, Theresa Wilson, Robert Nicholls, Simon Hales, Frank Tanser, David Le Sueur, Michael Schlesinger, and Natasha Andronova. Chapter 20 global climate change.

[2] D Maisonnier, D Campbell, I Cook, L Di Pace, L Giancarli, J Hayward, A Li Puma, M Medrano, P Norajitra, M Roccella, P Sardain, MQ Tran, and D Ward. Power plant conceptual studies in europe. *Nuclear Fusion*, 47(11): 1524, 2007. URL `http://stacks.iop.org/0029-5515/47/i=11/a=014`.

[3] Alvin M Weinberg and R Philip Hammond. Limits to the use of energy: The limit to population set by energy is extremely large, provided that the breeder reactor is developed or that controlled fusion becomes feasible. *American Scientist*, 58(4):412–418, 1970. URL `http://www.jstor.org/stable/27829166`.

[4] D Fasel and MQ Tran. Availability of lithium in the context of future d–t fusion reactors. *Fusion Engineering and Design*, 75–79:1163 – 1168, 2005. doi: http://dx.doi.org/10.1016/j.fusengdes.2005.06.345. URL `http://www.sciencedirect.com/science/article/pii/S0920379605003522`. Proceedings of the 23rd Symposium of Fusion TechnologySOFT 23.

[5] JET Team. Fusion energy production from a deuterium-tritium plasma in the jet tokamak. *Nuclear Fusion*, 32(2):187, 1992. URL `http://stacks.iop.org/0029-5515/32/i=2/a=I01`.

[6] Farrokh Najmabadi, A Abdou, L Bromberg, T Brown, VC Chan, MC Chu, F Dahlgren, L El-Guebaly, P Heitzenroeder, D Henderson, HE St John, CE Kessel, LL Lao, GR Longhurst, S Malang, TK Mau, BJ Merrill, RL Miller, E Mogahed, RL Moore, T Petrie, DA Petti, P Politzer, AR Raffray, D Steiner, I Sviatoslavsky, P Synder, GM Syaebler, AD Turnbull, MS Tillack, LM Waganer, X Wang, P West, and P Wilson. The aries-at advanced tokamak, advanced technology fusion power plant. *Fusion Engineering and Design*, 80(1–4):3 – 23, 2006. doi: http://dx.doi.org/10.1016/j.fusengdes.2005.11.003. URL `http://www.sciencedirect.com/science/article/pii/S0920379605007210`.

[7] H Bolt, V Barabash, W Krauss, J Linke, R Neu, S Suzuki, N Yoshida, and ASDEX Upgrade Team. Materials for the plasma-facing components of fusion reactors. *Journal of Nuclear Materials*, 329–333, Part A:66 – 73, 2004. doi: http://dx.doi.org/10.1016/j.jnucmat.2004.04.005. URL `http://`

`www.sciencedirect.com/science/article/pii/S0022311504001242`. Proceedings of the 11th International Conference on Fusion Reactor Materials (ICFRM-11).

[8] M Rieth, JL Boutard, SL Dudarev, T Ahlgren, S Antusch, N Baluc, M-F Barthe, CS Becquart, L Ciupinski, JB Correia, C Domain, J Fikar, E Fortuna, C-C Fu, E Gaganidze, TL Galán, C García-Rosales, B Gludovatz, H Greuner, K Heinola, N Holstein, N Juslin, F Koch, W Krauss, KJ Kurzydlowski, J Linke, Ch Linsmeier, N Luzginova, H Maier, MS Martínez, JM Missiaen, M Muhammed, A Muñoz, M Muzyk, K Nordlund, D Nguyen-Manh, P Norajitra, J Opschoor, G Pintsuk, R Pippan, G Ritz, L Romaner, D Rupp, R Schäublin, J Schlosser, I Uytdenhouwen, JG van der Laan, L Veleva, L Ventelon, S Wahlberg, F Willaime, S Wurster, and MA Yar. Review on the efda programme on tungsten materials technology and science. *Journal of Nuclear Materials*, 417(1–3):463 – 467, 2011. doi: http://dx.doi.org/10.1016/j.jnucmat.2011.01.075. URL `http://www.sciencedirect.com/science/article/pii/S0022311511001073`. Proceedings of ICFRM-14.

[9] V Barabash, G Federici, R Matera, A R Raffray, and ITER Home Teams. Armour materials for the iter plasma facing components. *Physica Scripta*, 1999 (T81):74, 1999. URL `http://stacks.iop.org/1402-4896/1999/i=T81/a=014`.

[10] RA Causey, JN Brooks, and G Federici. Tritium inventory and recovery in next-step fusion devices. *Fusion Engineering and Design*, 61–62:525 – 536, 2002. doi: http://dx.doi.org/10.1016/S0920-3796(02)00248-X. URL `http://www.sciencedirect.com/science/article/pii/S092037960200248X`.

[11] I Cook, D Maisonnier, N P Taylor, DJ Ward, P Sardain, L Di Pace, L Giancarli, S Hermsmeyer, P Norajitra, and R Forrest. European fusion power plant studies. 2004.

[12] E Lassner and W D Schubert. *Tungsten: Properties, Chemistry, Technology of the Elements, Alloys, and Chemical Compounds*. Springer US, 1999. ISBN 9780306450532.

[13] YA Yang, Y Ma, JN Yao, and BH Loo. Simulation of the sublimation process in the preparation of photochromic wo_3 film by laser microprobe mass spectrometry. *Journal of Non-Crystalline Solids*, 272(1):71 – 74, 2000. doi: http://dx.doi.org/10.1016/S0022-3093(00)00226-X. URL `http://www.sciencedirect.com/science/article/pii/S002230930000226X`.

[14] A Calvo, N Ordás, I Iturriza, JY Pastor, E Tejado, F Koch, H Greuner, G Pintsuk, A Litnovsky, C Sarbu, et al. Manufacturing and testing of self-passivating tungsten alloys of different composition. In *17th International Conference on Fusion Reactor Materials (ICFRM-17)*, 2015.

[15] C García-Rosales, P López-Ruiz, S Alvarez-Martín, A Calvo, N Ordás, F Koch, and J Brinkmann. Oxidation behaviour of bulk w-cr-ti alloys prepared by mechanical alloying and hiping. *Fusion Engineering and Design*, 89(7–8):1611 – 1616, 2014. doi: http://dx.doi.org/10.1016/j.fusengdes.2014.04.057. URL `http://www.sciencedirect.com/science/article/pii/S0920379614003342`. Proceedings of the 11th International Symposium on Fusion Nuclear Technology-11 (ISFNT-11) Barcelona, Spain, 15-20 September, 2013.

[16] F Jenko. Plasmaphysik ii.

[17] N P Taylor and R Pampin. Activation properties of tungsten as a first wall protection in fusion power plants. 2005.

[18] W Borchardt-Ott and H Sowa. *Kristallographie: Eine Einführung für Naturwissenschaftler*. Springer-Lehrbuch. Springer Berlin Heidelberg, 2013. ISBN 9783642348112.

[19] W Weil and W Schubert. 03.12.2015. URL `http://www.itia.info/assets/files/newsletters/Newsletter_2013_06.pdf`.

[20] Crystalpic, 10.11.2015. URL `https://en.wikipedia.org/wiki/File:Crystalline_polycrystalline_amorphous2.svg`.

[21] W Weißbach. *Werkstoffkunde: Strukturen, Eigenschaften, Prüfung*. Viewegs Fachbücher der Technik. Vieweg + Teubner, 16 edition, 2007. ISBN 9783834807397.

[22] W König. *Fertigungsverfahren 3: Abtragen, Generieren und Lasermaterialbearbeitung*. VDI-Buch. Springer Berlin Heidelberg, 2007. ISBN 9783540489542.

[23] Electropolishing, 13.11.2015. URL `https://en.wikipedia.org/wiki/Electropolishing`.

[24] P F Schmidt. *Praxis der Rasterelektronenmikroskopie und Mikrobereichsanalyse*. Kontakt & Studium: Messtechnik. Expert-Verlag GmbH, Fachverlag für Wirtschaft und Technik, 1994. ISBN 3-8169-1038-6.

[25] 20.08.2016. URL `http://www.epp-online.de/image/image_gallery?img_id=40041575`.

[26] S L Flegler, J W Heckman, and K L Klomparens. *Elektronenmikroskopie: Grundlagen, Methoden, Anwendungen.* Spektrum, Akad. Verlag, 1995. ISBN 3-86025-341-7.

[27] Kikuchi kegel (ebsd), 22.02.2016. URL `http://ssd.phys.strath.ac.uk/index.php/Electron_backscatter_diffraction_%28EBSD%29`.

[28] HP Meyers and HP Myers. *Introductory solid state physics.* CRC press, 1997.

[29] V Randle. *Microtexture Determination and Its Applications.* Book (Institute of Materials (Great Britain))). Maney for the Institute of Materials, Minerals and Mining, 2003. ISBN 9781902653839. URL `https://books.google.de/books?id=14OeAQAAIAAJ`.

[30] B D Ratner, A S Hoffman, F J Schoen, and J E Lemons. *Biomaterials Science: An Introduction to Materials in Medicine.* Elsevier Science, 2004. ISBN 9780080470368. URL `https://books.google.de/books?id=9PMU1iYGe34C`.

[31] Clsm picture, 21.06.2016. URL `http://www.olympus-ims.com/de/metrology/ols4000/`.

[32] 20.06.2016. URL `https://www.netzsch-thermal-analysis.com/de/produkte-loesungen/simultane-thermogravimetrie-dynamische-/differenzkalorimetrie/sta-449-f3-jupiter/`.

[33] J Habainy and C Nilsson. Oxidation of pure tungsten in the temperature interval 400 to 900 ° c. 09.2013.

[34] A Manhard, M Balden, and S Elgeti. Quantitative microstructure and defect density analysis of polycrystalline tungsten reference samples after different heat treatments. *Practical Metallography - Praktische Metallographie*, 52:437–466, 2015.

[35] F Koch, J Brinkmann, S Lindig, T P Mishra, and Ch Linsmeier. Oxidation behaviour of silicon-free tungsten alloys for use as the first wall material. *Physica Scripta*, 2011(T145):014019, 2011. URL `http://stacks.iop.org/1402-4896/2011/i=T145/a=014019`.

[36] SC Cifuentes, MA Monge, and P Pérez. On the oxidation mechanism of pure tungsten in the temperature range 600–800 °c. *Corrosion Science*, 57:114 – 121, 2012. doi: http://dx.doi.org/10.1016/j.corsci.2011.12.027. URL `http://www.sciencedirect.com/science/article/pii/S0010938X11006664`.

[37] EA Gulbransen and KF Andrew. Kinetics of the oxidation of pure tungsten from 500 to 1300 c. *Journal of The Electrochemical Society*, 107(7):619–628, 1960.

[38] T Engel and R Gomer. Adsorption of inert gases on tungsten: Measurements on single crystal planes. 52:5572–5580, 1970. doi: 10.1063/1.1672827.

[39] Crystal lattice figures, 16.08.2016. URL `http://www.phchem.uni-duisburg-essen.de/photochem/Crystal%20faces.pdf`.

[40] Joseph R Ligenza. Effect of crystal orientation on oxidation rates of silicon in high pressure steam. *The Journal of Physical Chemistry 65.11 (1961): 2011-2014*.

List of Figures

List of Tables

Affirmation

Hereby I declare that I have been working independently and used no other than the specified sources, references and resources. This work has not been published or submitted to further examination authority in the same or similar form until now.

Ulm, den ....

Karsten Schlüter